Concurrent Multi-Band Envelope Tracking Power Amplifiers for Emerging Wireless Communications

by

Hassan Sarbishaei

A thesis
presented to the University of Waterloo
in fulfillment of the
thesis requirement for the degree of
Doctor of Philosophy
in
Electrical and Computer Engineering

Waterloo, Ontario, Canada, 2014

Author's Declaration

I hereby declare that I am the sole author of this thesis. This is a true copy of the thesis, including any required final revisions, as accepted by my examiners.

I understand that my thesis may be made electronically available to the public.

Hassan Sarbishaei

Abstract

Emerging wireless communication is shifting toward data-centric broadband services, resulting in employment of sophisticated and spectrum efficient modulation and access techniques. This yields communication signals with large peak-to-average power ratios (PAPR) and stringent linearity requirements. For example, future wireless communication standard, such as long term evolution advanced (LTE-A) require adoption of carrier aggregation techniques to improve their effective modulation bandwidth. The carrier aggregation technique for LTE-A incorporates multiple carriers over a wide frequency range to create a wider bandwidth of up to $100\,MHz$. This will require future power amplifiers (PAs) and transmitters to efficiently amplify concurrent multi-band signals with large PAPR, while maintaining good linearity.

Different back-off efficiency enhancement techniques are available, such as envelope tracking (ET) and Doherty. ET has gained a lot of attention recently as it can be applied to both base station and mobile transmitters. Unfortunately, few publications have investigated concurrent multi-band amplification using ET PAs, mainly due to the limited bandwidth of the envelope amplifier. In this thesis, a novel approach to enable concurrent amplification of multi-band signals using a single ET PA will be presented.

This thesis begins by studying the sources of nonlinearities in single-band and dual-band PAs. Based on the analysis, a design methodology is proposed to reduce the sources of memory effects in single-band and dual-band PAs from the circuit design stage and improve their linearizability. Using the proposed design methodology, a $45\,W$ GaN PA was designed. The PA was linearized using easy to implement, memoryless digital pre-distortion (DPD) with 8 and 28 coefficients when driven with single-band and dual-band signals, respectively. This analysis and design methodology will enable the design of PAs with reduced memory effects, which can be linearized using simple, power efficient linearization techniques, such as lookup table or memoryless polynomial DPD. Note that the power dissipation of the linearization engine becomes crucial as we move toward smaller base station cells, such as femto- and pico-cells, where complicated DPD models cannot be implemented due to their significant power overhead. This analysis is also very important when implementing a multi-band ET PA system, where the sources of memory effects in the PA itself are minimized through the proposed design methodology.

Next, the principle of concurrent dual-band ET operation using the low frequency component (LFC) of the envelope of the dual-band signal is presented. The proposed dual-band ET PA modulates the drain voltage of the PA using the LFC of the envelope of the dual-band signal. This will enable concurrent dual-band operation of the ET PA without posing extra bandwidth requirements on the envelope amplifier. A detailed efficiency and linearity analysis of the dual-band ET PA is also presented. Furthermore, a new dual-band DPD model with supply dependency is proposed in this thesis, capable of capturing and compensating for the sources of distortion in the dual-band ET PA. To the best of our knowledge, concurrent dual-band operation of ET PAs using the LFC of the envelope of the dual-band signal is presented for the first time in the literature. The proposed dual-band ET operation is validated using the measurement results of two GaN ET PA prototypes.

Lastly, the principle of concurrent dual-band ET operation is extended to multi-band signals using the LFC of the envelope of the multi-band signal. The proposed multi-band ET operation is validated using the measurement results of a tri-band ET PA. To the best of our knowledge, this is the first reported tri-band ET PA in literature. The tri-band ET PA is linearized using a new tri-band DPD model with supply dependency.

Acknowledgements

I would like to take this opportunity to express my deepest gratitude to my supervisor, Professor Slim Boumaiza, for his never-ending help and support throughout my research. I would also like to thank him for giving me the chance to be involved in different research projects and showing me different aspects of conducting research. Moreover, I would like to thank my committee members for reviewing my thesis and their insightful comments.

I have also had the honor to be part of an amazing research group. Throughout the years, everyone in EmRG research group have become more like a family to me. A special thanks to David Wu and Yushi Hu for all the engaging technical and non-technical discussions that we have had over the years. I will greatly miss our debates on various topics from circuits to religion. I would also like to thank Sarah Wallace for always providing helpful feedback on my writing.

Last but not least, I would like to show my gratitude to my family. Their unconditional love and support over the years has made this journey possible.

Dedication

To my loving family

Table of Contents

List of Tables

List of Figures

List of Abbreviations

2D-CR-GMP	Dual-band complexity reduced generalized memory polynomial
3D-CR-GMP	Tri-band complexity reduced generalized memory polynomial
4G	Fourth generation
5G	Fifth generation
ACLR	Adjacent channel leakage ratio
ACPR	Adjacent channel power ratio
BBE	Baseband equivalent
CDMA	Code division of multiple of access
CMOS	Complementary metal-oxide semiconductor
CORDIC	Coordinate rotation digital computer
DAC	Digital to analog converter
DIDO	Dual-input dual-output
DPA	Doherty power amplifier
DPD	Digital pre-distortion
DSM	Delta-signal modulation
EDGE	Enhanced data rates for GSM evolution
EER	Envelope elimination and restoration

ET	Envelope tracking
EVM	Error vector magnitude
GaAs	Gallium arsenide
GaN	Gallium nitride
GMP	Generalized memory polynomial
GSM	Global system for mobile communications
HBT	Heterojunction bipolar transistors
HEMT	High electron mobility transistor
LDMOS	Laterally diffused metal-oxide semiconductor
LDO	Low dropout
LINC	Linear amplification using nonlinear components
LTE	Long term evolution
LTE-A	Long term evolution advanced
LTI	Linear time invariant
OFDM	Orthogonal frequency division multiplexing
PA	Power amplifier
PAE	Power added efficiency
PAPR	Peak-to-average power ratio
PDF	Power density function
PLL	Phased-locked loop
PSK	Phase shift keying
PWM	Pulse-width modulation
PWPM	Pulse-width/position modulation

QAM	Quadrature amplitude modulation
RF	Radio frequency
RF-DAC	Radio frequency digital to analog converter
SDR	Software-defined radio
SiGe	Silicon germanium
SISO	Single-input single-output
SMPA	Switched mode power amplifier
SOI	Silicon on insulator
UMTS	Universal mobile telecommunication system
VCO	Voltage controlled oscillator
WCDMA	Wideband code division multiple access
WiMAX	Worldwide interoperability for microwave access
WLAN	Wireless local area network

Chapter 1

Introduction

1.1 Motivation

Wireless communication is moving inexorably from voice-centric to data-centric broadband services in order to address ever changing connectivity demands. Future wireless networks will need to meet the more challenging requirements imposed by the co-existence of multiple communication standards, resulting in various technical and economic challenges for both service providers and consumers. For example, new standards, such as fourth generation (4G) long term evolution (LTE), will be required to support legacy standards, such as global system for mobile communications (GSM) and universal mobile telecommunication system (UMTS). Backward compatibility has traditionally been achieved by using multiple transceivers, one for each standard, which is both area and power inefficient. Software-defined radio (SDR) is an alternative solution which addresses the co-existence of multiple standards with minimal additional hardware. To some extent, SDR is made possible by highly reconfigurable, multi-band and multi-standard radio frequency (RF) transceivers which can be reprogrammed for varying power, frequency and standard requirements. Furthermore, future wireless communication standards, such as long term evolution advanced (LTE-A), will also require adoption of frequency aggregation techniques to increase the bandwidth and data rate of the communication link. Carrier aggregation technique incorporates multiple carriers over a wide frequency spectrum to deploy a wider bandwidth of up to $100\,MHz$. Three scenarios for carrier aggregation are foreseen; (i) intra-band contiguous carrier aggregation, (ii) intra-band non-contiguous carrier aggregation, and (iii) inter-band carrier aggregation, as shown in Figure 1.1. In order for transmitters and power amplifiers (PAs) to accommodate these three scenarios, they will need to concurrently transmit multi-band signals under various power and frequency scenarios.

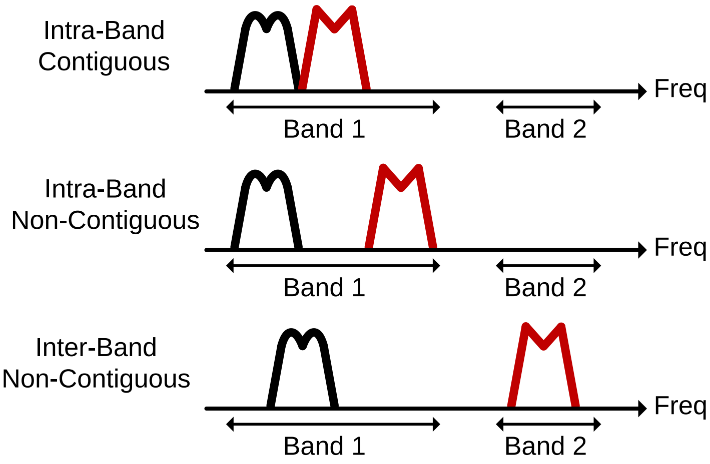

Figure 1.1: Three different modes of carrier aggregation.

Another challenge for multi-standard transmitters is the increasing peak-to-average power ratio (PAPR) and signal quality requirements of modern communication standards. Due to the enormous cost of spectrum allocation and the limited spectrum available, emerging standards, such as LTE, worldwide interoperability for microwave access (WiMAX) and wireless local area network (WLAN), have been designed to maximize spectral efficiency. High spectral efficiency techniques, such as orthogonal frequency division multiplexing (OFDM), typically increase PAPR and linearity requirements for both the transmitter and the PA. Figure 1.2 shows the probability density function (PDF) and the time-domain amplitude of a multi-carrier wideband code division multiple access (WCDMA) signal with a PAPR of $8.0\,dB$. In a typical PA the efficiency drops significantly as the output power is backed-off from its peak value. To illustrate this problem, Figure 1.3 shows the efficiency of an ideal class-B PA versus output power. As it can be seen, the efficiency of the class-B PA drops from 78.5% at peak output power to 30% when amplifying a modulated signal with a PAPR of $8.0\,dB$. The low average efficiency of the PA, and hence transmitter, results in a low battery lifetime for hand-held devices and high operation costs for base stations, in addition to reduced reliability due to significant heat dissipation and greater cooling costs for base stations.

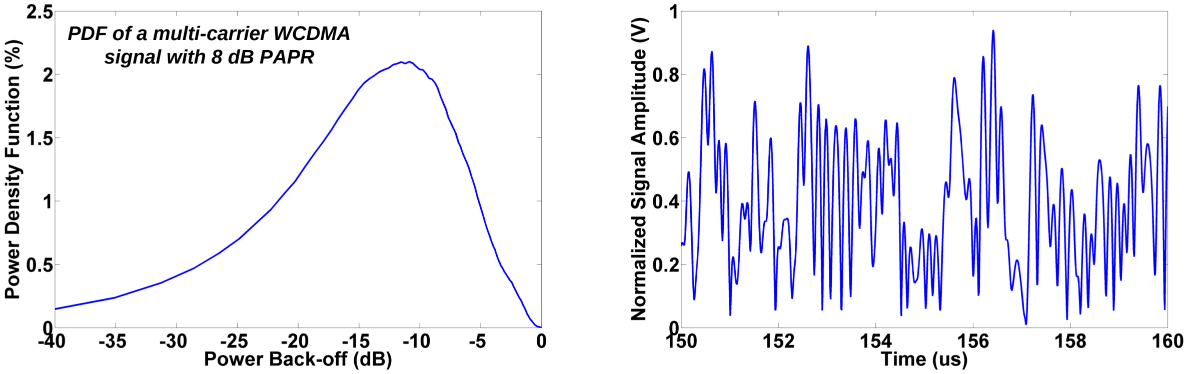

(a) PDF of the multi-carrier WCDMA signal

(b) WCDMA waveform illustrating high PAPR

Figure 1.2: PDF and time-domain waveform of a multi-carrier WCDMA signal with a PAPR of $8\,dB$.

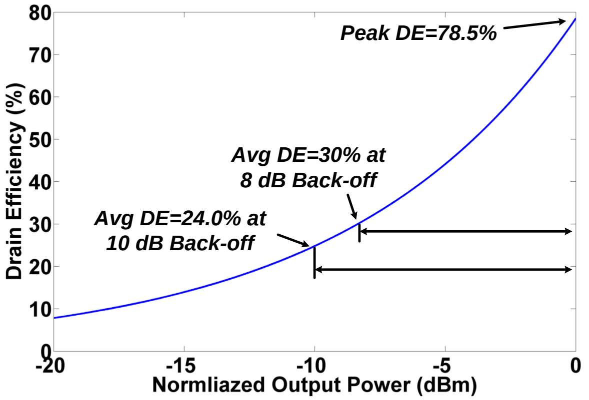

Figure 1.3: Drain efficiency of an ideal class-B power amplifier at power back-off.

1.2 Problem Statement

As stated in Section 1.1, while emerging wireless standards offer significant improvements in terms of network capacity and quality of service, the resulting characteristics of the signals as well as the ever increasing number of standards impose new challenges to the design of RF transmitters, especially PAs. Hence, there is a need for highly efficient transmitters that, when driven with high PAPR signals are capable of supporting concurrent multi-standard operation while meeting the stringent linearity requirements of modern communication signals. To achieve high efficiency at back-off power levels, different techniques have been investigated in the literature, such as Doherty [1], envelope tracking (ET) [2], and envelope elimination and restoration (EER) [3]. Recently, wideband and multi-band implementations of Doherty and ET PAs have been investigated extensively in an attempt to satisfy the demand for multi-standard operation of such PAs in modern base stations. However, few publications have focused on concurrent amplification of multi-standard signals. This limits the application of such wideband or multi-band PAs for frequency aggregated signals, such as LTE-A, where the amplifier is concurrently driven with multiple signals.

This thesis presents a novel approach to enable concurrent amplification of multi-standard signals using a single ET PA. The new amplifier is capable of efficiently amplifying concurrent multi-standard signals without posing excessive bandwidth requirement on the envelope amplifier. In this thesis, the focus is on the design of ET PAs for base station infrastructures, such as pico- and femto-cells. The proposed ET PA is capable of the amplification of inter-band non-contiguous and intra-band non-contiguous scenarios for carrier aggregated signals. In order to meet the demanding linearity requirements of modern base stations, a new baseband digital predistortion (DPD) technique has also been proposed to compensate for the added distortions of the concurrent multi-band ET PA. It is important to note that the proposed technique may also be suitable for mobile PAs. However, further research is required to investigate the compatibility of the proposed technique for mobile transmitters to meet the linearity requirements without power hungry linearization techniques.

1.3 Thesis Outline

This thesis is organized as follows. Chapter 2 presents a survey of existing transmitter and PA efficiency enhancement techniques together with a summary of relevant publications. The efficiency enhancement techniques surveyed include load modulation technique, drain modulation technique and advanced RF transmitter architectures. The suitability of these techniques for multi-standard operation will also be discussed.

Chapter 3 investigates the linearity and memory effects of PAs under single-band and dual-band excitations from a circuit perspective. The analysis begins with a simplified circuit model for a nonlinear transistor then discusses how different sources of nonlinearity contribute to the overall nonlinearity and memory effects in PAs. Based on this analysis, a wideband high efficiency PA is designed that minimizes the sources of memory effects from the circuit design stage. This translates to relaxed requirements for the complexity of the DPD models, and power/area of the DPD engine.

Chapter 4 discusses the basic principle of dual-band ET PA operation using the low frequency component of the envelope of the dual-band signal. A detailed linearity and efficiency analysis of the dual-band ET PA is presented together with simulation and measurement results to validate the concept. Furthermore, a new dual-band DPD model with supply dependency capable of capturing and compensating for the sources of distortion inherent to the dual-band ET PA is proposed.

Chapter 5 extends the proposed dual-band ET operation to multi-band signals using the low frequency component of the envelope of the multi-band signal. With the aid of measurement and simulation results of a tri-band ET PA, the proposed tri-band ET operation is validated. A new tri-band DPD model with supply dependency is also presented to linearize the sources of distortion associated with the tri-band ET PA.

The contribution of this work to the field is discussed in Chapter 6. In addition, possible directions for future research work on this topic are discussed.

Chapter 2

High Efficiency Multi-Standard RF Transmitters and PAs

2.1 Introduction

As mentioned in Chapter 1, the large PAPR of modern communication signals significantly degrades the average efficiency of PAs, and consequently transmitters. Typical class-A, -AB and -B PAs are capable of achieving high efficiency at peak power (e.g., ideal class-B achieves 78.5% peak drain efficiency), however, the efficiency starts to drop quickly as the output power is backed off from its peak value. This is illustrated clearly in Figure 1.3. The efficiency drop at back-off power levels is the result of a smaller drain-source voltage swing. Various techniques have been devised in the literature to improve the efficiency of PAs at back-off power while maintaining overall linearity. This chapter presents a review of existing efficiency enhancement techniques together with a summary of relevant recent publications. These techniques are broadly categorized into three groups: load modulation technique, drain modulation technique and advanced transmitter architectures. The suitability of these techniques for true concurrent multi-standard PAs/transmitters will also be discussed.

2.2 Load Modulation Technique

2.2.1 Basic Principle

A common technique to improve the efficiency of PAs at back-off power is to modulate the load impedance of the transistor. By modulating the load impedance (in most cases increasing the load impedance at power back-off), one ensures the transistor drain source voltage swings to its peak value, hence maintaining high drain efficiency. The Doherty PA (DPA) is the most popular load modulation technique; the impedance seen by the main transistor is modulated, as a function of the input signal power, using an auxiliary transistor [1]. The simplified schematic of a DPA is shown in Figure 2.1. The main transistor is typically biased in class-AB, hence conducting all the time, while the auxiliary transistor is biased in class-C, conducting current in the last $6\,dB$ (i.e., from $6\,dB$ back-off to peak power). While the auxiliary transistor is not conducting, the DPA behaves identically to a class-AB PA. Starting from $6\,dB$ back-off, the auxiliary transistor begins conducting and modulates the load impedance seen by the main transistor through the quarter-wave impedance inverter. As the auxiliary transistor injects more current to the load, the load impedance seen by the main transistor increases; thus maintaining the efficiency of the main transistor and the DPA at power back-off. Detailed analysis of this technique can be found in numerous publications, such as, [4–7].

2.2.2 Load Modulation Technique in Literature

DPAs are widely used in base station transmitters with output power ranging from tens to a few hundreds of watts, achieving back-off efficiency in excess of 40% to 50% [5]. DPAs have also been utilized for low-power mobile transmitters using lumped passive components [8, 9]. However, its application in this type of mobile transmitter has been limited due to the complex passive circuitry, added loss, and required area. Traditional DPA design methods have been band-limited (less than 10% fractional bandwidth) due to theoretical and practical issues, such as offset lines, the quarter-wave transformer and the transistor's parasitics. Several attempts have been reported in the literature to extend the traditional DPA to amplify multi-standard and multi-band signals. This has generally been attempted by extending the bandwidth of the DPA to incorporate multiple communication bands (e.g., [5, 10]), or by developing multi-band DPA architecture capable of operating at two discrete frequencies (e.g., [11, 12]).

Most of the recent work on extending the bandwidth of a DPA relies on one of the two approaches. The first approach employs a mixed-signal setup to allow the separate adjustment of the input amplitude and phase across the bandwidth (also called mixed signal DPA) [7]. Note

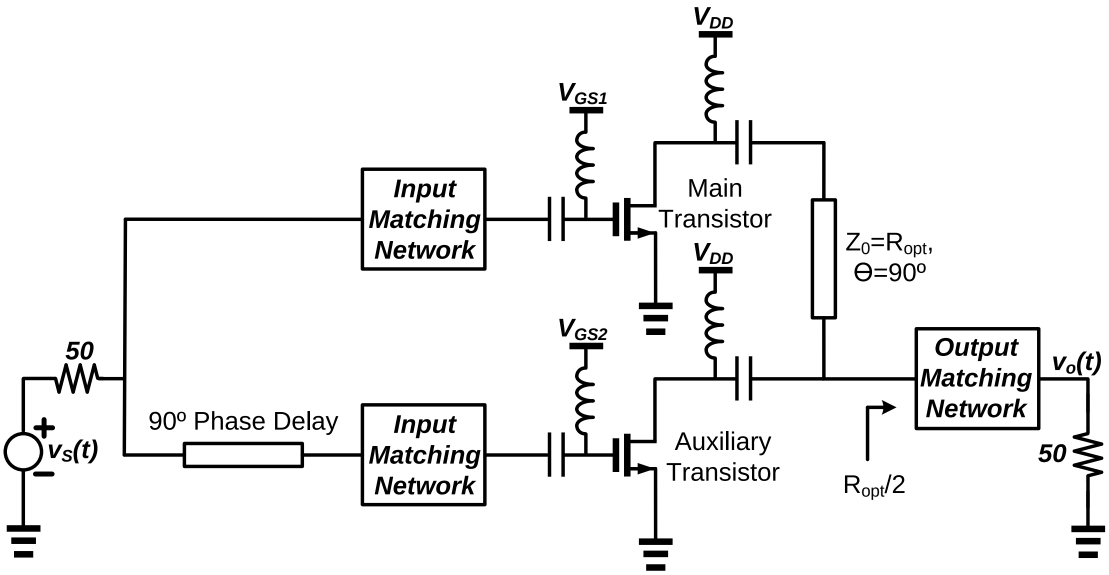

Figure 2.1: Simplified schematic of a DPA.

that a mixed signal DPA, while capable of achieving excellent back-off efficiency and bandwidth [7, 10, 13, 14] (e.g. DPA in [13] maintains more than 58% drain efficiency at $6\,dB$ back-off for 40% fractional bandwidth), requires a more complicated mixed signal setup. Furthermore, mixed signal DPAs are not suitable for concurrent amplification of multi-band signals. The second approach investigates new output combiners to extend the bandwidth of the DPA [5,10,13,15,16]. An example of a wideband DPA with a novel output combiner was presented in [10] where authors replaced the quarter-wave transformer with a lumped-component model, alleviating the bandwidth limitation of the DPA by absorbing the transistor's parasitics. Another novel output combiner was presented in [5, 13, 15] which extended the bandwidth capacity of a traditional two-way DPA for different power back-offs; however, this method requires two different supply voltages for the main and peaking transistors resulting in high breakdown voltage requirements for the peaking transistor.

It is important to note that most of the DPA publications do not target concurrent amplification of multi-standard signals. Only a few recent publications have shown measurement results for a DPA driven with concurrent dual-band signals [11,12,16]. Further research into the compatibility of DPAs for concurrent dual- and multi-standard operation is necessary. Table 2.1 summarizes relevant recent works on wideband DPA from the literature.

Table 2.1: Summary of published wideband DPAs in literature

Year	**Technique**	**Freq (GHz)**	**Signal**	**Signal BW (MHz)**	**Avg P_{out} (dBm)**	**PAPR (dB)**	**Avg η , Peak η**	**Gain (dB)**	**PD**
2010 [10]	Mixed Signal	1.7 – 2.3	–	–	37	6.0	45.0%, 55.0%	13	YES
2011 [17]	Optimized DPA	1.7 – 2.6	–	–	37	6.0	45.0%, 50.0%	–	YES
2012 [5]	Modified Doherty	0.7 – 1.0	4C WCDMA	20	42.7	7.1	60.6%, 67.3%	>18	YES
2013 [13]	Mixed Signal	1.6 – 2.4	–	–	38	6	49.0%, 55.0%	9	YES
2013 [7]	Mixed Signal	1.0 – 3.0	WCDMA	5	36	6.7	44.5%, 40.0%	8	YES
2014 [12]	Dual-band	0.85/2.33	LTE−10 / LTE−15	10 / 15	31.7	9.0	32.0%, 41.0%	19/13	YES
2014 [16]	Modified Doherty	0.70 – 0.95	LTE−15 / WCDMA	15 / 15	33.5	9.4	48.0%, 51.0%	14	YES

2.3 Drain Modulation Technique

2.3.1 Basic Principle

Drain modulation technique modulates the drain biasing voltage of the PA as a function of the input power to improve the efficiency at power back-off by reducing DC power dissipation. Kahn's EER [3] combines drain modulation technique with high-efficiency nonlinear RF PAs to implement a highly efficient, linear transmitter. A simplified schematic of a Kahn's transmitter is shown in Figure 2.2. This technique is based on polar modulation rather than in-phase (I) and quadrature (Q) modulation. The phase modulated signal with a constant envelope is fed to the input of the PA while the envelope is mixed with the phase through the drain supply variation of the PA. Note that in this scenario, the PA will behave like a mixer which mixes the RF input signal with the drain supply voltage. The linearity of the overall transmitter is preserved by the linear output power versus drain supply relationship of the PA, as well as the constant input-output phase characteristics. As the PA is driven with maximum power at all times, ideally the efficiency of the PA will be preserved at power back-off. The phase and envelope signals are generated from the original I/Q signals using a coordinate rotation digital computer (CORDIC) algorithm as:

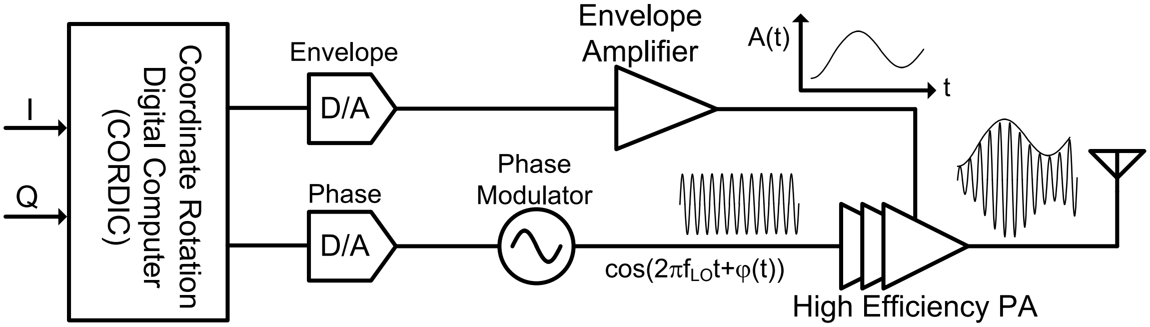

Figure 2.2: Simplified schematic of a Kahn's transmitter (EER technique).

$$a(t) = \sqrt{I(t)^2 + Q(t)^2}, \tag{2.1}$$

$$\phi(t) = tan^{-1}\left(\frac{Q(t)}{I(t)}\right). \tag{2.2}$$

In addition to preserving good back-off efficiency, Kahn's technique is an attractive choice for multi-standard PAs/transmitters. Multi-standard operation can be achieved through a multi-band or wideband PA with high peak efficiency, while the back-off efficiency is maintained through a supply modulator which is standard/signal independent.

Despite the aforementioned advantages, Kahn's technique suffers from four major drawbacks when dealing with modern wideband signals. First, the bandwidth of both the envelope and phase signals expands compared to the original I and Q signals due to the nonlinear transformation, which increases the bandwidth requirements of the PA and envelope modulator. Figure 2.3 shows the envelope and phase of a downlink LTE signal (centered at $740\,MHz$) with $20\,MHz$ bandwidth and $10.0\,dB$ PAPR, where the bandwidth of the envelope and phase signals are expanded 2 to 3 times compared to the original I and Q signals. Secondly, the required time alignment between the envelope and phase paths is very difficult to achieve, especially as the envelope and phase paths have completely different frequency scales. For modern modulation schemes, time alignment in the order of fractions of nano-seconds (ns) is required to meet the demanding linearity requirements. The third issue is the limited dynamic range of Kahn's technique. In order to achieve low output power in Kahn's technique, the drain supply voltage of the PA is lowered. Part of the PA's high input power leaks to the output of the PA, increasing the noise-floor of the transmitters. Finally, the fourth drawback is the efficiency of the transmitter, η, is limited by the efficiency of the envelope modulator and PA as follow:

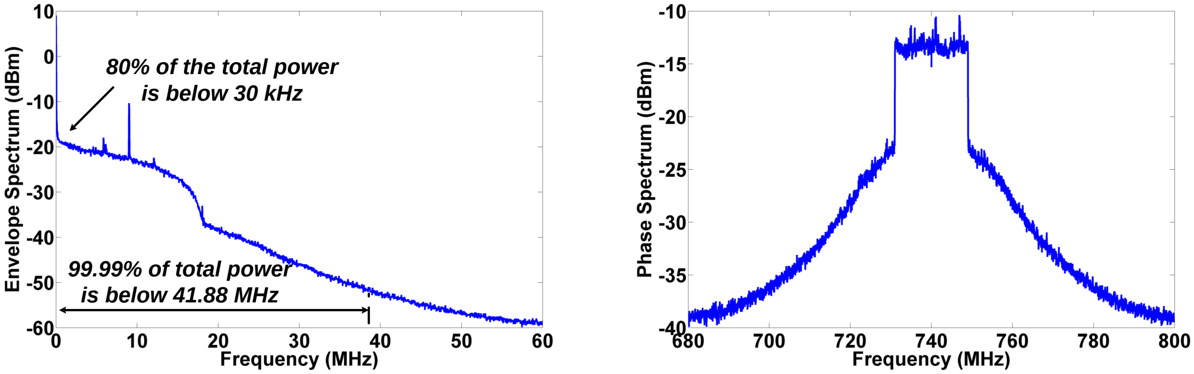

(a) Spectrum of the envelope signal.

(b) Spectrum of phase modulated signal.

Figure 2.3: Spectrum of the envelope and phase of downlink LTE signal with $20MHz$ bandwidth.

$$\eta = \eta_{PA} \cdot \eta_{EnvMod}, \tag{2.3}$$

where η_{PA} and η_{EnvMod} are the efficiency of the PA and the envelope modulator, respectively. It can be seen that the envelope modulator is a critical part of the transmitter. The main design criteria for envelope modulators are, bandwidth, slew rate and linearity (note that the overall linearity of the transmitter is limited by the linearity of the envelope modulator). These requirements typically contradict the efficiency of the envelope modulator which makes the design of envelope modulators more challenging.

An alternative solution to overcome some of the difficulties associated with Kahn's technique is ET, shown in Figure 2.4. In this technique, a linear PA is fed the I/Q modulated signal while the drain supply is modulated by the envelope signal to improve the efficiency of the PA at power back-off. The linearity of the overall transmitter is maintained through the linear PA, while drain supply modulation ideally will not affect the linearity. A very attractive aspect of this technique is that the drain supply does not need to follow the envelope signal accurately, which relaxes the requirements on the envelope modulator's linearity and time alignment. However, the bandwidth and efficiency of the envelope modulator still remain issues for ET PAs. Similar to EER technique, ET PAs can support multi-standard operation through a multi-standard or wideband high efficiency PA. In subsequent sections, recent developments in drain modulation technique will be discussed in further detail together with the main challenges and shortcomings of existing techniques.

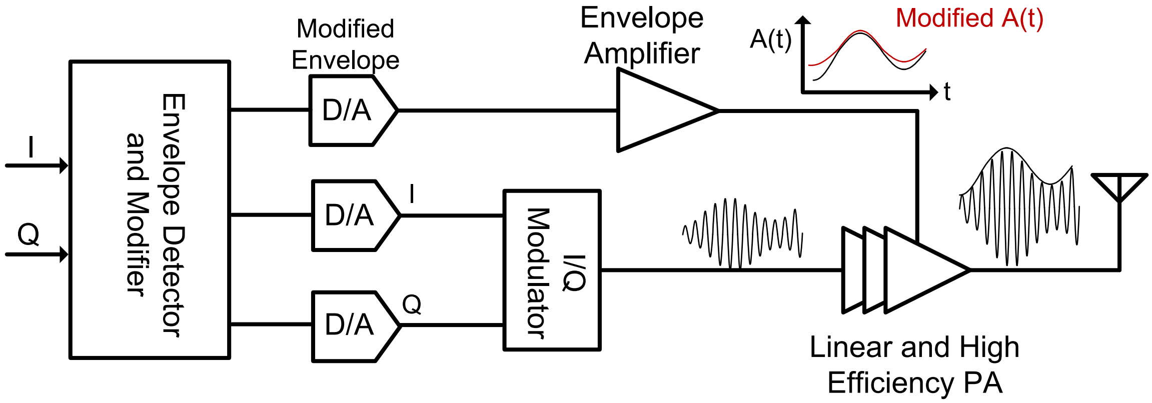

Figure 2.4: Simplified schematic of an ET PA.

2.3.2 Drain Modulation Technique in Literature

Envelope Elimination and Restoration in Literature

State of the art research on Kahn's EER transmitter (sometimes referred to as a polar transmitter) mainly focuses on variations of the original technique to improve its dynamic range and bandwidth. While polar transmitters are not popular for base stations due to their limited dynamic range, they have been applied for mobile transmitters as the linearity requirement is somewhat less stringent. Another advantage of polar transmitters is the lower power consumption and smaller silicon area as the modulator can be implemented using a voltage controlled oscillator (VCO) in a phased-locked loop (PLL). Some research on polar transmitters has investigated their implementation for modern communication systems. These publications do not usually focus on achieving the required output power, and they require an off-chip PA as the last stage (e.g. [18–20]). In this thesis, the focus is on the power amplification stage; hence only publications where PA has been implemented are discussed.

Most of the publications on polar transmitters target low PAPR and narrowband signals, such as enhanced data rates for GSM evolution (EDGE). A polar transmitter using a class-E PA with a low dropout (LDO) supply modulator was presented in [21] for GSM-EDGE signals with a PAPR of 3.4 dB. The complete transmitter was integrated in 0.18 μm CMOS technology with delay compensation to ensure the linearity requirements are met. Also, two polar transmitters using commercial class-AB PAs were published in [22, 23] for IS-95 CDMA and 8-PSK signals with a PAPR less than 2 dB. The efficiency for all of these techniques is lower than 35%. Few publications have shown polar transmitters successfully incorporating modern wideband signals. For example, in [24] a polar transmitter using class-E PA with class-G supply modulator was presented which achieved 24.5% average efficiency when transmitting a 64-QAM OFDM signal with a PAPR of 9 *dB*. However, the overall dynamic range and sensitivity to time-delay were not investigated in this paper. Another polar transmitter using current-mode class-D PA was presented in [25] for a WCDMA signal with a PAPR of 3.3 *dB*. The supply modulator was implemented using a buck converter and the transmitter achieved an overall efficiency of 26.5% at 24 *dBm* output power. The linearity of the transmitter was improved through DPD to meet the mask and error vector magnitude (EVM) requirements. The dynamic range of this transmitter was limited at low output power by the low-power linearity of the current-mode class-D PA used.

Furthermore, research has been conducted on variations of the polar transmitter trying to eliminate or reduce the non-ideal effects of the supply modulator. These techniques typically rely on switching the main PA ”ON” and ”OFF” to produce envelope variation rather than continuously modulating the drain supply voltage. In [26] the PA was switched through the drain supply voltage using a delta-sigma modulated (DSM) digitized envelope signal; hence eliminating the need for a linear envelope amplifier. The main drawback of this technique was the out-of-band quantization noise of the DSM digitized envelope signal which degraded the adjacent channel power ratio (ACPR) and dynamic range under high PAPR signals. This technique was employed for an IS-95A CDMA signal (PAPR of 3.3 *dB*) with an overall limited dynamic range of 11.3 *dB*. Another technique, investigated in [27, 28], was to switch a high efficiency PA from gate through an RF switch using a pulse-width modulated (PWM) envelope signal. In order to increase the dynamic range, the supply of the PA was varied based on the slow-varying average output power, called slow envelope power-level tracking (PT) technique. Although in [27, 28] good dynamic ranges were reported using this technique for CDMA-2000 and WCDMA signals (with 1.25 *MHz* and 3.84 *MHz* bandwidth respectively), this technique is not suitable for wideband and high PAPR signals, such as LTE. Another drawback of this technique is the filtering of the unwanted power generated at the harmonics of PWM frequency which was not discussed in [27, 28]. Table 2.2 presents a summary of all the relevant EER and polar transmitters from the literature. In summary, it can be concluded that there have not been any successful implementations of a multi-standard EER transmitter to support modern, high PAPR, wideband modulation schemes. Furthermore, there have not been an EER transmitter reported in the literature with the capacity to concurrently amplify multi-band signals.

Envelope Tracking in Literature

In recent publications, ET PAs are gaining more popularity for use in both base station [33–37] and mobile transmitters [38–49]. Research on ET PAs has focused on improving the efficiency

Table 2.2: Summary of published polar transmitters in literature

Year	**Technique**	**Freq**	**Signal**	**Signal BW (MHz)**	**Avg P_{out} (dBm)**	**PAPR (dB)**	**Avg η , Peak η**	**DR (dB)**	**PD**
2004 [29]	Polar loop	900 MHz	EDGE	0.384	29	4	35.0%, 54.0%	30	NO
2005 [21]	EER	1.75 GHz	EDGE	0.384	23.8	3.4	22.0%, 34.0%	7.7	YES
2007 [26]	Modified EER with DSM	836.5 MHz	IS-95A CDMA	1.25	22.1	3.3	31.0%, –	11.3	NO
2008 [30]	EER with Digital AM	1.56 GHz	64-QAN OFDM	20	14.7	10	7.2%, –	–	NO
2009 [31]	EER with Digital AM	1.90 GHz	EGDE	0.384	21.8	3.3	38.1%, 47.0%	30	YES
		1.92 GHz	WCDMA	5	21.7	3.4	38.2%, 47.0%	>70	YES
		1.92 GH	64-QAM WiMAX	5	15.3	9.8	22.0%, 47.0%	–	YES
2009 [24]	EER	2 GHz	64-QAM OFDM	20	19.6	10	22.6%, 69%	–	NO
2010 [27]	Pulsed EER	836.5 MHz	CDMA 2000	1.25	25	4.5	16.48%, 40%	80	NO
2011 [28]	EER with interleaved PWM	836.5 MHz	EGDE	0.384	26	3.3	45.5%, 68%	30	NO
		836.5 MHz	WCDMA	0.384	25	3.4	41.2%, 68%	80	NO
2014 [32]	EER	1.95 GHz	LTE-20	20	25.6	6.7	35.3%, –	–	NO

and linearity of the drain modulated PA while trying to accommodate wideband signals. The efficiency of the envelope modulator, and the nonlinear memory effects due to drain modulation, are the two major challenges facing wideband ET PAs. Two common techniques to improve the linearity and efficiency of both base stations and mobile ET transmitters, are, (i) optimizing the PA at low drain supply voltage (corresponding to back-off output power) and, (ii) shaping the envelope signal to reduce the knee voltage nonlinearities. Most recent publications employ these two techniques or variations of these techniques, to improve the performance of the ET PA. For example, authors in [40, 49] scaled and added offset to the original envelope signal to avoid the knee region of the transistor. This degraded the efficiency of the ET PA, however, it ensured linearity specifications would be met. Furthermore, authors in [49] implemented a sweet spot tracking technique to make sure the PA was operating at the optimum supply voltage for linearity at every power level. The optimum envelope shaping function was determined using system-level simulations. In [35], authors attempted to improve the efficiency of the ET PA for wideband signals by reducing the bandwidth of the envelope signal through digital signal processing. While [35] reduced the bandwidth of the envelope signal effectively using an iterative digital low-pass filtering, they failed to achieve good overall experimental results for their ET PA. Another issue with this technique is the added memory effects resulting from the filtering of the envelope signal.

An alternate approach was investigated in [50, 51] for both base station and mobile transmitters by combining ET and Doherty techniques to further improve the efficiency at back-off. In this technique the supply voltage of the main transistor was modulated through an envelope modulator (based on the envelope signal) before the auxiliary transistor was turned ”ON”. After the auxiliary transistor began conducting, the drain supply voltage would remain constant and efficiency enhancement was achieved through load modulation. While this technique showed good back-off efficiency enhancement, it suffered from the bandwidth limitations of DPA, making it less suitable for true multi-standard operation.

All implementations of ET PAs face the issues of added nonlinearity and memory effects associated with drain modulation. In the case of base station PAs, a common approach to the efficiency/linearity trade-off is to operate the PA in the efficient (but nonlinear) region and compensate for the nonlinearity through DPD or other linearization techniques. These linearization techniques typically involve modeling the PA as a nonlinear two-port network and applying the inverse of the nonlinearity in order to achieve an overall linear PA [34]. In the case of ET PAs, the PA has three ports, RF input, RF output and the drain supply voltage. As we move toward wider modulation bandwidth and multi-band signals, it will become vital to accurately model the added nonlinearity and memory effects due to drain supply variation.

Lastly, another challenge facing ET PAs is the concurrent amplification of multi-band signals. While authors in [46] presented a multi-standard ET PA, they did not investigate the concurrent signal transmission capability of the ET PA. Recently, attempts were made to design an ET PA for concurrent amplification of dual-band signals [52–55]. These publications do not include detailed analyses of efficiency and linearity and were limited to simulation results and/or measurements under single- or two-tone excitations. Table 2.3 and 2.4 summarize all relevant publications on ET PAs for mobile and base station applications, respectively.

Table 2.3: Summary of published ET PAs for mobile transmitters in literature

Year	**Technique**	**Freq**	**Signal**	**Signal BW (MHz)**	**Avg P_{out} (dBm)**	**PAPR (dB)**	**Avg η , Peak η**	**DR (dB)**	**PD**
2007 [39]	ET (Mobile)	2.1 GHz	WLAN OFDM	20	20	8.0	28.0%, 40.0%	–	YES
2009 [42]	ET (Moblie)	840 MHz	WCDMA	3.84	26.0	3.4	60.0%, –	10	YES
2009 [43]	ET (Moblie)	2.4 GHz	WLAN OFDM	20	11.7	10	40.0%, –	–	YES
2009 [50]	Doherty ET (Mobile)	1.88 GHz	WiBro	5	24.2	10.7	38.6%, –	11	YES
2011 [49]	ET (Mobile)	1.85 GHz	WCDMA	5	31.5	3.28	48.8%, –	–	NO
		1.85 GHz	LTE	10	28.9	7.4	42.2%, –	–	NO
2011 [48]	ET (Mobile)	2.5 GHz	LTE	20	30.0	6.0	45.0%, –	–	YES
2012 [56]	ET (Mobile)	2.5 GHz	LTE	20	29.0	6.6	43.0%, –	–	NO
2013 [57]	ET (Mobile)	1.85 GHz	LTE	10	26.0	7.5	34.1%, –	–	NO
2013 [58]	ET (Mobile)	1.7-2.0 GHz	LTE	10	27.0	7.5	39.5%, –	–	NO
2013 [59]	ET (Mobile)	1.74 GHz	LTE	10	27.0	6.44	39.8%, –	–	NO
2013 [60]	ET (Mobile)	2.53 GHz	LTE	20	28.3	6.7	48.0%, –	–	NO
2013 [61]	ET (Mobile)	0.7-1.0 GHz	LTE-5	5	28.1	7.5	42.3%, –	–	NO
		0.7-1.0 GHz	LTE-10	10	28.1	7.5	41.1%, –	–	NO
		0.7-1.0 GHz	LTE-20	20	27.9	7.5	40.2%, –	–	NO

2.4 Advanced RF Transmitter Architectures

2.4.1 Basic Principle

The efficiency enhancement techniques discussed above all attempt to improve the overall efficiency of the PA at power back-off while trying to accommodate multi-standard and multi-mode operation through analog and RF techniques. Techniques such as Doherty and ET require a multi-standard I/Q modulator to achieve a true multi-standard transmitter. These techniques fit well with the current homodyne transmitters with no need for significant changes to existing transmitter architecture. However, greater flexibility for true multi-standard transmitters can be

Table 2.4: Summary of published ET PAs for base station transmitters in literature

Year	Technique	Freq	Signal	Signal BW (MHz)	Avg P_{out} (dBm)	PAPR (dB)	Avg η , Peak η	DR (dB)	PD
2006 [33]	ET (BTS)	2.14 GHz	WCDMA	5	45.7	7.6	50.7%, –	–	YES
2008 [40]	ET (BTS)	1.0 GHz	WCDMA	5	29.2	9.8	35.5%, –	–	YES
2009 [36]	ET (BTS)	2.14 GHz	WCDMA	5	45.2	7.7	55.0%, –	–	YES
		2.14 GHz	WCDMA	5	41.9	11.2	49.0%, –	–	YES
		2.14 GH	WiMAX	10	43.9	8.8	48.0%, –	–	YES
2009 [35]	ET (BTS)	2.14 GHz	WCDMA	5	44.7	7.6	54.0%, –	–	YES
2011 [37]	ET (BTS)	3.54 GHz	LTE	10	40.0	8.5	39.6%, –	–	YES
2012 [62]	ET (BTS)	2.14 GHz	WCDMA	4	34.0	7.7	49.0%, –	–	YES
2013 [63]	ET (BTS)	2.6GHz	LTE	10	40.8	8.5	46.4%, –	–	YES
2013 [64]	ET (BTS)	0.89 GHz	LTE	5	40.0	6.5	59.7%, –	–	YES

achieved by using inherently flexible digital circuits in the majority of the hardware. Research efforts over the last few years have focused on moving the digital-to-analog interface in transmitters as close as possible to the antenna to leverage the flexibility of the digital circuits. Various approaches have been investigated to tackle this problem. Here, we discuss three popular techniques: fully digital RF modulators, switched-mode PA (SMPA) systems, and Chireix outphasing technique.

Fully Digital RF Modulator

Fully digital RF modulators combine the functionality of digital-to-analog converters (DAC), up-conversion mixers and unwanted sideband rejection filters into one digitally controlled circuit. Such digital-centric circuits are commonly referred to as RF-DACs. One common approach employs weighted quadrature digital-to-RF converter cells to construct a mulit-bit RF-DAC [65], shown in Figure 2.5. The digital-to-RF converter cell functions like a Gilbert mixer; the filtering of unwanted sidebands and image frequency is done through a resonator at the output. Similar to a conventional current-steering DAC, an array of parallel digital-to-RF converter units can be implemented using a combination of unitary and binary weighted cells, called segmentation [65]. The segmentation level between the most significant bits (MSB) and the least significant bits (LSB) partitions regulates the trade-off between RF-DAC linearity, complexity, and sensitivity to mismatch between the cells.

An alternate approach to RF-DAC employs a delta-sigma modulator to convert the multi-bit I/Q data into single-bit high speed pulses which will be fed to a quadrature digital RF converter [66]. This technique reduces the circuit complexity of the RF-DAC, however, out-of-band

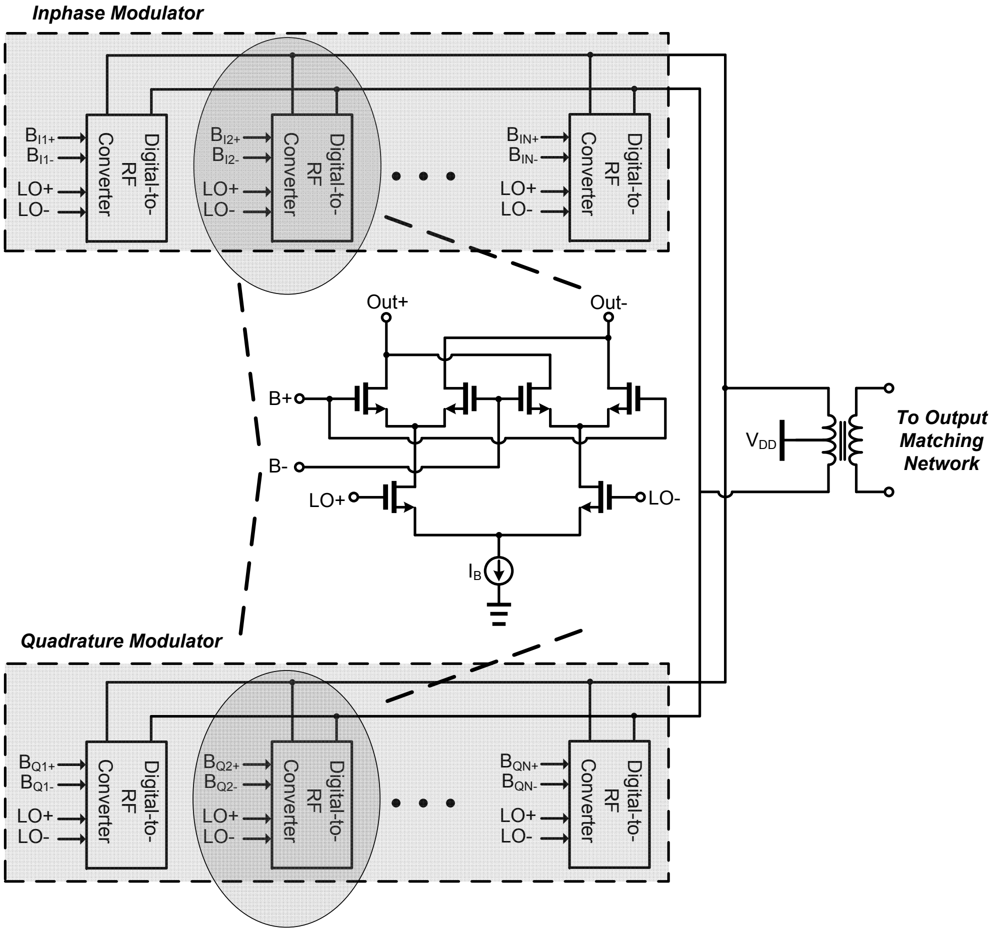

Figure 2.5: Simplified schematic of an RF-DAC using a weighted digital-to-RF converter.

quantization noise and the high oversampling ratio of the delta-sigma modulator makes designing the output filter and quadrature modulator more challenging. The main drawbacks of both techniques is efficiency degradation at power back-off and low output power. Most of the publications about RF-DAC fail to achieve watt-level output power, which is needed for mobile transmitters, and hence require the addition of an off-chip multi-standard high efficiency PA.

Switched-Mode Power Amplifier System

Another approach to the fully digital transmitter problem benefits from the high efficiency of SMPAs. The general architecture, shown in Figure 2.6, contains two functional blocks: a sig-

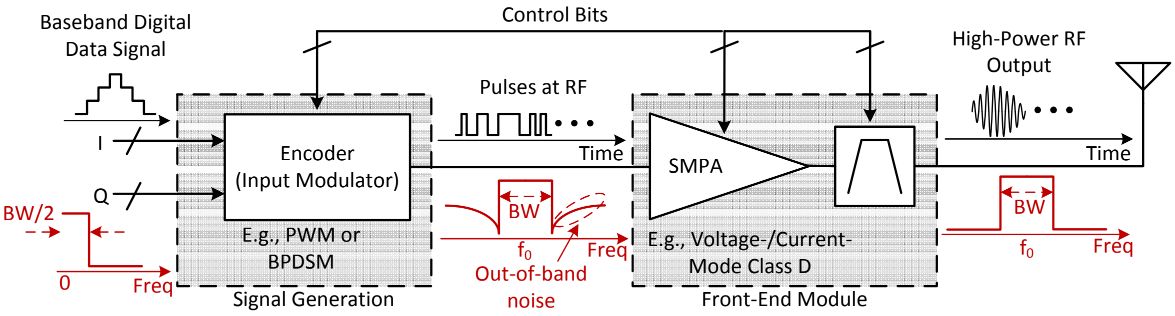

Figure 2.6: Simplified schematic of switched-mode PA system.

nal generation block, and a front-end module which includes an SMPA and filter. The signal generation block (also called a time-domain encoder) encodes the I/Q information in the timing of high frequency pulses. The output of the signal generation block provides the switching waveforms for the SMPA that already contain within its spectrum the I/Q modulated information centered at the RF carrier. As today's integrated circuit (IC) technology advances, with their ever increasing transition frequency (f_T), greater precision of pulse timings improves the accuracy and dynamic range of time-domain encoders. Two common time-domain encoding methods are bandpass DSM and RF pulse-width/position modulation (PWPM).

Band-pass DSM improves the dynamic range in time-domain through oversampling and shaping quantization noise away from the signal band. The main drawbacks of this technique are the high sampling frequency (typically four times the carrier frequency) and out-of-band quantization noise. The out-of-band quantization noise causes added losses in the SMPA which reduces the overall efficiency and imposes stringent requirements on the filter after the PA. PWPM encodes the amplitude and phase information of the signal in pulse-width and position (i.e. duty cycle and time-delay), respectively. Unlike band-pass DSM, PWPM does not generate close-band noise or distortion (only powers at harmonics), hence, it relaxes the filtering requirement and reduces the losses. It should be noted that both DSM and PWPM encoders have difficulty achieving adequate dynamic range for high data-rate base stations and mobile transmitters.

The front-end module consists of a highly efficient SMPA and an output filter to suppress the quantization/harmonic power from the digital encoding scheme. All common SMPA classes can be used, including class-E and voltage-/current-mode class-D. Theoretically, all these classes provide 100% efficiency for a 50% duty cycle pulse where the transistors are operating as switches. The purpose of the filter at the output of the SMPA is to recover the RF signal and filter the out-of-band power. This means the out-of-band quantization noise and spectral characteristics of the time-domain encoder are important parameters when designing the output filter.

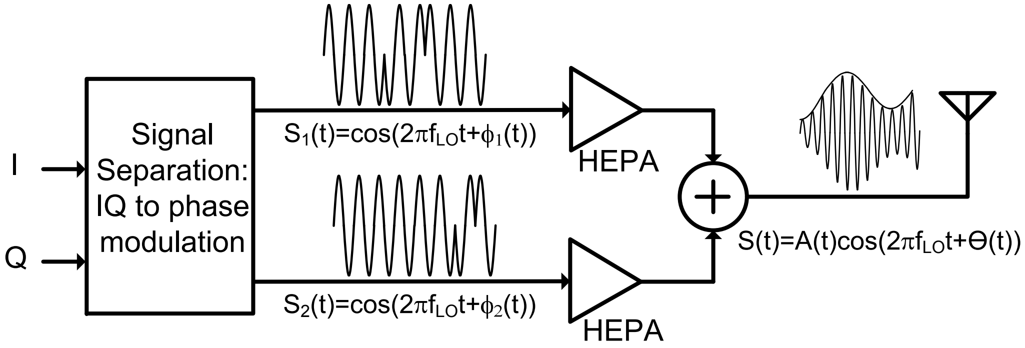

Figure 2.7: Simplified schematic of Chireix outphasing transmitter.

Chireix Outphasing Technique

The outphasing technique, first introduced by Chireix in 1935 and later renamed linear amplification with nonlinear components (LINC) [67,68], decomposes an amplitude and phase modulated signal, $S(t)$, into two phase modulated signals, $S_1(t)$ and $S_2(t)$.

$$\begin{cases} S_1(t) = 0.5\cos\left(\omega_0(t) + \theta(t) + \cos^{-1}(a(t))\right), \\ S_2(t) = 0.5\cos\left(\omega_0(t) + \theta(t) - \cos^{-1}(a(t))\right), \end{cases} \tag{2.4}$$

$$S(t) = S_1(t) + S_2(t) = a(t)\cos(\omega_0(t) + \theta(t)). \tag{2.5}$$

As the two signals have constant amplitudes, they can be efficiently amplified by an efficient nonlinear PA and then combined to construct the original I/Q modulated signal. A simplified schematic of a Chireix outphasing amplifier is shown in Figure 2.7. It has been shown that the outphasing modulator can be implemented completely using digital circuits, for example using a digitally controlled oscillator and digital phase rotators [69], which makes it suitable for use in fully digital transmitters. However, the main drawbacks of this technique are the limited dynamic range and the associated loss of the power combiner, limiting the application of this technique for modern wideband signals.

2.4.2 Digital RF Transmitters in Literature

Fully Digital RF Modulator in Literature

The main focus of research on fully digital RF modulators or RF-DACs is to improve the bandwidth and dynamic range of current modulators through combining delta-sigma modulation and a weighted array of RF modulators. Recent publications show good experimental results for multi-standard fully digital RF modulators [65, 66, 70–79]. While these techniques can support wideband high PAPR signals, they suffer from low output power (typically $0-5\,dBm$) and low efficiency (less than 10% for modern signals). Few publications on fully digital RF modulators achieve watt-level output power. For example, authors in [80] employed an array of power mixers to mix the envelope signal with the phase modulated carrier signal. They achieved average efficiency of 20% for a WiMAX signal with a PAPR of $8.5\,dB$, and a peak output power of $30\,dBm$ in a $0.13\,\mu m$ CMOS process. The back-off efficiency was improved in [80] using segmented power generation where part of the power mixer units are turned off for small output power. It should be noted that most publications on fully digital RF modulators demonstrate the capability to support multiple standards, however, they typically have narrowband carrier frequency range (less than 10% fractional bandwidth). Furthermore, concurrent amplification of multi-band signals using fully digital RF modulators has not been investigated in the literature.

Switched-Mode Power Amplifier System in Literature

The state of the art research on SMPA systems focuses on improving the dynamic range of the transmitter for today's communication signals. Most of the publications use variations of DSM to generate the high frequency pulses to achieve required the dynamic range while trying to minimize the out-of-band quantization noise. Coding efficiency, defined as the ratio of the desired signal power to the overall power, is a measure of out-of-band quantization noise for DSM signals. It has been shown that coding efficiency can reduce the overall efficiency of an SMPA system significantly [81–83]. Some publications employ PWPM technique for the time-domain encoder [84–88]. These technique are limited by the minimum pulse-width and timing accuracy of the modulator and SMPA. Due to the limited dynamic range of the SMPA and time-domain coding techniques, this approach has been limited to low PAPR signals in the range of $3-5\,dB$. Furthermore, SMPA systems are not capable of concurrent amplification of multi-band signals, making them unsuitable for carrier aggregated signals such as LTE-A.

Chireix Outphasing Technique in Literature

While Chireix outphasing technique is attractive for high efficiency multi-standard transmitters, most of the implementations presented in the literature are either narrowband, inefficient or have limited dynamic range. However, recent publications have shown the ability to accommodate up to $5\,MHz$ bandwidth with improved dynamic range through modifications to the original outphasing technique [89–91]. For example, authors in [91] improved the dynamic range of the transmitter by adding discrete PWM to the input of a high efficiency class-E PA. In another publication [90], authors tackled the limited dynamic range of the transmitter through discrete drain supply variation for the high efficiency PA. They achieved 41% average efficiency for a $40\,MHz$ 16-QAM signal with a PAPR of $6.5\,dB$. However, the overall dynamic range of the transmitter was not reported. In spite of good results in recent publications, Chireix outphasing technique is less tempting for a true fully digital multi-standard transmitter due to aforementioned dynamic range limitations. Table 2.5 provides a summary of recently published fully advanced RF transmitter architectures, including RF-DACs, SMPA system and Chireix outphasing techniques.

2.5 Summary

A detailed literature review of efficiency enhancement techniques was presented in this chapter. A review of recent publications shows that ET and Doherty techniques have the most potential to be employed in future highly linear concurrent multi-band multi-standard base stations and mobile transmitters. Other techniques, such as Chireix outphasing and the SMPA system, have shown good initial steps toward truly digital transmitters for low PAPR signals; however, accommodating the high PAPR and stringent linearity requirement of today's modern signals for truly concurrent multi-band and multi-standard transmitters will require further research and state-of-the-art RF, analog and digital circuit and system techniques.

Doherty technique, while popular for base station transmitters, requires complicated passive circuits, making it less suitable for integrated mobile transmitters. ET PAs, on the other hand, have attracted researchers interested in both integrated mobile and high power base station transmitters. The major drawback of the ET PA is its capacity to accommodate concurrent multi-band signals, due to the bandwidth limitation of the envelope amplifier. In this thesis, the suitability of ET PAs for concurrent amplification of multi-band and carrier aggregated signals is investigated. In the next chapter, sources of nonlinearity and memory effects in single-band and multi-band constant supply and drain modulated PAs will be analyzed. This analysis will prove crucial for successful implementation of concurrent multi-band ET PAs.

Table 2.5: Summary of published advanced RF transmitter architectures in literature

Year	**Technique**	**Freq**	**Signal**	**Signal BW (MHz)**	**Avg P_{out} (dBm)**	**PAPR (dB)**	**Avg η , Peak η**	**DR (dB)**	**PD**
2007 [85]	BPDSM H-Bridge Class-D	800 MHz	IS-95 CDMA	1.25	15.5	5.5	33%, 62%	–	NO
2007 [65]	Direct Digital Quad Mod	1.76 GHz	EDGE	0.2	-0.2	3	–, –	–	NO
		1.92 GHz	WCDMA	3.84	-2	3.5	–, –	60	NO
		1.9 GHz	WLAN	16.6	-9	10	–, –	–	NO
2008 [92]	Digital Polar	1.5 GHz	WLAN OFDM	20	17	–	14%, –	–	NO
2008 [75]	DSM RF DAC	2.4–2.7 GHz	64-QAM OFDM	17	2.6	–	–, –	38	NO
2008 [86]	Polar DSM Class-D	2.4 GHz	8-PSK	3	11	3	30.0%, 38.5%	–	NO
2008 [89]	Outphasing Sat. Class-B	900 MHz	GSM	0.384	16.4	3.6	49.0%, 56.0%	–	NO
		900 MHz	EGDE	0.384	13.6	6.4	39.0%, 56.0%	–	NO
		900 MHz	WCDMA	3.84	13.0	7.0	27.0%, 56.0%	–	NO
2009 [77]	Direct Quad Mod	1.95 GHz	WCDMA	3.84	4.0	8.0	10%, –	80	NO
2009 [93]	All-Digital DSM	1.0 GHz	WCDMA	3.84	-4.0	8.0	–, –	–	NO
2009 [87]	PWPM Class-E	2.2 GHz	$\frac{\pi}{4}$-DQPSK	0.192	26.7	4	21.0%, 28.5%	–	NO
2009 [80]	Power Mixer Array	1.75–1.95 GHz	WCDMA	3.84	25.3	5.2	20.0%, 43.0%	–	NO
		1.75 GHz	WiMAX	10	25.0	8.5	20.0%, 43.0%	–	NO
2011 [88]	BPDSM Class-D	800 MHz	EDGE	0.27	10.5	3.5	62.0% 75.0%	–	NO
		800 MHz	IS-95 CDMA	1.25	8.5	5.5	55.0%, 75.0%	–	NO
2011 [94]	Digital Polar Class-D	2.25 GHz	WLAN OFDM	20	14.0	8	18.0%, 44.0%	–	YES
2012 [95]	Multilevel Outphasing	2.4 GHz	OFDM	20	20.1	7.5	27.6%, 45.1%	–	YES

Chapter 3

Linearity Analysis of Single-Band and Multi-Band PAs

3.1 Introduction

Traditionally, base station PAs for macro- and micro-cells, are operated in their efficient, but nonlinear, region to improve the overall efficiency of the transmitter. Subsequently, the PA nonlinearities are modeled and compensated for using DPD techniques [96]. As the bandwidth of the modulated signal increases to accommodate higher data rates, the PA dynamic nonlinearities, commonly referred to as memory effects, become dominant yielding significant added complexity for the DPD model and implementation. This also increases the power overhead associated with linearizing the PA. When we move from single-band modulated signals toward multi-band and carrier aggregated signals, DPD models including memory effects will be even more complicated. In the case of macro- and micro-cell base stations, the added power overhead associated with the linearization, typically in the order of $1-2\,W$, can be tolerated. However, as we move toward smaller cell sizes, such as pico- and femto-cells, the power dissipation of DPD becomes a significant proportion of the overall power dissipation of the PA. Hence, it is important to reduce the complexity of DPD models. One way in which this can be achieved is by minimizing the sources of memory effects in PAs from the circuit design stage so that simple DPD models, such as look-up tables (LUT) and memoryless polynomials, are sufficient to linearize the PA.

In this chapter, a detailed analysis of sources of static and dynamic nonlinearities in single-band and multi-band PAs will be presented. This study will help designers to reduce the sources of nonlinearities, particularly memory effects, from the circuit design stage. Using the analysis in this chapter, a design guideline has been devised to reduce and mitigate sources of memory effects in gallium nitride (GaN) high electron mobility transistor (HEMT) PAs. The study is validated using the measurements of a 45 W GaN PA, designed to minimize the sources of memory effects. The PA is linearized using memoryless polynomial DPD when driven with single-band and dual-band modulated signals. Note that while the analysis is conducted for a GaN PA, it can be generalized to other transistor technologies, such as laterally diffused metal oxide semiconductor (LDMOS) and gallium arsenide (GaAs) transistors.

3.2 Device Technology

It is important to study and analyze different transistor technologies for high power high frequency PAs. The transistor is typically the bottleneck of high power PAs in terms of efficiency, linearity, output power and gain. Inherent parasitics and nonidealities of the transistor can determine an upper limit on the performance of the PAs designed using such transistors. GaN HEMTs and LDMOS transistors are the two dominant transistor technologies for high power PAs suitable for base station infrastructures. Low power mobile PAs employ other transistor technologies such as GaAs heterojunction bipolar transistors (HBTs), silicon germanium (SiGe) HBTs and silicon on insulator (SOI) CMOS transistors. This thesis focuses on base station infrastructure applications, therefore, only GaN HEMT and LDMOS devices will be discussed.

Presently, LDMOS transistors are the dominant technology of choice for base station PAs, especially at 600 MHz to 2 GHz, due to their low cost and high breakdown voltage. On the other hand, GaN HEMT technology is gaining more and more interest for use in high power, high frequency PAs due to its even higher breakdown voltage, higher transition frequency (f_T), and power density. Despite the higher fabrication cost of GaN HEMT technology, the aforementioned benefits of this technology make it an attractive technology for high power PAs operating beyond 3 GHz for future applications such as 4G and 5G.

3.3 Simplified FET-Based Nonlinear Transistor Model

Figure 3.1 shows an equivalent circuit model outlining the key components that contribute to the static and dynamic nonlinearities in a PA. A transistor's sources of nonlinearity are:

- nonlinear DC-I/V (modeled as a nonlinear controlled current source, $i_{DS}(v_{GS}, v_{DS})$),
- nonlinear input, output and feedback capacitances.

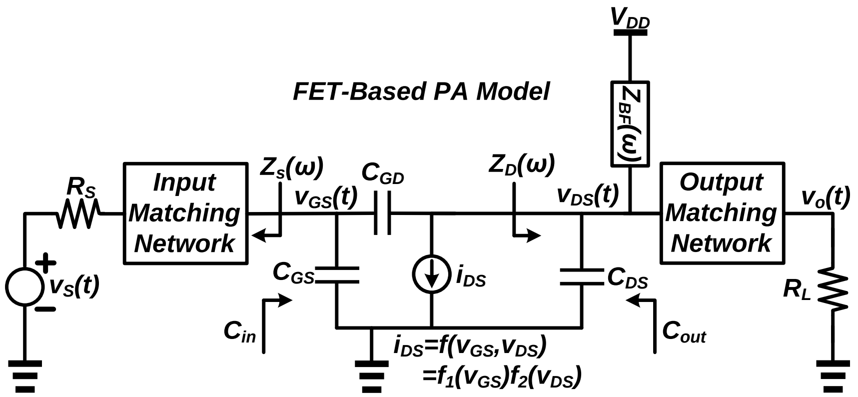

Figure 3.1: Equivalent nonlinear circuit model for an RF PA.

The input matching network is modeled using the source impedance, $Z_S(\omega)$, and the output matching network is modeled using the biasing feed impedance, $Z_{BF}(\omega)$, and the overall output impedance, $Z_D(\omega)$. This equivalent model will be used throughout this thesis to analyze nonlinearity mechanisms in PAs. The model does not include sources of nonlinearities due to thermal and trapping effects of the transistor. The impact of thermal and trapping effects on the dynamic nonlinearity of the PA will be discussed separately. It should be noted that the goal of this analysis is not to find an exact analytical solution, but rather to provide insights into nonlinearity mechanisms in PAs in order to mitigate nonlinearity from the circuit design stage. Hence, at different points throughout the analysis, appropriate approximations and/or simplifications will be employed to decrease the complexity of the analysis. Also, where appropriate, simulation results will be used to illustrate the effect of transistor nonlinearity on the performance of the PA.

In the most general case, all of the capacitances, C_{GS}, C_{DS} and C_{GD}, are nonlinear functions of both v_{GS} and v_{DS}; however, in the case of GaN HEMT devices (from now on simply referred to as GaN transistors), we can assume the drain-source capacitance is linear, and C_{GS} and C_{GD} are solely a function of v_{GS} and v_{GD}, respectively. Figure 3.2 shows the extracted gate-source, gate-drain and drain-source capacitances of a $45\,W$ GaN transistor (Cree CGH40045F). The equivalent input and output capacitances of the nonlinear transistor are calculated using the miller-effect [97] as,

$$C_{in} = C_{GS} + C_{M,in} = C_{GS} + (1 - \frac{dv_{DS}/dt}{dv_{GS}/dt})C_{GD}. \tag{3.1}$$

$$C_{out} = C_{DS} + C_{M,out} = C_{DS} + (1 - \frac{dv_{GS}/dt}{dv_{DS}/dt})C_{GD} \simeq C_{DS} + C_{GS}. \tag{3.2}$$

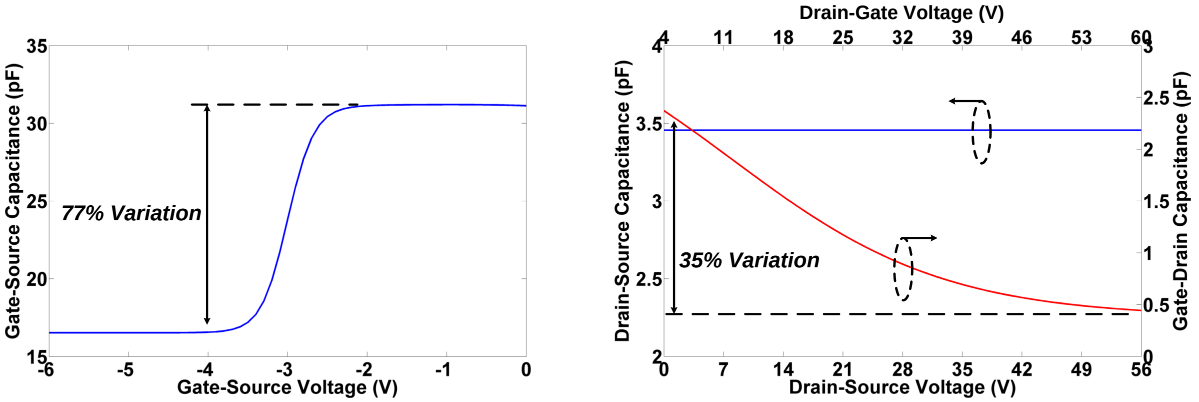

(a) Gate-source capacitance

(b) Gate-drain and drain-source capacitances

Figure 3.2: The nonlinear CV profile of gate-source, gate-drain and drain-source capacitances of a $45\,W$ GaN transistor.

It is evident from (3.2) that the equivalent output capacitance of a GaN transistor is dependent on v_{DS}. When the transistor is operating away from the knee region, it can be assumed that the input capacitance is only a function of v_{GS} as the dependency of C_{GD} on v_{DS} is weak. As the transistor begins to operate close to the knee region, this assumption will no longer be valid.

At this point it is important to define and distinguish between ”mild” and ”harsh” nonlinearity in PAs. When the transistor operates in the knee region, the PA is said to be exhibiting ”strong” nonlinearity due to the harsh DC I/V nonlinearity in that region. Other sources of nonlinearity in GaN transistors, such as nonlinear transconductance, nonlinear gate-source and gate-drain capacitances can be considered ”mild”. The impact of ”mild” nonlinearities on the behavior of the PA can be compensated for using techniques such as DPD. However, compensating for the ”harsh” nonlinearities is difficult and impractical in some cases. This is especially true as we move toward wideband modulated signals where the sources of memory effects when operating in the knee region become even more significant.

3.4 Sources of Quasi-Static Nonlinearity in Single-Band PAs

In order to analyze the sources of nonlinearity in single-band PAs, we start with an analysis of the nonlinear PA when driven with a single-tone sinusoidal excitation:

$$v_S(t) = V_S \cos(\omega_0 t + \theta_0). \tag{3.3}$$

The fundamental component of the output signal (i.e., around ω_0) can be written as:

$$v_o(t) = V_o(V_S)\cos(\omega_0 t + \theta_0 + \phi(V_S)), \tag{3.4}$$

where the amplitude and phase of the output signal are nonlinear functions of the input signal magnitude, V_S. Typically, nonlinear circuits under single-tone excitation are modeled through their amplitude-amplitude (AM/AM) and amplitude-phase (AM/PM) responses. Note that this assumes that the dependency of the output amplitude and phase on the input phase is negligible (i.e., no PM/AM and PM/PM) [98]. Furthermore, it is assumed that the harmonics at the output can be adequately filtered to meet the spectrum mask requirements prior to the signal being transmitted to the antenna.

Before discussing the sources of AM/AM and AM/PM nonlinearities in PAs, it is necessary to define the problem clearly and present the basic terminology which will be employed throughout this thesis. The analysis has been conducted with a single-tone input in a steady-state condition and phasor notation has been used throughout for simplicity. For example, the time-domain drain-source voltage and its corresponding phasor are expressed as,

$$\begin{aligned} v_{DS}(t) &= V_{DS0} + V_{DS1}\cos(\omega_0 t + \phi_{DS1}) \\ &\quad + V_{DS2}\cos(2\omega_0 t + \phi_{DS2}) + \ldots, \\ V_{DS}(\omega) &= \left[V_{DS0},\, V_{DS1}e^{j\phi_{DS1}},\, V_{DS2}e^{j\phi_{DS2}},\, \ldots\right]. \end{aligned} \tag{3.5}$$

Unless otherwise stated, the nonlinearity profiles of capacitors are approximated as a truncated power series, such as,

$$C_{in}(v_{GS}) \simeq C_{in0} + C_{in1}v_{GS} + C_{in2}v_{GS}^2. \tag{3.6}$$

While employing a truncated power series to model the capacitor is not a truly accurate representation in the case of strongly nonlinear capacitor, it does provide useful insights into the nonlinearity generation mechanisms. The nonlinear controlled current source has been modeled as a two-dimensional nonlinearity as in,

$$\begin{aligned} i_{DS}(v_{GS}, v_{DS}) &= f_1(v_{GS})f_2(v_{DS}) \\ &= f_1(v_{GS}) + f_1(v_{GS})\hat{f}_2(v_{DS}). \end{aligned} \tag{3.7}$$

where, $\hat{f}_2(v_{DS}) = f_2(v_{DS}) - 1$. For example in the case of the Angelov model [99], both $f_1(v_{GS})$ and $f_2(v_{DS})$ include tanh(.) nonlinearity. Note that, away from the knee region, the controlled current source can be adequately modeled as,

$$i_{DS}(v_{GS}, v_{DS}) \simeq f_1(v_{GS})\,(1 + \lambda v_{DS}). \tag{3.8}$$

In the following subsections, the sources of amplitude and phase distortion in PAs will be discussed. It should be emphasized again that the goal of this analysis is not to derive a closed-form analytical model for the single-band PA; whereas the aim is to provide insight into the sources of nonlinearity mechanism in GaN PAs and ways to mitigate those distortions from the circuit design stage.

3.4.1 Amplitude Nonlinearity – AM/AM

Conventionally, AM/AM distortion in a PA is attributed to nonlinear DC-I/V of the transistor (which includes nonlinear transconductance and knee voltage). A typical AM/AM plot of a PA exhibits a linear region at low power (i.e., constant gain) and gain compression close to peak power. However, it is observed in practice that GaN PAs tend to exhibit gain compression at large power back-off and compress more slowly compared to LDMOS PAs. The main disadvantage of slow compressing PAs is that they cannot be linearized by simply backing-off the input power. In this section we attempt to analyze sources of AM/AM in GaN PAs to fully understand the causes of slow compression.

Using the simplified model shown in Figure 3.1, we can approximate the voltage gain, G_V, of the PA as,

$$G_V = \frac{fund\,(v_{DS}(t))}{fund\,(v_S(t))} \simeq \frac{V_{GS}(\omega_0)}{V_S(\omega_0)} \left(\frac{-I_{DS}(\omega_0)}{V_{GS}(\omega_0)} \right) Z_D(\omega_0). \tag{3.9}$$

Using the voltage gain and neglecting the losses associated with input/output matching networks, the power gain, G_P, is subsequently determined as,

$$G_P = \frac{P_{out}}{P_{AVS}} = 4\frac{Re(Z_S(\omega_0))Re(Z_D(\omega_0))}{|Z_D(\omega_0)|^2}|G_V|^2, \tag{3.10}$$

where $Re(.)$ denotes the real part of a complex number. Rewriting (3.9) we have,

$$G_V \simeq -G_{Vin}.G_m.Z_D(\omega_0), \tag{3.11}$$

where G_m and G_{Vin} are the large-signal transconductance and the voltage gain of the input matching network, respectively. G_m and G_{Vin} are defined as:

$$G_{Vin} = \frac{V_{GS}(\omega_0)}{V_S(\omega_0)}, \tag{3.12}$$

$$G_m = \frac{I_{DS}(\omega_0)}{V_{GS}(\omega_0)}. \tag{3.13}$$

Examining (3.11) shows that there are two possible sources of amplitude distortion; DC-I/V (G_m) and nonlinear input capacitance (G_{Vin}).

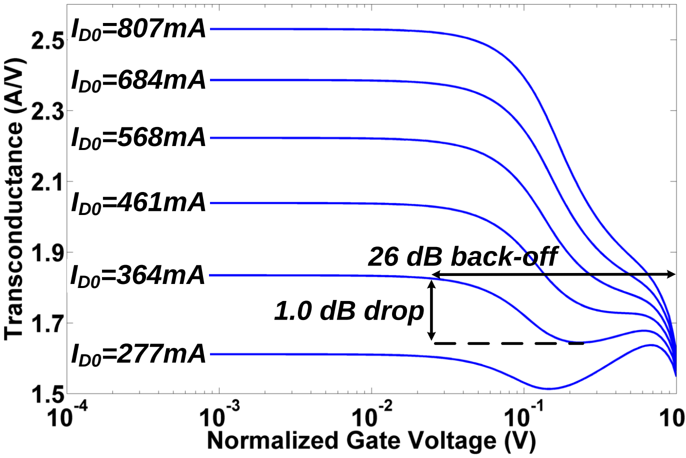

Figure 3.3: Simulated $G_{m,SC}$ of a 45 W GaN transistor at different bias currents versus gate voltage.

Nonlinear DC-I/V $- G_m$

As stated earlier, the DC-I/V nonlinearities include nonlinear transconductance and the knee region. As the drain-source voltage of the transistor enters the knee region at high output power, gain starts to compress rapidly. This is the main contributor to rapid gain compression at high power for GaN PAs (or any other PA), and is considered to be ”harsh” nonlinearity and difficult to linearize using DPD. With no knee region intrusion, however, the AM/AM profile of the PA is determined by the device transconductance (refer to (3.8)). The short-circuit large-signal transconductance of a transistor is defined as,

$$G_{m,SC} = \frac{I_{DS}(\omega_0)}{V_{GS}(\omega_0)}, \tag{3.14}$$

where the drain is AC short-circuited (i.e., $V_{DS}(\omega_0, 2\omega_0, ...) = 0$) and the transistor is fed using a pure sinusoid at the gate. Figure 3.3 shows the simulated $G_{m,SC}$ of a $45\,W$ GaN transistor at different biasing currents. It can be seen that, the $G_{m,SC}$ of a GaN transistor exhibits nonlinearity as far as $26\,dB$ back-off which contributes to slow compression of the AM/AM characteristic.

Nonlinear Input Capacitance $- G_{Vin}$

Nonlinear input capacitance affects both the AM/AM and AM/PM of the PA by distorting both the amplitude and phase of the gate-source voltage. The extent to which AM/AM and AM/PM are affected is a strong function of the nonlinearity profile of the input capacitance, as well as harmonic termination at the gate, however, typically the effect of nonlinear input capacitance on AM/PM is more pronounced. It is important to note that in the case of GaN transistors, the input second harmonic termination greatly effects both the AM/AM and AM/PM, thus, its effect on the linearity of a GaN PA will be discussed separately. The input capacitance nonlinearity is the result of the nonlinear gate-source capacitance, C_{GS}, and the nonlinear miller capacitance, C_M. We will consider the effects of the nonlinear capacitances separately, starting with the nonlinear C_{GS}.

The C_{GS} nonlinearity in GaN transistors is symmetrical around the pinch-off voltage. It can be shown that the effect of C_{GS} nonlinearity on the AM/AM and AM/PM will be negligible (ideally zero) if the even harmonics are short circuited at the intrinsic gate and the transistor is biased at the pinch-off voltage (i.e., $V_{GS0} = V_P = -3\,V$). As the biasing voltage moves away from the pinch-off voltage, and/or the second harmonic is not short circuited, the effect of the nonlinear C_{GS} on the AM/AM and AM/PM becomes significant. While it is possible to short circuit it at the intrinsic gate for a narrow bandwidth, it is not practical to short circuit the second harmonic at the intrinsic gate over a wide bandwidth. Furthermore, in case of high power packaged transistors (such as $45\,W$ GaN transistors), the package parasitics will make it practically impossible to short circuit the second harmonic at the intrinsic gate. Simulation results of a packaged $45\,W$ GaN transistor show that the amount of AM/AM added due to nonlinear C_{GS}, without the right harmonic termination, will be less than $0.15\,dB$ when the transistor is biased at the onset of the pinch-off voltage. Figure 3.4 shows the variation of G_{Vin} when the transistor is biased at the pinch-off voltage at $2.5\,GHz$ and the second harmonic at the source is terminated with an open circuit. Note that the amount of AM/AM will increase significantly (close to $1\,dB$) when transistor is not biased at the pinch-off voltage.

The nonlinearity of the miller capacitance, C_M, is the result of nonlinear C_{GD} and the nonlinear gain of the transistor (i.e., nonlinear G_m). Unlike the nonlinear C_{GS}, C_M will affect both AM/AM and AM/PM of the PA, regardless of the biasing voltage/harmonic termination. It can be shown that the effect of nonlinear C_M becomes more significant at high frequencies. The amount of AM/AM due to nonlinear input capacitance, both C_{GD} and C_M, can be reduced by compromising power gain and presenting a capacitive source impedance to the transistor, as shown in Figure 3.4.

3.4.2 Phase Nonlinearity − AM/PM

Phase nonlinearity (i.e., AM/PM) is a key metric measuring (to some extent) memory effects in PAs. The AM/PM of a PA strongly depends on its transistor technology and circuit design. For

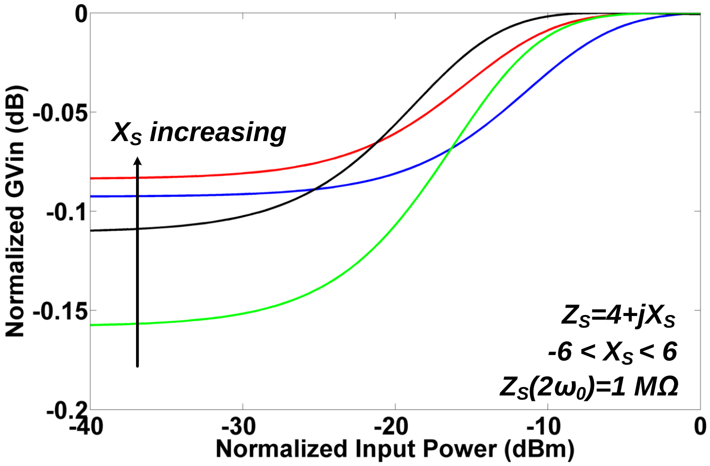

Figure 3.4: Simulated normalized G_{Vin} of the $45\,W$ GaN transistor versus input power and source termination.

example, GaN transistors have completely different sources of phase nonlinearity as compared to LDMOS transistors. The phase response of the PA is determined using (3.11) as,

$$PM_{out} = \angle G_{Vin} + \angle G_m + \angle Z_D(\omega_0). \tag{3.15}$$

We can categorize the major sources of phase nonlinearity in GaN transistors into nonlinear input capacitances and interaction with the knee region.

Nonlinear Input Capacitance

The nonlinear input capacitance distorts the phase of the intrinsic gate-source voltage before it goes to the drain of the transistor. In the case of a GaN transistor, a strongly nonlinear input capacitance can add significant AM/PM. The amount of AM/PM is a strong function of the biasing and source impedance of the GaN transistor. When the transistor is biased in linear class-A, the phase distortion becomes less significant as there is less variation in the input capacitance. However, when the transistor is biased in class-B (to achieve high efficiency), the phase distortion becomes pronounced and contributes significantly to AM/PM. It can be shown that the phase shift due to nonlinear input capacitance, with the nonlinearity profile given in (3.6), is calculated as (refer to appendix A):

$$\angle G_{Vin} \simeq \tan^{-1}\left(\frac{B_S}{G_S}\right) - \tan^{-1}\left(\frac{B_S + Y_{GS0} + 0.5\omega_0 C_{in2} V_S^2}{G_S}\right), \tag{3.16}$$

where $Y_S(\omega_0) = Z_S^{-1}(\omega_0) = G_S + jB_S$, V_S is the phasor of the source voltage and Y_{GS0} is defined as:

$$Y_{GS0} = \omega_0 \left(C_{in0} + C_{in1} V_{GS0} + C_{in2} V_{GS0}^2 \right). \tag{3.17}$$

The first term in (3.16) adds a constant phase (independent of input power) and hence does not contribute to AM/PM. The second term adds a power dependent phase shift which will contribute to AM/PM. The minimum amount of AM/PM is achieved when the $\angle G_{Vin}$ function is least sensitive to V_S variation (i.e., $min(S_{V_S}^{\angle G_{Vin}})$). The sensitivity of $\angle G_{Vin}$ to V_S is defined as:

$$S_{V_S}^{\angle G_{Vin}} = \left(\frac{V_S}{\angle G_{Vin}} \right) \cdot \left(\frac{d\left(\angle G_{Vin}\right)}{dV_S} \right). \tag{3.18}$$

Due to the nature of the $tan^{-1}(.)$ function, minimum sensitivity happens at:

$$min\left(S_{V_S}^{\angle G_{Vin}} \right) \Rightarrow \left(\frac{B_S + Y_{S0} + 0.5\omega_0 C_{in2} V_S^2}{G_S} \right) \rightarrow \pm\infty. \tag{3.19}$$

Hence, optimum input matching for minimum AM/PM requires maximizing $|B_S + Y_{S0}|$. Note that designing for maximum gain requires $B_S + Y_{S0} = 0$. This shows the fundamental trade-off between minimizing AM/PM and maximizing gain which can be seen using simulation results from the packaged $45\,W$ GaN transistor, shown in Figure 3.5. It is evident from Figure 3.5, that the amount of AM/PM induced by the nonlinear input capacitance is reduced as the source impedance becomes more capacitive. It should be noted that a more capacitive source impedance also reduces the sensitivity of AM/PM versus frequency. By appropriate choice of the source impedance, a compromise between gain and AM/PM sensitivity can be obtained.

Interaction with the Knee Region

The knee region intrusion is normally associated with gain compression and AM/AM nonlinearity at high input powers. However, knee region intrusion can also contribute to AM/PM distortions. As the drain voltage enters the knee region, the drain current becomes distorted. If the intrinsic drain is presented with ideal class-B impedances (i.e., short-circuit harmonics and resistive fundamental impedance), entering the knee region will only result in gain compression without phase distortion, as shown in Figure 3.6(a). However, if the harmonics are not short circuited and/or the fundamental impedance is not purely resistive, the drain current will distort asymmetrically, as shown in Figure 3.6(b), resulting in both AM/AM and AM/PM distortions. Note that the phase shifts due to non-zero harmonic terminations can be designed to be positive or

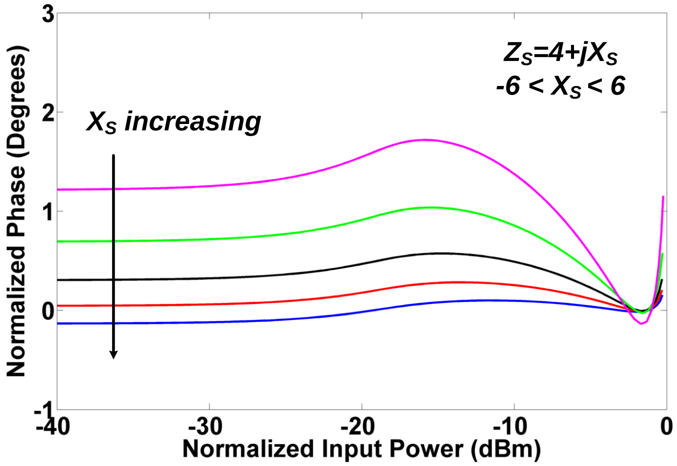

Figure 3.5: Simulated AM/PM of the 45 W GaN transistor versus input power and source termination.

negative, making it possible (to some extent) to cancel out the AM/PM caused by the input capacitance. Benefiting from high efficiency operation modes such as class-B/J where the efficiency is not very sensitive to second harmonic termination [100, 101], the overall phase distortion of the PA can be minimized by appropriate second harmonic termination without compromising efficiency.

3.4.3 Effect of Input Harmonic Termination on AM/AM and AM/PM

In GaN transistors, due to the nonlinear input capacitance, the efficiency and linearity are strongly dependent on the input impedance at fundamental and harmonics. The sensitivity of the efficiency of GaN PAs to the second harmonic termination at the input has been investigated extensively in the literature (e.g., [101]), however, its effect on linearity has not been discussed. It can be shown that in GaN PAs, improper second harmonic termination at the input can increase the amount of AM/PM; furthermore, it can result in a more pronounced soft compression. This was validated using simulation results from a 45 W GaN PA, shown in Figure 3.7. When the input second harmonic deviates from a short-circuit state, the second harmonic content of the gate voltage distorts the transconductance of the GaN transistor and results in stronger AM/AM and AM/PM nonlinearity. It should be noted that in the case of high power packaged transistors, it is impractical to short-circuit the second harmonic of the intrinsic gate so, as a result, added AM/AM and AM/PM nonlinearity is experienced due to improper input second harmonic

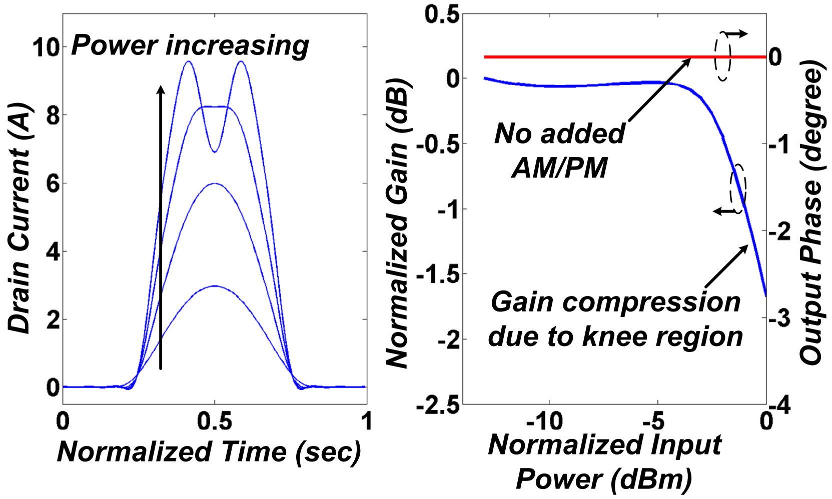

(a) Short-circuited harmonic termination

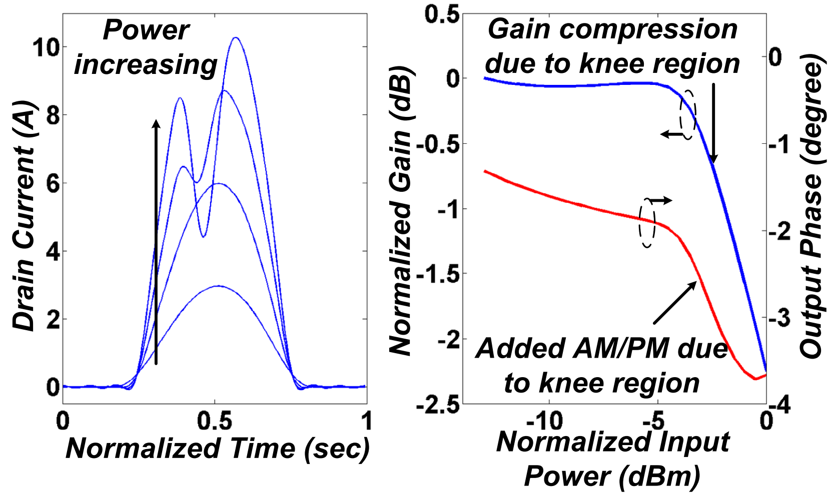

(b) Improper harmonic termination

Figure 3.6: Improper harmonic termination and knee region intrusion generates both AM/AM and AM/PM distortion.

termination.

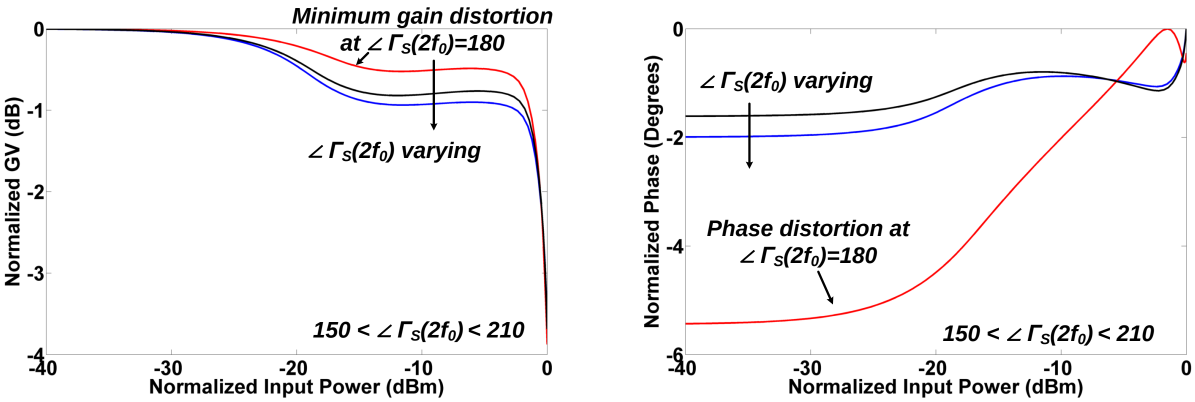

(a) AM/AM (b) AM/PM

Figure 3.7: The source second harmonic termination can affect both AM/AM and AM/PM significantly.

3.5 Sources of Memory Effects in Single-Band GaN PAs

The nonlinearity analysis presented in the previous section was limited to the case of a PA driven using a single sinusoid. When a nonlinear PA is driven with a modulated signal composed of hundreds of sinusoids with a time-varying envelope, the behavior of the PA can no longer be characterized using the static AM/AM and AM/PM responses. When driven with a modulated signal, the nonlinear PA will exhibit additional sources of dynamic nonlinearity, commonly referred to as memory effects. Memory effects in a nonlinear PA can be broadly categorized into long- and short-term memory effects. Note that long and short refer to the time-scale of the memory effects with respect to modulated signal bandwidth. The dominant physical sources of memory effects in GaN transistors are as follows:

- power/frequency dependent group delay,
- baseband impedance and unwanted drain modulation, and
- thermal and trapping effects.

In the following sections, we will discuss these sources in detail.

3.5.1 Power/Frequency Dependent Group Delay

The power/frequency dependent group delay results in short-term memory effects (i.e., in the order of the modulated signal bandwidth). The effect of power/frequency dependent group delay on the linearity of the PA is somewhat similar to the effect of frequency dependent group delay on the response of a linear time-invariant (LTI) circuit. The effect is visible in single-tone tests and can be characterized using AM/AM and AM/PM plots versus frequency within the bandwidth of the modulated signal. This source of memory effects can be minimized by maintaining a constant group delay (i.e., similar AM/AM and AM/PM shapes), versus frequency and input power. The intensity of the power/frequency dependent group delay becomes significant as the percentage modulation bandwidth exceeds $1-2\%$. For example, the power/frequency dependent group delay will become a significant contributor to the memory effects when amplifying a $40\,MHz$ modulated signal around the carrier frequency of $800\,MHz$ (5% instantaneous modulation bandwidth).

3.5.2 Baseband Impedance and Unwanted Drain Modulation

Unwanted drain modulation causes short-term memory effects (i.e., in the order of the envelope of the modulated signal). This effect is only visible in two- and multi-tone tests which makes it more challenging to study. Conventionally, this type of memory effect is studied using the third order inter-modulation distortion (IMD3) imbalance of the PA when excited using a two-tone signal. The unwanted drain modulation can cause memory effects through two distinct mechanisms.

The first mechanism, is the interaction of the nonlinear output capacitance with the output biasing feed (not a significant source in the case of GaN transistors). Assume the PA is driven with a two-tone sinusoidal signal at ω_1 and ω_2, as shown in Figure 3.8(a). As the result of nonlinear drain-source current, intermodulation products at $\Delta\omega = \omega_2 - \omega_1$ will be created. Note $\Delta\omega$ is in the order of the signal bandwidth and will be referred to as baseband frequency. Due to the non-zero impedance of the biasing feed at baseband frequency, the drain voltage of the transistor will be unintentionally modulated with the envelope signal. This will induce a nonlinear current in the output capacitance of the transistor which includes components at fundamental frequency, and cause memory effects and IMD3 imbalance (refer to Figure 3.8(a)). This phenomenon has been traditionally considered to be the dominant source of memory effects in LDMOS transistors.

The second mechanism, is the interaction of the nonlinear drain current with the output biasing feed (relevant to both GaN and LDMOS transistors). Again, in this case the drain is unintentionally modulated with the envelope signal due to the non-zero impedance of the biasing

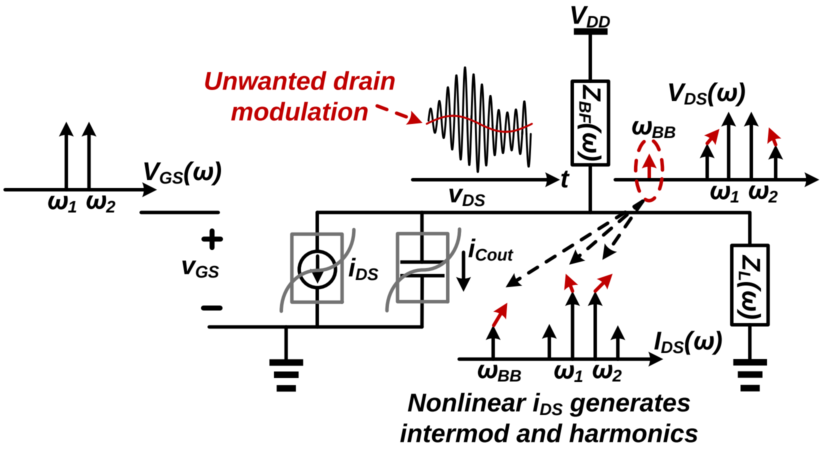

(a) Nonlinear output capacitance and biasing feed

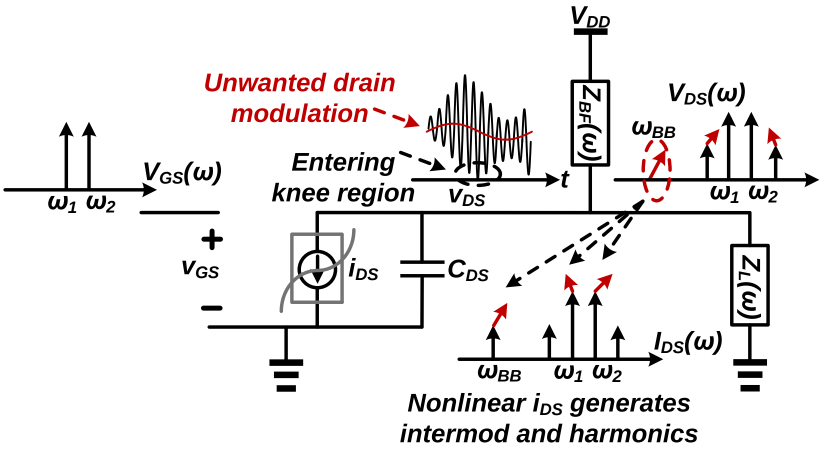

(b) Nonlinear drain current and biasing feed

Figure 3.8: (a) Memory effects due to nonlinear drain current and biasing feed, and (b) memory effects due to nonlinear output capacitance and biasing feed.

feed. Note that this drain modulation is not in-phase with the actual envelope signal due to the inductive nature of the biasing feed impedance (refer to Figure 3.8(b)). If the magnitude of the unwanted drain modulation is large enough, the transistor will enter the knee region which will introduce an added nonlinear current at the fundamental frequency resulting in memory effects and IMD3 imbalance. Both of these types of memory effects can be reduced by minimizing the impedance of the biasing feed at baseband frequency. In the case of LDMOS transistors, the existence of both sources offers the ability to selectively choose the biasing feed impedance so that the two effects work in opposite directions.

3.5.3 Thermal and Trapping Effects

Thermal memory effects happen when the temperature of the PA during operation is not constant which results in time-dependent gain and, consequently, dynamic nonlinearity [102]. Thermal memory effects become significant when the thermal time-constant of the PA and the signal variation speed become comparable. This effect can be minimized through appropriate thermal management. In OFDM-based modulation schemes, where the frame length of the signal can become comparable to the thermal time-constant (e.g., $10\,ms$ and longer), thermal memory effects become significant and difficult to linearize, especially as we move toward low power PAs. In this thesis, it is assumed that through appropriate thermal management and biasing schemes, thermal memory effects have become negligible.

Charge trappings due to the device non-idealities can similarly induce memory effects [102]. The capture and release of the carriers can change the gain of the amplifier versus time if the trapping time-constant is smaller than the signal variation speed. This phenomenon is a strong function of the transistor technology and is less problematic in devices made with a higher quality material fabrication process where trapping states are minimized. However, GaN transistors exhibit a significant amount of charge trapping. It can be shown that the effects of charge trapping will become more significant when the transistor is operated in ET mode. In this thesis, it is assumed that the time-constant of the charge trapping is much larger than the modulation bandwidth; thus, its effect will be negligible in terms of memory effects.

3.6 Validation with Simulation Results

In this section, the previously described sources of memory effects in GaN PAs have been validated through simulation of three generic GaN PAs. When simulating a generic PA (assuming we have access to relatively accurate circuit models), it is possible to decouple different sources of memory effects using appropriate/ideal matching networks and study the effect of each source separately. For example, using an ideal biasing feed in simulation, we are able to ensure that there will not be any unwanted drain modulation. The simulation results have been used as an initial validation of the memory effect study. The analysis was further validated using measurement results from a fabricated $45\,W$ GaN PA. Three $45\,W$ generic GaN PAs were simulated and driven with modulated signals using Agilent's ADS RF and Ptolemy co-simulations. All of the PAs were operated at $800\,MHz$ with simulated peak output power and drain efficiency of $46\,dBm$ and 75%, respectively. The three PAs were designed as follows:

- Case 1 – A harmonically tuned class-AB PA with an input matching network optimized for constant group delay, and optimum output biasing feed.
- Case 2 – A harmonically tuned class-AB PA with an input matching network not optimized for constant group delay, and optimum output biasing feed.
- Case 3 – A harmonically tuned class-AB PA with an input matching network optimized for constant group delay and a non-optimum output biasing feed.

The input and output matching networks for Case 1 and 3 were optimized to ensure the PA exhibited constant group delay versus power and frequency within the bandwidth of the modulated signal. This minimized the memory effects associated with the non-constant group delay. Note that group delay variation versus power and frequency for Case 2 is close to $2\,ns$. In Case 1 and 2, the output biasing feed was chosen to present a very low impedance at the intrinsic drain of the GaN transistor at baseband, reducing the memory effects associated with unwanted drain modulation. Figure 3.9 shows the static AM/AM and AM/PM for Case 1 and Case 3, and Figure 3.10 shows the static AM/AM and AM/PM for Case 2. Note the even though the output biasing feeds for Case 1 and 3 are different, the static AM/AM and AM/PM for the two cases are identical. As it can be seen in Figure 3.10, the PA in Case 2 exhibited group delay variation versus power/frequency, which resulted in memory effects.

In order to study the intensity of the memory effects in the three cases, all of the PAs were simulated using Agilent's ADS co-simulation driven with a $20\,MHz$ modulated signal. The PAs for Case 2 and 3 showed more spread in AM/AM and AM/PM, an indicator of strong memory effects. Figure 3.11 shows the simulated AM/AM of Case 1, 2, and 3. As can be seen in Figure 3.11, the significant unwanted drain modulation in Case 3 resulted in the transistor entering the knee region and more spread in AM/AM and AM/PM. To quantify the intensity of the memory effects, the PAs were linearized in simulation using a memoryless 7^{th} order polynomial DPD (using 8 complex coefficients). As the memoryless DPD corrected for the static nonlinearity, the residual nonlinearity represents the amount of memory effects in the PA. Figure 3.12 shows the spectrum of the three PAs with and without the memoryless DPD. The PA for Case 1 achieved an ACLR of more than $-52\,dBc$ when using the memoryless DPD, which is sufficient to meet the spectrum mask. The PAs for Case 2 and 3, however, only achieved an ACLR of $-43\,dBc$

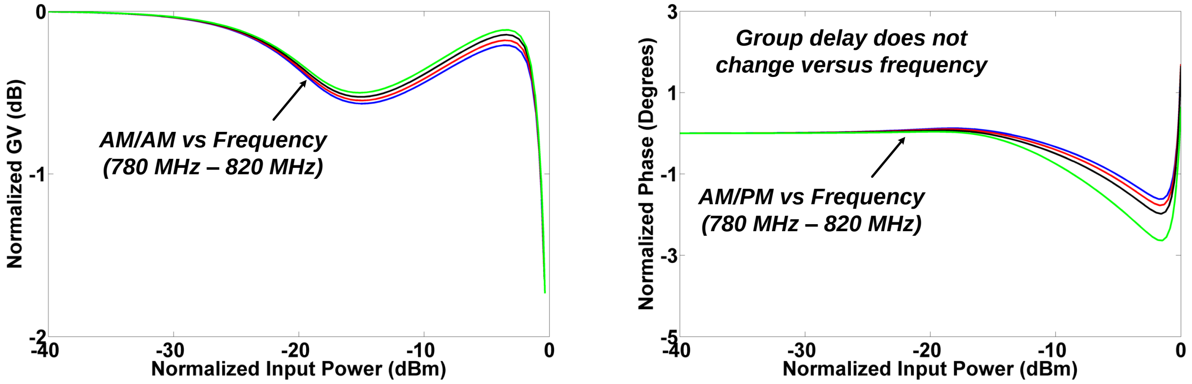

(a) AM/AM versus frequency

(b) AM/PM versus frequency

Figure 3.9: Simulated AM/AM and AM/PM of Case 1 and 3 versus frequency.

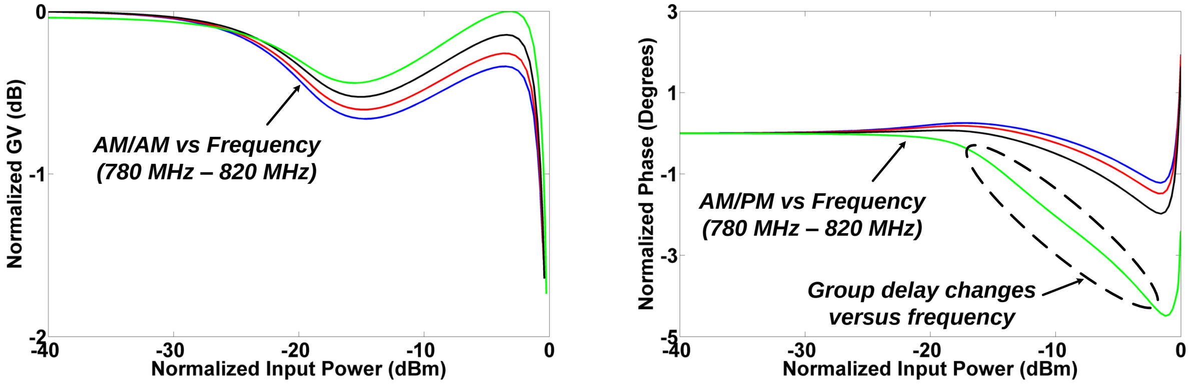

(a) AM/AM versus frequency

(b) AM/PM versus frequency

Figure 3.10: Simulated AM/AM and AM/PM of Case 2 versus frequency.

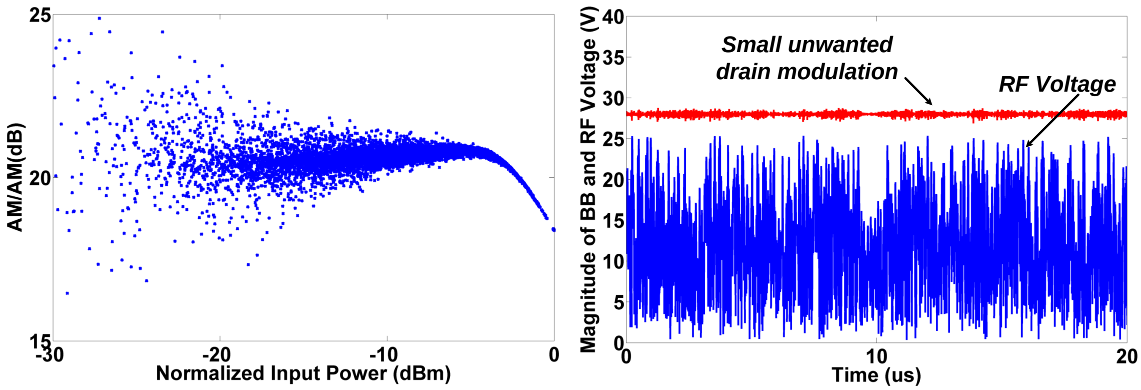

(a) Case 1 – Optimum biasing feed reduces the unwanted drain modulation

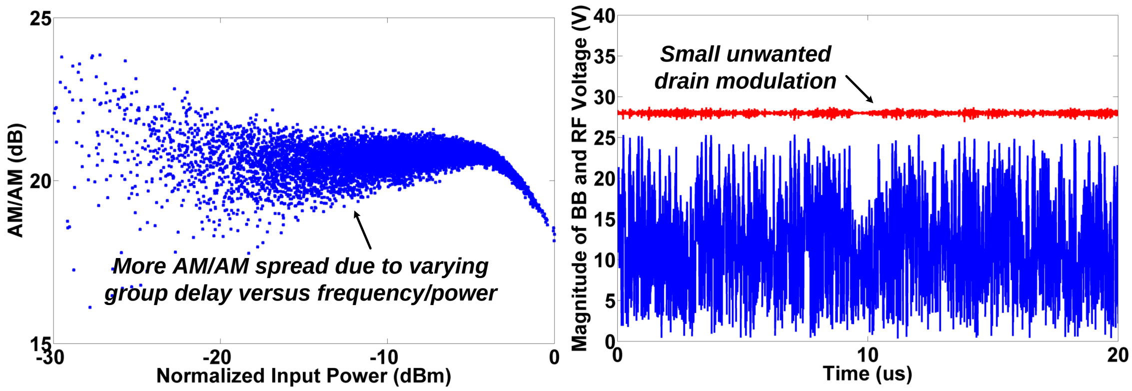

(b) Case 2 – More spread due to varying group delay versus power/frequency

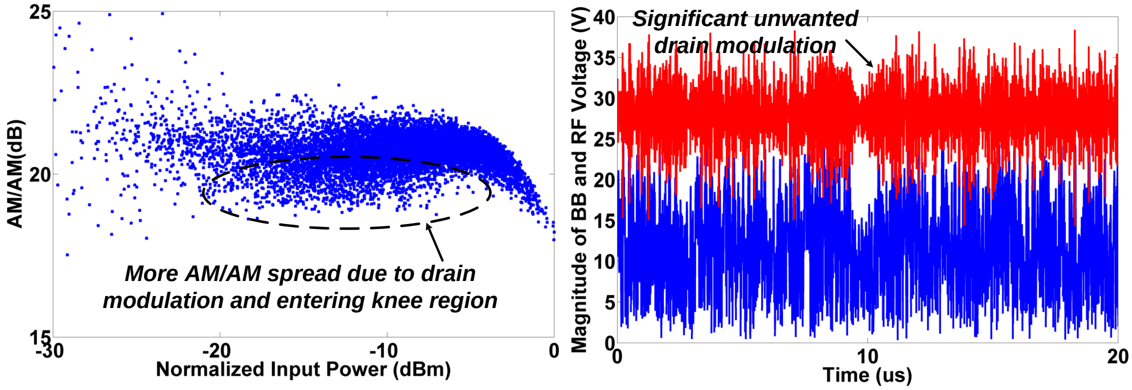

(c) Case 3 – More spread due to unwanted drain modulation

Figure 3.11: Simulated AM/AM of Case 1, 2 and 3 show more spread in case 2 and 3.

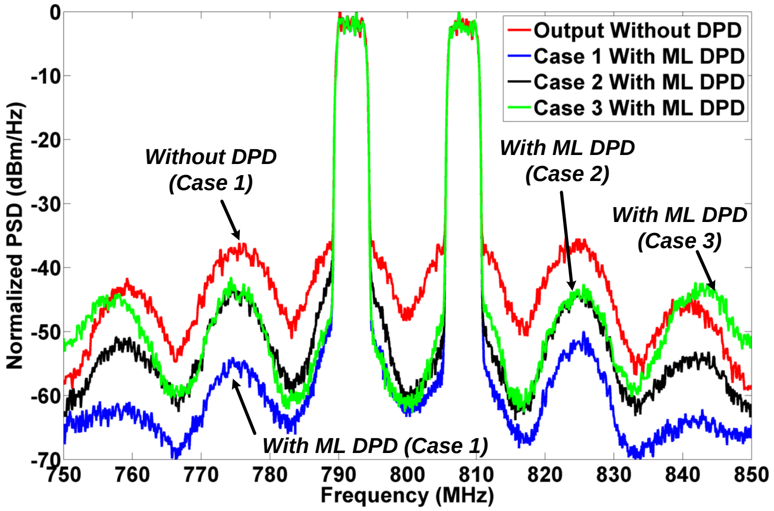

Figure 3.12: Simulated spectrum of Case 1, 2 and 3 with and without memoryless DPD.

Table 3.1: Summary of the simulation results for the three cases.

		Avg. Power (dBm)	**ACLR(dBc)**	**EVM (%)**	**DE (%)**
Case 1	No DPD	39	−32	3.8	32
	With DPD	38.9	−51	1.7	31.8
Case 2	No DPD	38.9	−31	4.2	32
	With DPD	39.1	−43	2.7	32.0
Case 3	No DPD	39.0	−30	4.5	32.1
	With DPD	39.0	−42	2.9	32.0

after the memoryless DPD was applied. The residual memory effects in Cases 2 and 3 can be linearized using appropriate memory DPD, such as memory polynomial (MP) or Volterra dynamic deviation reduction (DDR) DPD [103]. Note that DPD models with memory typically require a more complicated implementation, which increases the needed area and power dissipation of the DPD engine. Table 3.1 summarizes the simulation results for all the PAs before and after linearization.

3.7 Sources of Memory Effects in Dual-Band GaN PAs

When a nonlinear PA is driven with a dual-band modulated signal, the PA response includes additional sources of nonlinearity (both static and dynamic) compared to a single-band input. In the case of a dual-band signal at the center frequencies of ω_1 and ω_2, the PA's output spectrum will include high order intermodulation components at $\omega_1 - \omega_2$, $2\omega_1 - \omega_2$, $2\omega_2 - \omega_1$. Assuming the two carrier frequencies are spaced apart, the high order intermodulation products and harmonics can be filtered at the output of the PA using an appropriate dual-band filter. Note that depending on the filter's out-of-band rejection, there will be a requirement on the relative power level of the intermodulation products. However, the distortions around the carrier frequencies (ω_1 and ω_2) need to be linearized using dual-band DPD techniques.

The nonlinearity around carrier frequency ω_1 is the result of the input signal at ω_1, called self-distortion, and the input signal at ω_2, called cross-distortion. For example, when the input signal at ω_1 and ω_2 are at back-off and peak, respectively, the output signal at ω_1 shows mild self-distortion and strong cross-distortion nonlinearity. Note that both the self- and cross-distortions include static and dynamic nonlinearities. The static self- and cross-distortion nonlinearity is very similar to the static nonlinearity in single-band PAs, and can be modeled using static AM/AM and AM/PM responses for each band. The dynamic self- and cross-distortion nonlinearity, on the other hand, is more challenging to study. In this section we briefly review the sources of dynamic self- and cross-distortion nonlinearities in dual-band GaN PAs.

3.7.1 Self-Distortion Memory Effects

The sources of self-distortion memory effects are very similar to the sources of memory effects in single-band PAs. For GaN PAs, the sources of self-distortion memory effects are determined as:

- power/frequency dependent group delay around ω_1 and ω_2, and
- unwanted drain modulation at baseband frequency.

The self-distortion memory effects in dual-band GaN PAs can be reduced in a similar manner to that used for single-band PAs; optimizing the input and output matching networks to maintain constant group delay versus power/frequency, and optimizing the output biasing feed to reduce the unwanted drain modulation. It is important to note that if the group delays at ω_1 and ω_2 are different (i.e., $\tau_{\omega_1} \neq \tau_{\omega_2}$), it will not result in self-distortion memory effects as long as τ_{ω_1} and τ_{ω_2} do not change versus power or within the bandwidth of the modulated signals.

3.7.2 Cross-Distortion Memory Effects

The sources of cross-distortion memory effects can be categorized into two major groups. The first source of cross-distortion memory effects is the self-distortion memory effect in one of the bands. If the signal at ω_1 shows strong self-distortion memory effects (e.g., if the transistor enters the knee region as the result of unwanted drain modulation at baseband), the signal at ω_2 will also exhibit cross-distortion memory effects.

The second source of cross-distortion memory effects, which is more difficult to control, is the unwanted drain modulation at $\omega_1 - \omega_2$. The nonlinear drain-source current of the transistor will generate intermodulation products at baseband frequency (in the order of the modulation bandwidth of the individual signals), as well as intermodulation products at $\omega_1 - \omega_2$. Depending on the spacing between the two bands, this component can be up to a few hundred megahertz, whereas the baseband component is typically only in the order of $20MHz - 40MHz$. Due to the non-zero impedance of the biasing feed and the matching network at $\omega_1 - \omega_2$, the drain voltage of the transistor will be unintentionally modulated at $\omega_1 - \omega_2$. Similar to baseband unwanted drain modulation, this nonlinear current can cause the transistor to enter the knee region which will result in cross-distortion memory effects.

The cross-distortion memory effects in dual-band GaN PAs can be minimized by, (i) ensuring both bands have insignificant self-distortion memory effects and, (ii) presenting a low impedance at the drain of the transistor at $\omega_1 - \omega_2$. In practice, it is difficult to ensure this impedance is low for all carrier spacings. However, using more complicated biasing networks employing multiple low-quality factor resonators can reduce the impedance at $\omega_1 - \omega_2$ significantly, and consequently reduce the memory effects in dual-band ET PAs.

3.8 Design to Mitigate Memory Effects in Single-Band and Dual-Band GaN PAs

Using the analysis on sources of memory effects, a design approach is devised to mitigate the sources of memory effects in dual-band GaN PAs from the circuit design stage. The design approach can be summarize as follows:

- design the output matching network for peak output power and efficiency using the results from load-pull and class-B/J design space,
- design the input matching matching network to desensitize AM/PM to frequency and

power, while maintaining constant group delay versus power and frequency within the desired modulation bandwidth, and

- design the output biasing feed to ensure the baseband impedance seen at the drain is minimized.

Both the input and the output matching networks can be implemented using simplified real frequency technique (SRFT) using lumped components or stepped microstrip transmission lines [101]. It should be noted that in the case of dual-band PAs, the baseband impedance seen at the drain must be minimized at the separation frequency of the two carriers. For separation frequencies up to few hundreds of megahertz, this can be achieved using conventional inductive biasing feed. However, for wider separation frequencies, more sophisticated biasing feeds need to be employed.

Using the proposed design approach, a single-stage $45\,W$ GaN PA was designed to mitigate sources of memory effect from the circuit design stage. The aim of mitigating the memory effects was to design a PA which could be linearized using either a memoryless DPD or a simple memory DPD. This would reduce the complexity and power dissipation for the DPD platform where a simple DPD technique would be sufficient to linearize the PA. The design was done using a $45\,W$ packaged GaN transistor (Cree CGH40045F), targeting $0.7\,GHz - 1.0\,GHz$. The transistor was biased at $400\,mA$ (corresponding to a conduction angle of 200^o) from a constant $28\,V$ drain supply voltage. The schematic of the fabricated GaN PA is shown in Figure 3.13 and 3.14. The input and output matching networks were optimized to ensure constant group delay versus power/frequency. The output biasing feed was implemented through a thick transmission line in order to reduce the baseband impedance presented at the drain of the transistor.

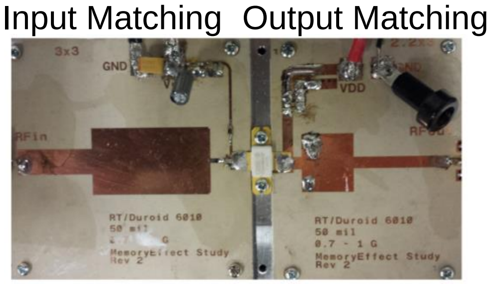

Figure 3.13: Photograph of the fabricated $45\,W$ GaN PA.

Figure 3.15 shows the simulated AM/AM and AM/PM of the GaN PA from $750\,MHz$ to $850\,MHz$. In order to ensure memory effects of the GaN PA were reduced for single- and

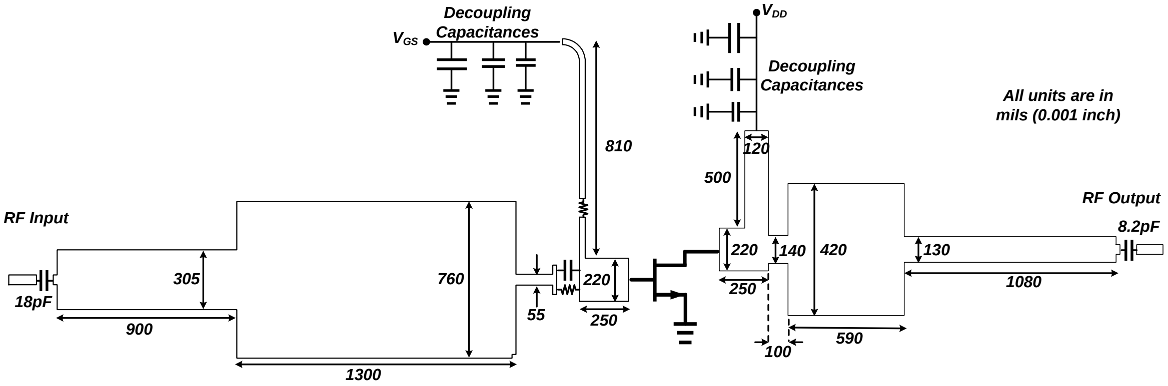

Figure 3.14: Schematic of the fabricated 45 W GaN PA.

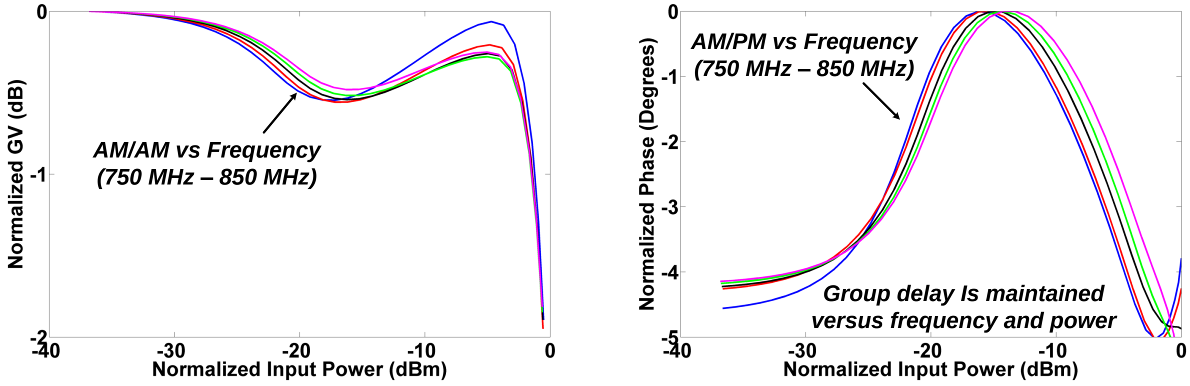

(a) AM/AM versus frequency

(b) AM/PM versus frequency

Figure 3.15: Simulated AM/AM and AM/PM of the GaN PA versus frequency.

dual-band excitations, the baseband impedance at the drain of the transistor was reduced up to 200 MHz, as shown in Figure 3.16. The measured continuous wave (CW) output power, gain and drain efficiency of the PA is shown Figure 3.17. The PA was linearized using a 7^{th} order memoryless DPD (8 complex coefficients) when driven with single-band 20 MHz and 40 MHz modulated signals. In all cases, the dynamic range of the coefficients was less than 62 dB (less than 10 bits resolution). Note that the dynamic range of the coefficients was defined as:

$$DR_{coef} = 20\log_{10}\left(\frac{\max(|a_i|)}{\min(|a_i|)}\right), \tag{3.20}$$

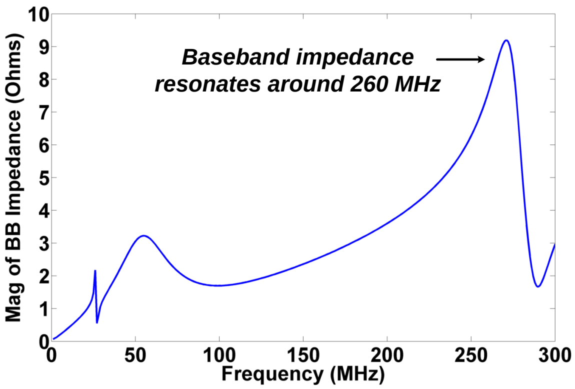

Figure 3.16: Simulated baseband impedance of the GaN PA.

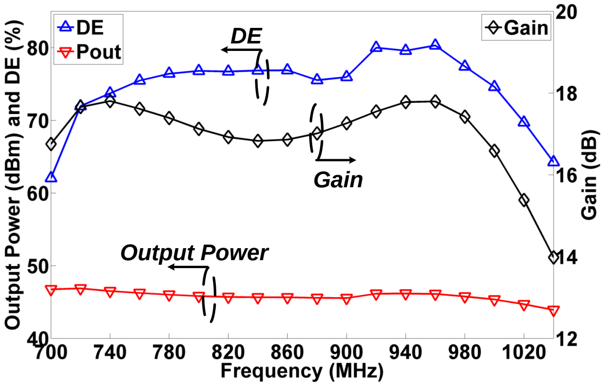

Figure 3.17: Measured output power, efficiency and gain of the GaN PA.

where a_i were the complex coefficients of the memoryless DPD. Figure 3.18 and 3.19 show the measured spectrum of the GaN PA with and without memoryless linearization, driven with $20\,MHz$ and $40\,MHz$ modulated signals, for various carrier frequencies. In all cases, the GaN PA achieved an ACLR of more than $-47\,dBc$ using the memoryless DPD. The residual nonlinearity due to memory effects was linearized using MP DPD with a nonlinearity order of 7 and memory depth of 2 (with a total of 16 complex coefficients).

The GaN PA was further validated when driven with dual-band 4C WCDMA and LTE $20\,MHz$ modulated signals at $750\,MHz$ and $850\,MHz$ with an average output power and efficiency of $35.5\,dBm$ and 24%, respectively. The GaN PA achieved an ACLR of better than $-47\,dBc$ when linearized using a 7^{th} order memoryless two-dimensional DPD (2D-DPD) [104] with a total of 28 complex coefficients per band. The dynamic range of the coefficients in that

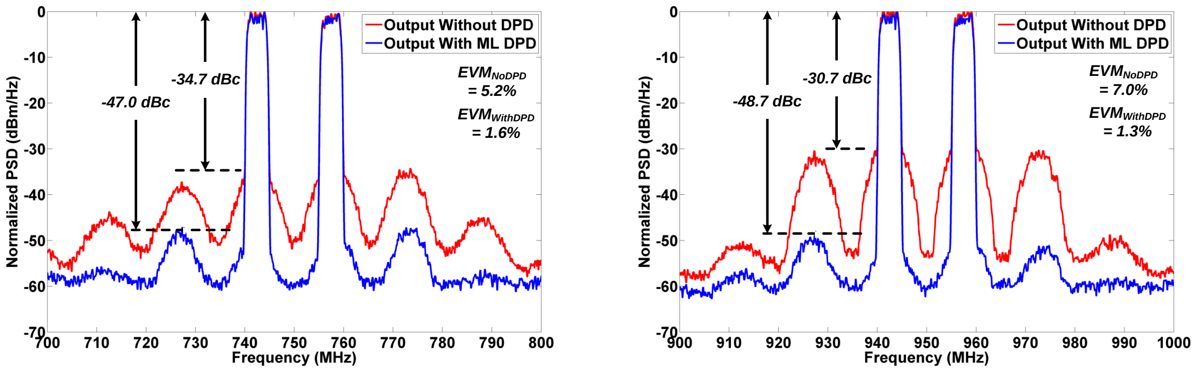

(a) 4C WCDMA at 750 MHz (b) 4C WCDMA at 950 MHz

Figure 3.18: Measured spectrum of the GaN PA when driven with a 4C WCDMA with and without memoryless DPD at 750 MHz and 950 MHz.

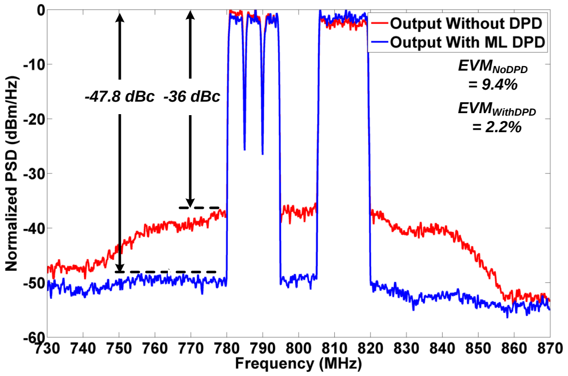

Figure 3.19: Measured spectrum of the GaN PA when driven with a 40 MHz signal with and without memoryless DPD at 800 MHz.

case was less than 55 dB, ensuring easy implementation in practice.

3.9 Conclusion

This chapter presented a detailed study and analysis of the sources of nonlinearity in single- and dual-band GaN PAs. This analysis can provide PA designers with guidelines to reduce the sources of memory effects in GaN PAs from the circuit design stage. By reducing the sources of

Table 3.2: Summary of the single-band measurement results of the 45 W GaN PA using 7^{th} memoryless polynomial DPD.

Freq (GHz)		**Mod. BW (MHz)**	**Power (dBm)**	**Avg Eff. (%)**	**ACLR (dBc)**	**EVM (%)**	**PAPR (dB)**	**# of Coeff.**	**DR of Coeff.**
0.75	No DPD	20	38.8	33%	−34.7	5.2	7.1	–	–
	With DPD	20	38.9	33%	−47	1.6	7.1	8	55
0.80	No DPD	20	38.7	36%	−32.3	6.4	7.1	–	–
	With DPD	20	38.6	36%	−47.8	1.4	7.10	8	60
0.85	No DPD	20	38.7	36%	−34.7	4.1	6.5	–	–
	With DPD	20	38.6	36%	−47.9	1.8	7.17	8	51
0.90	No DPD	20	38.5	34%	−33.8	4.8	6.16	–	–
	With DPD	20	38.5	34%	−48.2	1.8	7.10	8	58
0.95	No DPD	20	38.7	33%	−30.7	7.0	6.01	–	–
	With DPD	20	38.6	33%	−48.7	1.3	7.16	8	56
0.80	No DPD	40	37.8	29%	−36.0	9.4	7.6	–	–
	With DPD	40	37.6	29%	−47.8	2.2	7.16	8	60

memory effects in single- and dual-band PAs, one can ensure that relatively simple linearization techniques, such as LUT or memoryless polynomial DPD, are sufficient to linearize them. This will result in lower power dissipation and complexity for the DPD engine. This will become essential as we move toward smaller base station cell sizes, such as pico- and femto-cells. Using the analysis presented in this chapter, a 45 W GaN PA with reduced sources of memory effects was designed and measured. The GaN PA was linearized using 7^{th} order memoryless polynomial DPD when amplifying wideband modulated signals up to 40 MHz. Furthermore, the GaN PA was linearized using memorlyess 2D-DPD when amplifying two 20 MHz dual-band modulated signals.

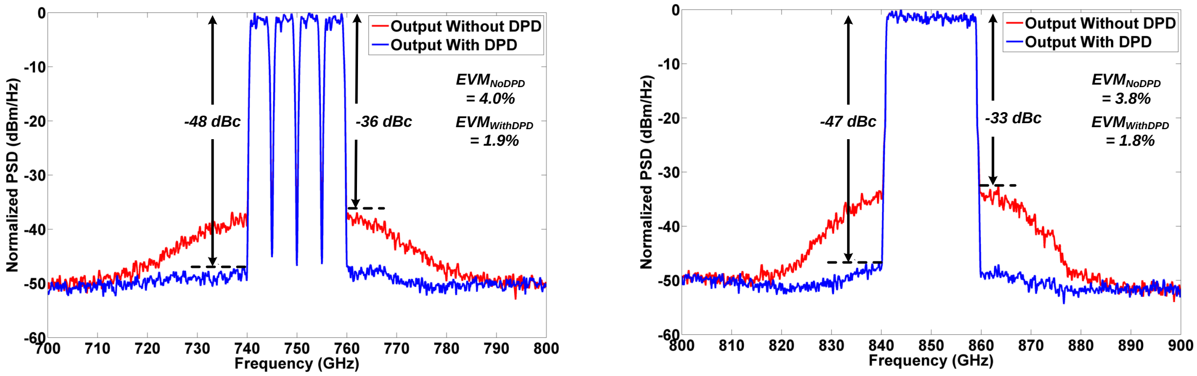

(a) Band 1 – 4C WCDMA

(b) Band 2 – LTE 20 MHz

Figure 3.20: Measured spectrum of the GaN PA when driven with a dual-band 4C WCDMA and LTE 20 MHz signals with and without memoryless 2D-DPD.

Chapter 4

Concurrent Dual-Band ET PA

4.1 Introduction

As stated in Chapter 2, concurrent dual-band transmission using ET PAs has not been shown in the literature, mainly due to the limited speed of the envelope amplifier used to modulate the drain supply of the PA (refer to Figure 4.1, redrawn from Chapter 2). A few recent publications (e.g., [52–55]), have made attempts to design ET PAs for concurrent amplification of dual-band signals. However, these publications did not show modulated signal tests and lacked detailed efficiency and linearity analyses. This chapter proposes an ET PA capable of concurrent dual-band operation. Furthermore, the effect of the proposed solution on the overall efficiency and linearity of the dual-band ET PA are analyzed in detail. The effectiveness of the proposed dual-band ET PA is also validated using the measurement results from two ET PA prototypes.

4.2 Concurrent Dual-Band ET Operation

4.2.1 Basic Principle

This section aims at formulating the problem of concurrent transmission of dual-band modulated signals using a single ET PA, starting with calculating the envelope of a concurrent dual-band signal. This analysis assumes the dual-band signal is composed of the individual signals expressed

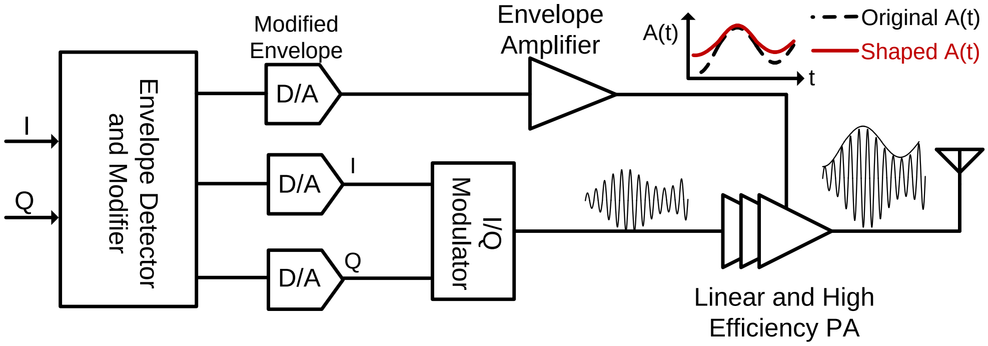

Figure 4.1: Simplified schematic of an ET PA.

as follows:

$$\begin{aligned} v_1(t) &= I_1(t)\cos(\omega_{c1}t) + Q_1(t)\sin(\omega_{c1}t), \\ v_2(t) &= I_2(t)\cos(\omega_{c2}t + \theta_0) + Q_2(t)\sin(\omega_{c2}t + \theta_0), \end{aligned} \tag{4.1}$$

where ω_{c1} and ω_{c2} denote the two carrier frequencies, $I_1(t)$, $I_2(t)$, $Q_1(t)$ and $Q_2(t)$ represent the in-phase and quadrature components of the signals in bands 1 and 2, respectively, and θ_0 designates the phase shift between the two carrier frequencies. Combining the two modulated signals yields the concurrent dual-band signal which is expressed as:

$$\begin{aligned} v_{DB}(t) &= v_1(t) + v_2(t) \\ &= (I_1(t)\cos(\omega_{c1}t) + Q_1(t)\sin(\omega_{c1}t)) \\ &\quad + (I_2(t)\cos((\Delta\omega + \omega_{c1})t + \theta_0) + Q_2(t)\sin((\Delta\omega + \omega_{c1}) + \theta_0)) . \end{aligned} \tag{4.2}$$

where $\Delta\omega = (\omega_{c2} - \omega_{c1})$ denotes the frequency spacing. Rewriting (4.2) results in,

$$v_{DB}(t) = \hat{I}(t)\cos(\omega_{c1}t) + \hat{Q}(t)\sin(\omega_{c1}t), \tag{4.3}$$

where,

$$\hat{I}(t) = I_1(t) + I_2(t)\cos(\Delta\omega t + \theta_0) + Q_2(t)\sin(\Delta\omega t + \theta_0), \tag{4.4}$$

$$\hat{Q}(t) = Q_1(t) + Q_2(t)\cos(\Delta\omega t + \theta_0) - I_2(t)\sin(\Delta\omega t + \theta_0). \tag{4.5}$$

Using (4.3), the envelope of the dual-band signal is expressed as,

$$\begin{aligned} a_{DB}^2(t) &= \hat{I}^2(t) + \hat{Q}^2(t), \\ &= I_1^2(t) + I_2^2(t) + Q_1^2(t) + Q_2^2(t) \\ &+ 2(I_1(t)I_2(t) - Q_1(t)Q_2(t))\cos(\Delta\omega t + \theta_0) \\ &+ 2(Q_1(t)I_2(t) + I_1(t)Q_2(t))\sin(\Delta\omega t + \theta_0). \end{aligned} \tag{4.6}$$

According to (4.6), the envelope of the dual-band signal is composed of two components: (i) a low frequency component (LFC) that depends exclusively on $I_1(t)$, $I_2(t)$, $Q_1(t)$ and $Q_2(t)$, and (ii) a high frequency component that involves frequency spacing, $\Delta\omega$.

The envelope of the dual-band signal in (4.6) cannot be used in its original form to drive a typical envelope amplifier. The envelope requires a high speed (and consequently power inefficient) envelope amplifier as the frequency spacing can be in the order of hundreds of megahertz. The LFC of the envelope of the dual-band signal is calculated as the envelope of $a_{DB}(t)$ (i.e., the envelope of the envelope of the dual-band signal), so,

$$a_{LF}(t) = \left(\sqrt{I_1^2(t) + Q_1^2(t)} + \sqrt{I_2^2(t) + Q_2^2(t)}\right). \tag{4.7}$$

According to (4.7), the bandwidth of the $a_{LF}(t)$ is equal to the largest bandwidth of the individual envelope signals, in other words,

$$BW\left(a_{LF}(t)\right) = max\{BW\left(a_1(t)\right), BW\left(a_2(t)\right)\}, \tag{4.8}$$

where,

$$a_1(t) = \sqrt{I_1^2(t) + Q_1^2(t)};\;\; a_2(t) = \sqrt{I_2^2(t) + Q_2^2(t)}. \tag{4.9}$$

Hence, if a_{LF} is used to control the envelope amplifier in a dual-band ET PA, it will require similar envelope amplifier bandwidth to the single-band ET PA, thus eliminating the challenges attributed to the frequency spacing.

Figure 4.2 shows the envelope of the dual-band signal given in (4.6) and its LFC, a_{LF}, given in (4.7), when the carrier frequencies are at $2.05\,GHz$ and $2.15\,GHz$ and are modulated according to downlink LTE $5\,MHz$ and single-carrier WCDMA, respectively. The individual single-band signals have a PAPR of $9.5\,dB$ and $9.1\,dB$, respectively, and the combined dual-band signal has a PAPR of $8.2\,dB$.

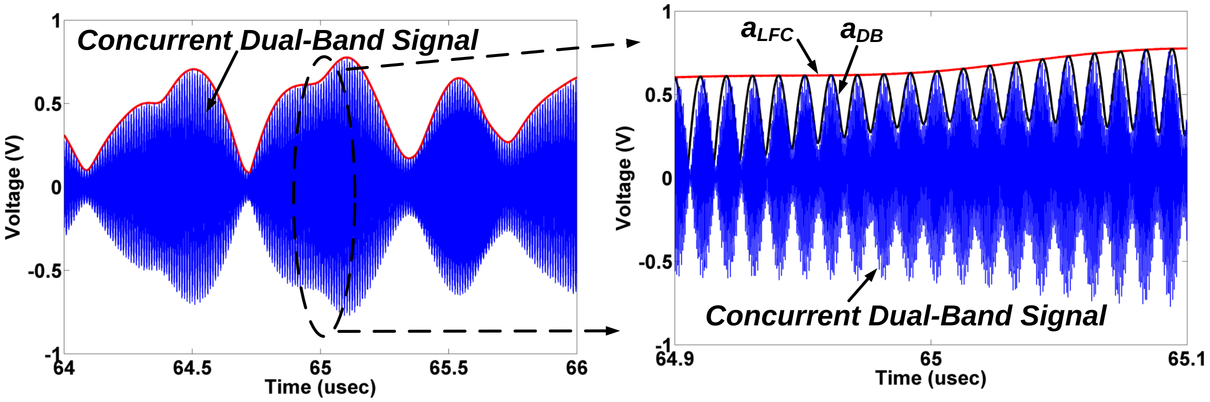

(a) Time domain envelope of the dual-band signal.

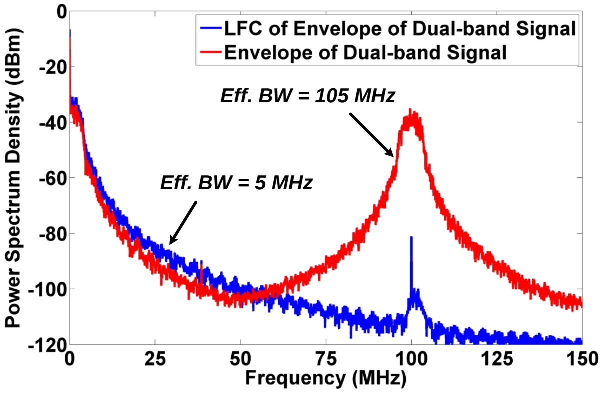

(b) Frequency domain envelope of the dual-band signal.

Figure 4.2: (a) Time domain and (b) frequency domain envelope of the dual-band signal and its LFC for a concurrent dual-band LTE and WCDMA signal.

4.2.2 Efficiency Analysis

Using the LFC of the envelope of the dual-band signal, $a_{LF}(t)$, to modulate the drain supply voltage of the PA rather than using the complete envelope of the dual-band signal, $a_{DB}(t)$, addresses one of the main obstacles in developing ET PAs for concurrent dual-band transmission. According to Figure 4.2, the LFC of the envelope of the dual-band signal does not follow its instantaneous envelope. This results in a drain supply voltage that does not always correspond to the instantaneous RF signal at the input of the PA. In other words, the employment of $a_{LF}(t)$ results in a drain supply voltage that can be higher than necessary for a given input signal power, as observed in Figure 4.2(a) where the value of $a_{LF}(t)$ is higher than $a_{DB}(t)$ at times. This leads to a contraction in the efficiency enhancement of the ET operation. The efficiency contraction attributed to the simplification of the envelope of the dual-band signal is discussed in the next paragraph.

In the case of an ET system with an ideal class-AB biased PA, the general form of the drain efficiency at a given normalized input signal envelope, $a_{DB}(t)$, and output power, $P_{out}(t)$, excluding losses in the envelope amplifier, is calculated as:

$$\eta(P_{out}) = \frac{P_{out}(t)}{P_{DC}} = \frac{P_{out}(t)}{V_{DD}(P_{out})I_{DD}(P_{out})}, \tag{4.10}$$

where $V_{DD}(P_{out}) = V_{DD,max} \times a(t)$ and $P_{out}(t) \propto a^2_{DB}(t)$. Applying (4.10) to the following two cases of a dual-band ET:

- Case I – drain voltage modulated using the complete dual-band signal envelope, a_{DB}, and
- Case II – drain voltage modulated using the LFC of the dual-band envelope, a_{LF},

results in,

$$\eta_{DB}(P_{out}) = \frac{1}{a_{DB}(t)} . \frac{ka^2_{DB}(t)}{V_{DD,max}I_{DD}(P_{out})}, \tag{4.11}$$

$$\eta_{LF}(P_{out}) = \frac{1}{a_{LF}(t)} . \frac{ka^2_{DB}(t)}{V_{DD,max}I_{DD}(P_{out})} = \eta_{DB}(P_{out}) . \frac{a_{DB}(t)}{a_{LF}(t)}, \tag{4.12}$$

where η_{DB} and η_{LF} are the efficiency of the ET PA for Case I and II, respectively. When the dual-band ET PA is driven with a modulated signal with a given power density function (PDF), the average efficiencies obtained for the above two cases are calculated as:

$$\eta_{avg,DB} = \frac{\displaystyle\int_0^1 ka^2_{DB}.PDF_{DB}(a_{DB})da_{DB}}{\displaystyle\int_0^1 \frac{ka^2_{DB}}{\eta_{DB}(ka^2_{DB})}.PDF_{DB}(a_{DB})da_{DB}}, \tag{4.13}$$

$$\eta_{avg,LF} = \frac{\displaystyle\int_0^1 ka^2_{DB}.PDF_{DB}(a_{DB})da_{DB}}{\displaystyle\int_0^1\int_0^1 \frac{ka_{LF}a_{DB}}{\eta_{DB}(ka^2_{DB})}.PDF_{LF}(a_{DB},a_{LF})da_{LF}da_{DB}}, \tag{4.14}$$

where $\eta_{avg,DB}$ and $\eta_{avg,LF}$ denote the average efficiency of the concurrent dual-band ET PA using the complete envelope of the dual-band signal and its LFC, respectively. $PDF_{DB}(.)$ and $PDF_{LF}(.)$

represent the PDF of the complete envelope of the dual-band signal and its LFC, respectively. One can define γ_{CF} as the efficiency contraction factor attributed to the envelope simplification as:

$$\gamma_{CF}=\frac{\eta_{avg,LF}}{\eta_{avg,DB}}=\frac{\displaystyle\int_0^1\int_0^1 a_{LF}\frac{ka_{DB}}{\eta_{DB}(ka_{DB}^2)}.PDF_{LF}(a_{DB},a_{LF})da_{LF}da_{DB}}{\displaystyle\int_0^1\frac{ka_{DB}^2}{\eta_{DB}(ka_{DB}^2)}.PDF_{DB}(a_{DB})da_{DB}}. \tag{4.15}$$

According to (4.15), the efficiency contraction factor is independent of frequency spacing (i.e., $\Delta\omega$), and is a function of the individual signal characteristics (e.g., PDF and PAPR), and the efficiency profile of the PA. In the case of an ideal class-B biased PA, equation (4.15) can be simplified as:

$$\gamma_{CF}=\frac{\displaystyle\int_0^1 a_{LF}.PDF_{LF}(a_{DB})da_{DB}}{\displaystyle\int_0^1 a_{DB}.PDF_{LF}(a_{DB})da_{DB}}. \tag{4.16}$$

The application of (4.16) to the previously mentioned dual-band signal (formed by downlink LTE $5\,MHz$ and single-carrier WCDMA signals) results in an efficiency contraction factor of 80% when the PA is biased in class-B. When the PA is biased in class-AB with a conduction angle of 200^o (where GaN PAs are typically biased in practice), the efficiency contraction factor increases to 94%. The significant increase in the efficiency contraction factor is due to the efficiency characteristics of the PA versus supply voltage and input power. The effect of the conduction angle of the PA on the efficiency contraction factor can be better understood with the use of an example.

Assume we have an ideal class-B PA with 78.5% peak drain efficiency. Using the original concurrent dual-band envelope signal, $a_{DB}(t)$ to modulate the drain supply voltage, the PA will maintain its peak efficiency at power back-off resulting in $\eta_{avg,DB}=78.5\%$, regardless of the signal characteristics. If we modulate the drain supply voltage using $a_{LF}(t)$, the average efficiency of the PA will be reduced by the efficiency contraction factor as,

$$\eta_{avg,LF}=\eta_{avg,DB}.\gamma_{CF}=78.5\times 0.80=62.8\%. \tag{4.17}$$

Note that the loss of 16% would be significant, especially as this does not include the losses in the envelope amplifier. However, in practice, due to linearity considerations, the transistor is biased in class-AB. Assume we have a class-AB PA with a conduction angle of 200^o (where GaN PAs are typically biased in practice), with a peak drain efficiency of 70%. Using the efficiency profile of the class-AB PA, the efficiency of the PA when the supply voltage is modulated using

$a_{DB}(t)$ is calculated as, $\eta_{avg,DB} = 64.5\%$. If we modulate the drain supply voltage using $a_{LF}(t)$, the average efficiency of the class-AB PA will be reduced by the efficiency contraction factor as,

$$\eta_{avg,LF} = \eta_{avg,DB} \cdot \gamma_{CF} = 64.5 \times 0.94 = 60.6\%, \tag{4.18}$$

resulting in an efficiency loss of only 4%. Using this efficiency analysis, it can be concluded that the amount of efficiency contraction due to the application of $a_{LF}(t)$ in a class-AB PA is not significant. This proves that implementing a concurrent dual-band ET PA using the LFC of the envelope of the dual-band signal, $a_{LF}(t)$, is beneficial in terms of efficiency enhancement. We discuss and validate this efficiency analysis further, as applied to a $10\,W$ GaN class-J PA, in Section 4.2.4.

4.2.3 Linearity Analysis

In the ideal case, where the PA nonlinearity is independent of the drain supply voltage, the proposed envelope simplification will not introduce any additional distortions to the dual-band ET PA. However, in practice, as the PA behavior changes with the drain supply voltage, the dual-band ET PA may exhibit higher nonlinearity. This can be illustrated with the aid of Figure 4.3. Suppose the PA is driven with a concurrent dual-band signal while the drain supply voltage is modulated according to a_{LF}, as shown in Figure 4.3. When the dual-band ET PA is driven with the same input power at both points ”A” and ”B” (refer to Figure 4.3), the PA drain bias voltage will correspond to $a_{LF,A}$ and $a_{LF,B}$. This will result in different C_{ds} and r_{ds} for the transistor. In this example, the PA is operating closer to the knee region at point ”A” compared to point ”B”; hence the ET PA will exhibit stronger nonlinearity (i.e., more gain compression and added phase distortion).

The intensification of the distortion is strongly dependent on the transistor technology and the nonlinearity profile of the transistor’s parasitics (i.e., C_{ds} and r_{ds}). Strong nonlinearity in r_{ds} will correspond to significant amplitude distortion at point ”A” as compared to point ”B”. This will translate into more spread and more memory in the amplitude response of the dual-band ET PA (i.e., more spread in AM/AM). For example, a transistor that exhibits a gradual knee region will have strong r_{ds} nonlinearity. Strong nonlinearity in C_{ds} will correspond to significant phase distortion at point ”A” comparied to point ”B”. This will translate into more spread in the AM/PM response of the dual-band ET PA. It should be noted that greater spread in the AM/AM and AM/PM responses of the dual-band ET PA will complicate the linearization of the PA. In the case of GaN transistors, the output capacitance (C_{ds}) is fairly linear; hence the spread in AM/PM is minimal. The r_{ds} nonlinearity in GaN transistor is moderate; thus, we expect more spread in the AM/AM of the dual-band ET PA using a_{LF}. This linearity analysis was validated using co-simulation of a $10\,W$ GaN class-J PA in Section 4.2.4. It is important to note that in the case of

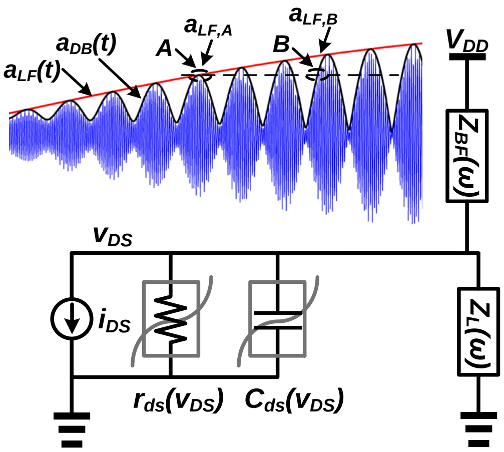

Figure 4.3: Effect of supply modulation on the linearity of the dual-band ET PA.

LDMOS transistors, we expect significant amount of phase and amplitude distortion to be added for a dual-band ET PA as the LDMOS transistor has a strongly nonlinear output capacitance (i.e., C_{ds}).

4.2.4 Validation in Simulation

In order to validate the effect of dual-band ET operation using $a_{LF}(t)$ on linearity and efficiency, a $10\,W$ GaN class-J PA (conduction angle of 200^o) was simulated using Agilent's ADS RF and Ptolemy co-simulations. The $10\,W$ GaN class-J PA was operated at $1.95-2.25\,GHz$ with peak output power and drain efficiency of $40\,dBm$ and 75%, respectively, when biased at $28\,V$. Figure 4.4 shows the measured continuous wave (CW) power added efficiency (PAE) of the PA versus output power and frequency when the drain supply voltage was varied from $8-28\,V$.

The $10\,W$ GaN PA was simulated as being driven with the previously mentioned dual-band LTE $5\,MHz$ ($9.6\,dB$ PAPR) and WCDMA ($9.1\,dB$ PAPR) signals at $2.05\,GHz$ and $2.15\,GHz$, respectively, for three cases:

- Case I – $10\,W$ GaN dual-band PA with constant supply voltage (no drain modulation),
- Case II – $10\,W$ GaN dual-band ET PA using $a_{LF}(t)$, and
- Case III– $10\,W$ GaN dual-band ET PA using $a_{DB}(t)$, given in equation (4.6).

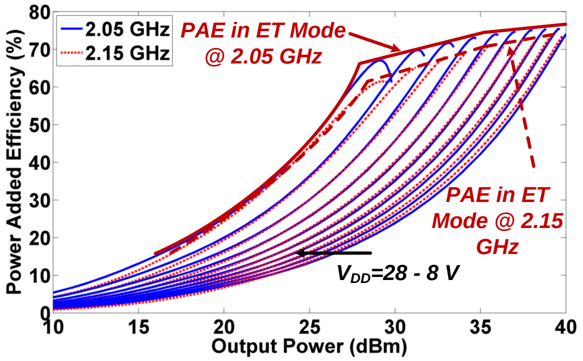

Figure 4.4: Measured continuous wave power added efficiency of the 10 W GaN PA versus supply voltage variation at 2.05 GHz and 2.15 GHz.

Table 4.1: Simulation results of 10 W GaN dual-band ET PA (Does not include losses of the envelope amplifier).

Technique	**Avg. Efficiency**	**Avg. Power (dBm)**	**Gain (dB)**	**Env. BW (MHz)**
Constant Supply PA	27.5%	31.4	16.3	–
LFC-Env ET PA	60.2%	31.3	12.2	5
DB-Env ET PA	63.5%	31.0	12.1	105

An ideal envelope amplifier without bandwidth limitation was employed in the co-simulation. Note that the envelope amplifier for Case III required more than 105 MHz bandwidth which is not feasible in practice.

The simulation results are summarized in Table 4.1. Note that the efficiency values do not include losses in the envelope amplifier and the PA is not linearized. The efficiency of the PA in Case II dropped by less than 4% as a result of employing $a_{LF}(t)$ rather than $a_{DB}(t)$. Note that this corresponds to $\gamma_{CF} = 94.5\%$ which is in good agreement with the calculated efficiency contraction factor discussed in Section 4.2.2. Employing the proposed simplification for a dual-band ET PA would be especially beneficial as the frequency spacing increases beyond a few hundreds of megahertz making dual-band ET operation feasible. Assuming that an envelope amplifier can achieve 75% efficiency under the Case II scenario, the ET PA's overall efficiency would be 18% higher than that of the constant supply PA.

Figure 4.5 shows the simulated input-output and AM/PM of the dual-band ET PA for Case II and III. As is evident from the spread of the input-output relationship, the dual-band ET PA using $a_{LF}(t)$ exhibits more memory effects, supporting the analysis of Section 4.2.3. Note that

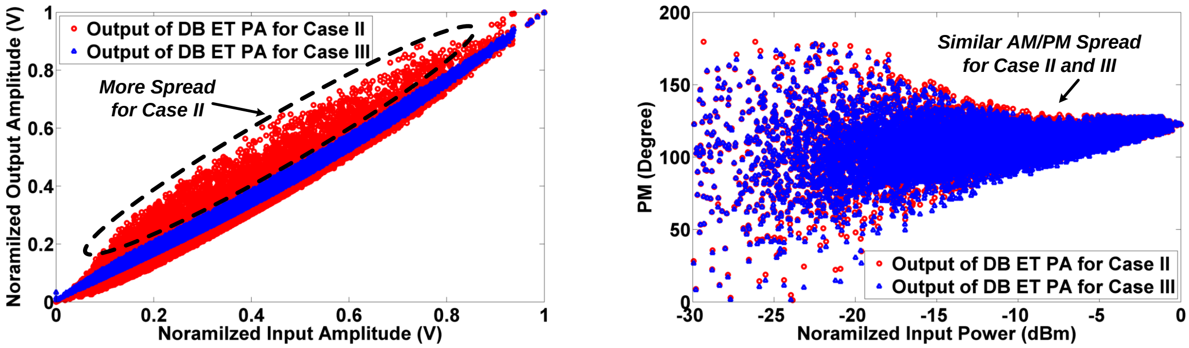

(a) Simulated input-output of the dual-band ET PA for Case II and III

(b) Simulated AM/PM of the dual-band ET PA for Case II and III

Figure 4.5: Simulated (a) input-output and (b) AM/PM of the dual-band ET PA for Case II and III.

the spread in the case of AM/PM is the same for both Cases II and III which is due to the linear output capacitance of the GaN transistor. Even though Case III provides higher efficiency and better linearity, it is not feasible for practical implementation due to the excessive bandwidth requirements of the envelope amplifier (beyond hundreds of megahertz). It will be shown in Section 4.3 that the added source of memory effects in Case II can be compensated for using an appropriate DPD model.

4.3 Dual-Band ET PA Linearization

As discussed in Section 4.2.3, concurrent dual-band ET operation using $a_{LF}(t)$ introduces new sources of nonlinearity, especially amplitude distortion. Existing dual-band DPD models cannot be applied to linearize the additional sources of distortion in concurrent dual-band ET PAs. In this section, we begin by presenting a brief overview of the existing DPD models for linearizing dual-band constant supply PAs; then propose a new dual-band DPD model that is capable of modeling and linearizing dual-band ET PAs.

4.3.1 Modeling and Linearization of Dual-Band PAs in Literature

Conventionally, behavioral modeling employed in DPD for single-band signals, treat the PA as a single-input single-output (SISO) envelope processing system. Assume the real RF PA behavior is expressed as:

$$y(t) = f(x(t)), \tag{4.19}$$

where $x(t)$ and $y(t)$ are the real RF input and output signals of the PA, respectively, and $f(.)$ is the real RF describing function of the PA behavior. In behavioral modeling, the PA is modeled using the baseband equivalent (BBE) of the input and output signals as,

$$\tilde{y}(n) = \tilde{f}(\tilde{x}(n)), \tag{4.20}$$

where $\tilde{x}(n)$ and $\tilde{y}(n)$ are the BBE input and output of the PA, respectively, and $\tilde{f}(.)$ is its describing function. Note that the real RF input/output signals are determined as a function of their BBE as,

$$\begin{aligned} x(n) &= Re\left(\tilde{x}(n)e^{j\omega_0 t}\right), \\ y(n) &= Re\left(\tilde{y}(n)e^{j\omega_0 t}\right), \end{aligned} \tag{4.21}$$

where ω_0 is the center frequency of the modulated signal, and $Re(.)$ denotes the real part of a complex number. The describing function is typically constructed using memory polynomials (MP), Volterra series or another approach to model static and dynamic nonlinear characteristics of the PA. This approach cannot be applied to model or linearize dual-band PAs as it would involve excessive sampling frequency depending on the spacing between the two bands. Alternatively, a dual-band PA can be treated as a dual-input dual-output (DIDO) system according to,

$$\tilde{y}_i(n) = \tilde{f}_i(\tilde{x}_1(n), \tilde{x}_2(n)), \tag{4.22}$$

where $\tilde{x}_i(n)$ and $\tilde{y}_i(n)$ are the BBE inputs and outputs of the dual-band PA for band i, respectively, and $\tilde{f}_i(.)$ is the describing function of the PA behavior around band i. It is worth mentioning that the baseband signals, $\tilde{x}_i(n)$ and $\tilde{y}_i(n)$, are sampled at a frequency which is only two to five times the largest bandwidth of both signals, independent of the frequency separation between the two bands.

Various describing functions have been proposed to generalize single-band DPD models to generate dual-band DPD models in the literature, such as [104–106]. For example, the MP model was generalized in [104] to form a two dimensional DPD model (2D−DPD) which expresses the PA behavior in each band through a polynomial function that uses the two baseband input signals as arguments. The 2D-DPD expresses the BBE output of each band as a function of the BBE inputs as:

$$\tilde{y}_i(n) = \sum_{m=0}^{M-1} \sum_{k=0}^{N-1} \sum_{l=0}^{k} a_{klm}^{(i)} \tilde{x}_i(n-m) |\tilde{x}_1(n-m)|^{(k-l)} |\tilde{x}_2(n-m)|^{l}, \tag{4.23}$$

where $a_{mkl}^{(i)}$ are the model coefficients for band i, and N and M denote the nonlinearity order and memory depth, respectively. The 2D-DPD model has shown good capacity to linearize dual-band PAs. However, the model involves a large number of coefficients and suffers from numerical instability and sensitivity to time misalignment. In [105], authors exploited the cross-band modulation effects to modify the envelope terms of the conventional MP model and develop a two-dimensional modified MP (2D$-$MMP) formulation. According to authors in [105], the 2D$-$MMP yielded a lower number of coefficients compared to the 2D$-$DPD while maintaining the linearization capacity.

A dual-band DPD model based on Volterra series was proposed in [106], called dual-band BBE Volterra. Authors in [106] started with a real-valued passband RF Volterra expression and applied various signal transformations and derivations to generate a dual-band BBE model capable of accurately mimicking or linearizing a dual-band PA. This model included a relatively small number of coefficients while encompassing all possible distortion terms. To illustrate, the expression of the dual-band BBE Volterra DPD is given for the case of 3^{rd} order nonlinearity for simplicity:

$$\tilde{y}_i(n) = \tilde{y}_{i,1}(n) + \tilde{y}_{i,3}(n), \tag{4.24}$$

where $\tilde{y}_{i,k}(n)$ is the k^{th} order distortion term of the output for band i which includes both self-distortion and inter-distortion terms. The 1^{st} and 3^{rd} order distortion terms are defined using Volterra kernels as,

$$\begin{aligned}
\tilde{y}_{i,1}(n) &= \sum_{l_1=0}^{M_1} \tilde{h}_{i,1}(l_1)\tilde{x}_{i,1s}(n,l_1), \\
\tilde{y}_{i,3}(n) &= \sum_{l_1=0}^{M_{3,s}} \sum_{l_2=0}^{M_{3,s}} \sum_{l_3=0}^{M_{3,s}} \tilde{h}_{i,3s}(l_1,l_2,l_3)\tilde{x}_{3,s}(n,l_1,l_2,l_3), \\
&+ \sum_{l_1=0}^{M_{3,d}} \sum_{l_2=0}^{M_{3,d}} \sum_{l_3=0}^{M_{3,d}} \tilde{h}_{i,3d}(l_1,l_2,l_3)\tilde{x}_{3,d}(n,l_1,l_2,l_3),
\end{aligned} \tag{4.25}$$

where $\tilde{h}_{i,1}$, $\tilde{h}_{i,3s}$ and $\tilde{h}_{i,3d}$ are the impulse responses of the Volterra kernels for the self- and inter-distortions of order 1 and 3 ($\tilde{x}_{1,s}$,$\tilde{x}_{3,s}$ and $\tilde{x}_{3,d}$) respectively, and M_1, $M_{3,s}$ and $M_{3,d}$ denote the memory depth of the 1^{st} and 3^{st} distortion terms, respectively. The dual-band BBE Volterra showed great capacity for the linearization of dual-band PAs while using a small number of coefficients; however, the model requires pre-computation of the BBE Volterra kernels. Another dual-band DPD model was proposed in [107], where the authors extend the generalized MP (GMP) [108] to model DIDO PAs. The resulting dual-band complexity reduced GMP (2D-CR-GMP) model achieved similar linearization performance to 2D-DPD with a smaller number of coefficients, as well as reduced sensitivity to time misalignment between the two signals. The general formulation of 2D-CR-GMP is given as:

$$
\begin{aligned}
\tilde{y}_i(n) = &\sum_{\substack{k=1\\odd}}^{2N_i-1} \sum_{\substack{r=0\\even}}^{k} \delta \tilde{x}_i(n)|\tilde{x}_1(n)|^{k-r-1}|\tilde{x}_2(n)|^{r} \\
&+ \sum_{\substack{k=2\\even}}^{N_i-1} \sum_{\substack{q=2\\even}}^{\hat{N}-1} \sum_{\substack{r=0\\even}}^{k-1} \sum_{\substack{s=0\\even}}^{q} \sum_{j=1}^{M(m_1)} \alpha \tilde{x}_i(n)|\tilde{x}_1(n)|^{k-r-2}|\tilde{x}_2(n)|^{r}|\tilde{x}_2(n-j)|^{s} \\
&+ \sum_{\substack{k=1\\odd}}^{N_i} \sum_{\substack{q=1\\odd}}^{\hat{N}} \sum_{\substack{r=0\\even}}^{k-1} \sum_{\substack{s=0\\even}}^{q} \sum_{j=1}^{M(m_2)} \beta \tilde{x}_i(n-j)|\tilde{x}_1(n)|^{k-r-1}||\tilde{x}_1(n-j)|^{q-s-1}|\tilde{x}_2(n)|^{r}|\tilde{x}_2(n-j)|^{s}, \quad (4.26)
\end{aligned}
$$

where δ, α, and β are the model coefficients, and,

$$
\begin{aligned}
\hat{N} &= \max(N_1, N_2), \\
m_1 &= \Big(1 + (k-r-2) + ((q-s) + r + s) + 1\Big)/2, \\
m_2 &= \Big(1 + (k-r-1) + ((q-s-1) + r + s) + 1\Big)/2. \quad (4.27)
\end{aligned}
$$

All of the aforementioned DPD models were developed and validated for PA topologies with a constant drain supply voltage. While these DPD models work adequately for Doherty and constant supply PAs, they fail to linearize concurrent dual-band ET PAs, as proposed in this thesis. To the best of our knowledge, linearization results for concurrent dual-band ET PAs under modulated signal tests have not been reported in the literature. In the next section, we present a dual-band DPD model capable of linearizing concurrent dual-band ET PAs.

4.3.2 Proposed Dual Band Volterra Series for ET PAs

In order to capture the extra sources of nonlinearity in dual-band ET PAs, either the dual-band BBE Volterra or 2D-CR-GMP could be extended to incorporate the distortion attributed to the drain supply modulation. To achieve this, the BBE of the output signal in each band can be expressed as a function of the envelope of the input signals, $\tilde{x}_1(n)$ and $\tilde{x}_2(n)$, as well as the supply voltage, $V_{DD}(n)$, as:

$$\tilde{y}_i(n) = \tilde{f}_i(\tilde{x}_1(n), \tilde{x}_2(n)) \times f_{Ei}(V_{DD}(n)), \quad (4.28)$$

where $\tilde{f}_i(.)$ is the dual-band PA describing function without supply modulation (i.e., constant supply) for band i, given in either (4.25) or (4.26), and $f_{Ei}(.)$ describes the dependency of the dual-band PA on the supply voltage for band i. While various expressions can be used for $f_{Ei}(V_{DD}(n))$, in this thesis a polynomial function was chosen as it was found to achieve modeling capability with the lowest complexity. Furthermore, knowing the supply voltage of the dual-band ET PA is controlled using a shaped version of $(|\tilde{x}_1(n)| + |\tilde{x}_2(n)|)$, we can simplify (4.28) to,

$$\tilde{y}_i(n) = \tilde{f}_i(\tilde{x}_1(n), \tilde{x}_2(n)) \times \sum_{l=0}^{N_S-1} \left(c_l^{(i)} \left(|\tilde{x}_1(n)| + |\tilde{x}_2(n)| \right)^l \right), \tag{4.29}$$

where N_S is the nonlinearity order for the supply effect and c_l^i are the model coefficients for band i. Note that this formulation assumes that the output does not depend on the past values of the supply voltage and the memory effects associated with the PA will be captured by $\tilde{f}_i(.)$. It is worth mentioning that this extension from a constant supply to a drain modulated PA can be similarly applied to 2D-DPD and 2D-MMP schemes. The model coefficients in (4.29) can be identified linearly using a least square error (LSE) estimator. The effectiveness of the proposed DPD model was validated using the measurement results of three dual-band ET prototypes as presented in Section 4.5.

4.4 Dual-Band ET PA Design Considerations

In Chapter 3, the sources of nonlinearity in single- and dual-band constant supply PAs, together with a design methodology to improve the linearizability of constant supply PAs was presented. This section discusses the design considerations when the PA is used in an ET system.

4.4.1 Envelope Amplifier Nonidealities

Successful implementation of an ET PA system requires a linear envelope amplifier. Nonidealities in the envelope amplifier can degrade the linearity and linearizability of the ET PA significantly. In order to maintain a high efficiency for the envelope amplifier while providing a wide bandwidth, a linear-assisted switched mode envelope amplifier is typically employed to modulate the drain supply voltage of the PA. A simplified schematic of the linear-assisted switched model envelope amplifier is shown in Figure 4.6. The envelope amplifier is composed of, (i) a linear amplifier that provides the high frequency content of the signal, and (ii) a switched mode buck converter that provides the low frequency content of the signal. This amplifier can achieve

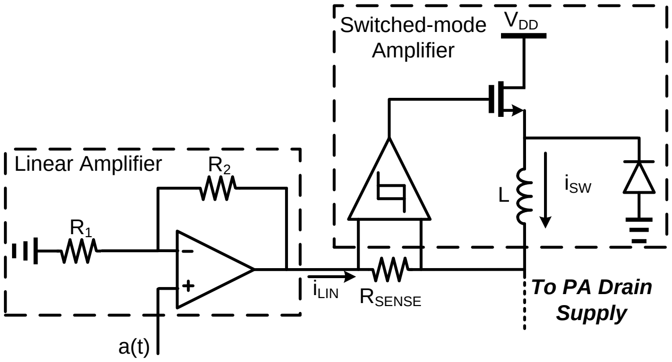

Figure 4.6: Schematic of the linear-assisted switched-mode amplifier used as the envelope amplifier.

more than 70% efficiency for modulation bandwidths of $5 MHz$ to $20 MHz$ [109]. There are three major sources of nonidealities in the envelope amplifier:

- limited slew-rate and bandwidth,
- coupling of ground noise to the PA, and
- nonidealities due to envelope amplifier's varying load.

The effect of these nonidealities on ET PAs will be discussed separately.

If the slew-rate and/or bandwidth of the envelope amplifier is insufficient, the output of the envelope amplifier, i.e., the supply voltage of the PA, will no longer represent the envelope of the RF signal. As a result of limited slew-rate of the envelope amplifier, the supply voltage will not be able to reach its desired value when PA's envelope is varying rapidly. This may result in the drain supply voltage of the PA to be smaller than the required value, hence, resulting in early saturation of the PA. This will degrade the linearity and linearizability of the ET PA significantly. Typically, improving slew-rate and/or bandwidth of the envelope amplifier requires larger biasing current for the linear amplifier which degrades the efficiency of the envelope amplifier. The slew-rate and bandwidth requirement of the envelope amplifier can be reduced to some extent by shaping the envelope. This will be further discussed in Section 4.4.2.

Another source of nonideality in the envelope amplifier is the ground noise. The envelope amplifier generates a significant amount of ground noise due to the switching stage. This switching noise is typically in the order of few megahertz (similar to the bandwidth of the envelope signal). In practice, when the envelope amplifier is connected to the PA, part of the switching noise couples to the ground of the PA. The coupled switching noise can then mix with the RF signal and create in-band distortion at the output of the PA which degrades EVM and ACPR of the PA. The effect of switching can be minimized by decoupling the RF ground and the envelope amplifier's ground.

Lastly, output of the envelope amplifier will be distorted as the result of its varying load. The envelope amplifier is typically designed to provide the appropriate current and voltage for the PA. The performance of the envelope amplifier is tested separately when driving a capacitor in parallel with a constant resistive load corresponding to the peak DC power required by the PA, as shown in Figure 4.7(a). In practice, the envelope amplifier will see a varying resistive load depending on the efficiency profile of the PA, as shown in Figure 4.7(b). This will result in high slew-rate requirement for the linear amplifier compared to the constant resistive load. Hence, it is important to take the varying load of the PA into account from the early stages of the design of the envelope amplifier, otherwise, the output of the envelope amplifier will be distorted which may degrade the linearity and linearizability of the ET PA.

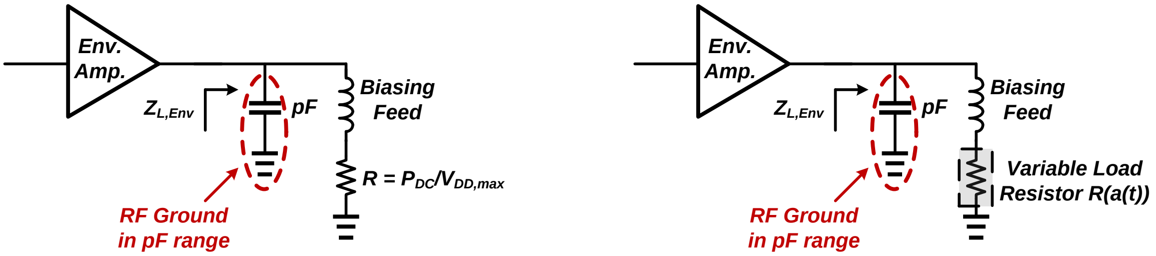

(a) PA is modeled using a fixed resistive load

(b) PA is modeled using a varying resistive load

Figure 4.7: The equivalent model of the envelope amplifier's load using a (a) fixed resistive load, and (b) varying resistive load.

4.4.2 Envelope Shaping

In order to improve the efficiency and linearity of ET PAs, the drain supply voltage is typically modulated according to the shaped envelope of the signal, rather than the original envelope. Different envelope shaping/modification techniques have been proposed in the literature for single-band ET PAs to partially alleviate the slew-rate/bandwidth and linearity/dynamic range requirements of the envelope amplifier [35, 110]. For example, authors in [35] suggested the reduction

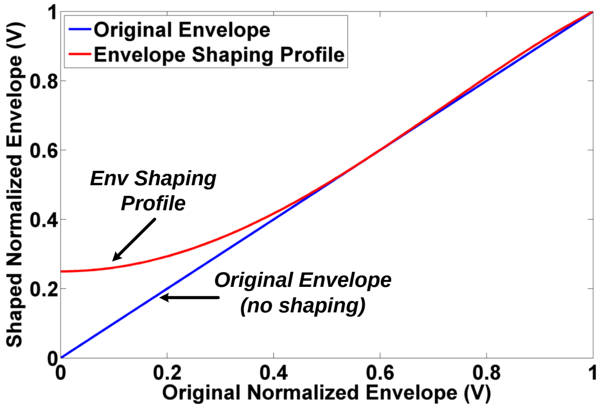

Figure 4.8: The envelope shaping function based on (4.30) where $a_{min} = 0.25$.

of the bandwidth of the supply through iterative low-pass filtering of the original envelope signal. Filtering the envelope signal adds extra sources of memory effects for ET PAs, especially for wideband signals. In [110], authors investigated multiple memoryless envelope shaping functions and studied their effects on the efficiency of the ET PA (note that the modulation bandwidth was limited to $5\,MHz$). A memoryless envelope shaping function based on $a^2(t)$ was introduced in [111]. This class of shaping function benefits from the fact that the bandwidth of $a^2(t)$ is limited to the RF bandwidth as it only includes a linear combination of $I^2(t)$ and $Q^2(t)$. The general form of the envelope shaping function is given as,

$$\hat{a}(t) = c_0 + c_1 a^2(t) + c_2 a^4(t), \tag{4.30}$$

where $a(t)$ and $\hat{a}(t)$ are the original and shaped envelope signals respectively, and c_0, c_1 and c_2 are constant coefficients that are determined using the signal PAPR and knee voltage to ensure $\hat{a}(t) > a(t)$ and $\min(\hat{a}) = a_{min}$. Figure 4.8 depicts an envelope shaping function based on (4.30) where $a_{min} = 0.25$, corresponding to $12\,dB$ of dynamic range.

For dual-band ET PAs, envelope shaping can be similarly applied to the LFC of the envelope of the dual-band signal to reduce the linearity requirement of the envelope amplifier and improve the efficiency of the dual-band ET PA as in:

$$\hat{a}_{LF}(t) = f\left(a_{LF}(t)\right), \tag{4.31}$$

where $\hat{a}_{LF}(t)$ and $a_{LF}(t)$ are the shaped and original LFC of the dual-band envelope and $f(.)$ is the envelope shaping function. Figure 4.9 shows the spectrum of the LFC of the dual-band envelope before and after shaping for a dual-band downlink LTE $5\,MHz$ and a single-carrier WCDMA signal.

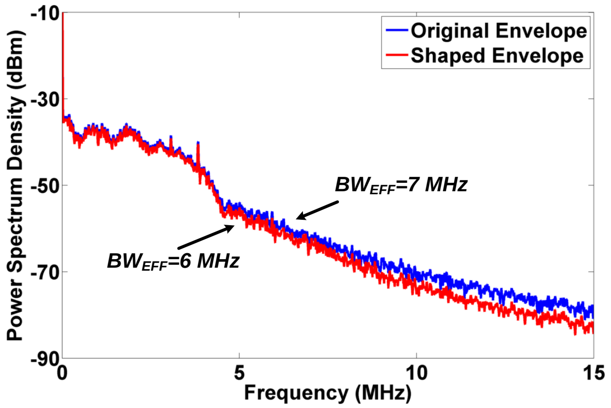

Figure 4.9: Spectrum of the original and shaped LFC of the envelope of the dual-band LTE and WCDMA signal.

4.4.3 PA and Envelope Amplifier Interface Considerations

The interface between the envelope amplifier and the PA plays an important role on the linearity and linearizability of the ET PA. It is important that the output of the envelope amplifier provides low impedance for the PA at all frequencies. In single-band ET PA, the output impedance of the envelope amplifier at carrier frequency, f_c, its harmonics, and baseband frequency (from DC up to five times the modulation bandwidth) should be very small. The envelope amplifier provides low impedance within its bandwidth, i.e., at baseband frequency. The output impedance of the envelope amplifier at f_c and its harmonics can be reduced using decoupling capacitors in the range of pico Farads (pF).

In the case of a dual-band ET PA, the output of the envelope amplifier should provide a low impedance at: carrier frequencies (f_{c1} and f_{c2}) and their harmonics, baseband frequency (up to 5 times the modulation bandwidth) and the separation frequency ($f_{c1} - f_{c2}$) and its harmonics. In this case, the decoupling capacitors should reduce the impedance of the envelope amplifier at the separation frequency too. Hence, for dual-band ET PAs, decoupling capacitors includes capacitances in the range of pF for carrier frequencies, and in the range of nano Farads (nF) for separation frequency, as shown Figure 4.10. This means that the envelope amplifier should be able to drive a fairly large capacitive load which typically degrades its slew rate and bandwidth. It should be noted that the linearizability of the dual-band ET PA will be compromised if the output impedance of the envelope amplifier is large at $f_{c1} - f_{c2}$. This will pracitcally limit the application of the proposed dual-band ET PA approach to dual-band signals with small carrier spacing. Note that for small carrier spacing, such as $60\,MHz$ or less, the required decoupling

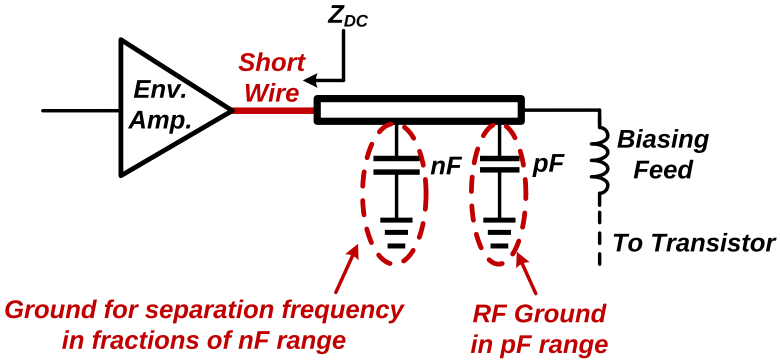

Figure 4.10: Large decoupling capacitors are required at the PA and envelope amplifier interface.

capacitor will be so large that the envelope amplifier will not be able to drive the large capacitive load.

4.4.4 Time Alignment

The time alignment between the RF signals and the envelope amplifier influence the linearity and linearizability of the dual-band ET PA significantly. Any misalignment between the two RF signals individually, or a delay between the envelope and RF path, can result in poor linearity for the ET PA. Maintaining time alignment between the RF and the envelope path is more challenging in practice as the two frequencies are so far apart. The time alignment for the dual-band ET PA is done during the measurements in two steps.

Step 1 – Ensure the two RF signals are time aligned. Any group delay differences between the two bands results in the two RF signals combining with a time-delay which will change the envelope of the dual-band signal, as well as its PAPR. Furthermore, typical dual-band DPD models assume the two signals are perfectly time aligned. The group delay difference of the measurement setup can be estimated in MATLAB® without the device under test (DUT) by downloading the two RF signals separately in each band.

Step 2 – Adjust the timing of the RF path and the envelope signal. Note that this task is more challenging as the two signals are on different time scales (especially as the signal modulation bandwidth increases). The RF and the envelope paths can be time aligned using a high speed dual-channel oscilloscope. The envelope of the RF signal is extracted in MATLAB® by downloading the time-domain signal using the high speed scope. The time-delay difference between

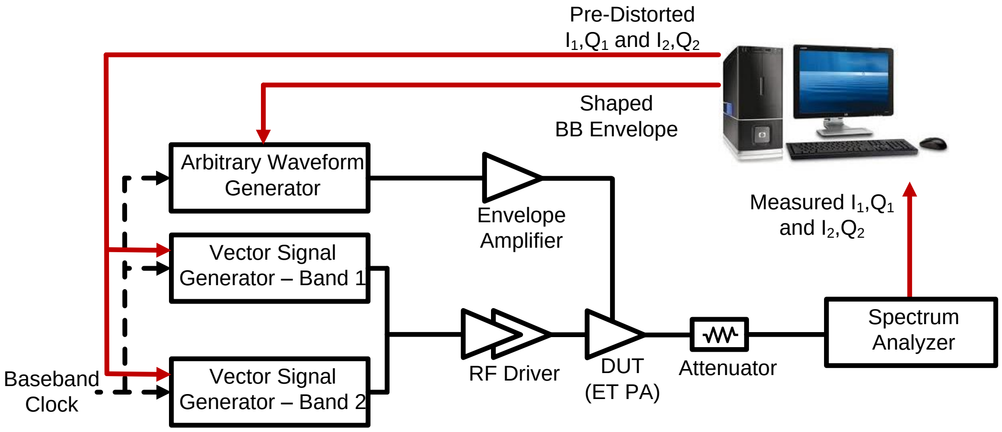

Figure 4.11: The measurement setup for the dual-band ET PA.

the envelope path and the extracted envelope of the RF signal is calculated in MATLAB® and then used to align the RF and envelope path.

4.5 Dual-Band ET PA Measurement Results

The proposed concurrent dual-band ET PA performance was evaluated using the measurement setup shown in Figure 4.11. The measurement setup consisted of two signal generators (with baseband time alignment), a vector signal analyzer, an arbitrary waveform generator for the envelope signal and an RF driver. All the signal sources used the same baseband clock and were time aligned. The DPD model coefficients were identified and applied using a PC running MATLAB®. Figure 4.12 shows the block diagram of the proposed dual-bad ET PA system.

Two proof-of-concept prototypes were used to validate the proposed concurrent dual-band ET approach.

- Prototype I – A 45 W GaN ET PA consisted of a 45 W broadband GaN PA (the same PA presented in Chapter 3) and a linear-assisted switched mode envelope amplifier (see Figure 4.6). The PA operated from 750 MHz to 1 GHz and achieved peak output power and efficiency of 46 dBm and 75%, respectively, with more than 16 dB of gain when operating from a constant 28 V supply. The linear-assisted switched mode envelope amplifier achieved 70% average efficiency while amplifying the envelope of a WCDMA signal with PAPR of 9.0 dB [109]. Figure 4.13 shows the photograph of the envelope amplifier.

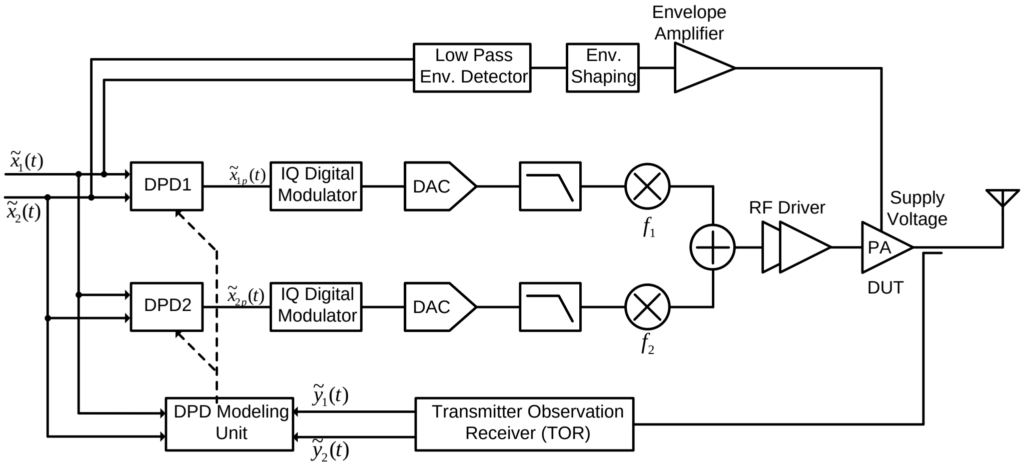

Figure 4.12: Block diagram of the proposed concurrent dual-band ET PA system.

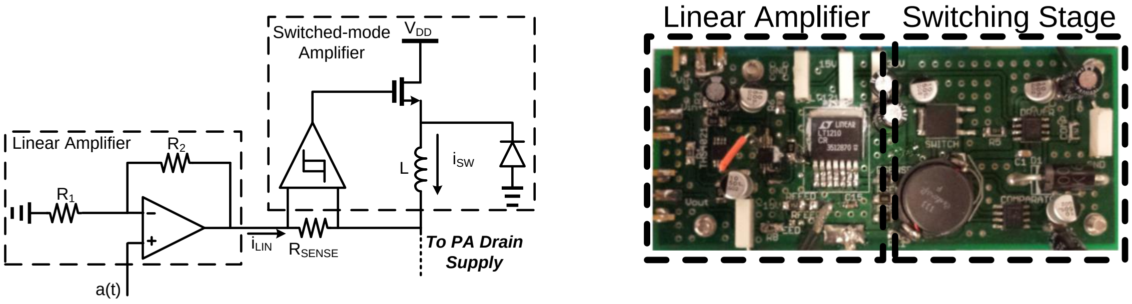

(a) (b)

Figure 4.13: Photograph and schematic of the linear-assisted switched mode envelope amplifier.

- Prototype II – A 45 W GaN ET PA consisting of a 45 W broadband class B/J GaN PA (presented in [101]) and a linear-assisted switched mode envelope amplifier. The PA was operated from 1.9 GHz to 2.9 GHz and achieved a peak output power and drain efficiency of 45.0 dBm and 67%, respectively, under constant drain supply voltage operation (28 V). The same envelope amplifier as in Prototype II was used for this dual-band ET PA.

4.5.1 Prototype I Measurement Results

The 45 W broadband GaN PA was measured and linearized in both stand-alone and ET modes of operation. The dual-band GaN ET PA was successfully linearized when amplifying a dual-band downlink two-carrier WCMDA and LTE 10 MHz signals (both signals with 10 MHz modulation bandwidth) at 0.75 GHz and 0.95 GHz, respectively, with a combined PAPR of 9.2 dB. The dual-band ET PA was linearized using proposed dual-band DPD model with supply dependency with $N = 5$, $M = 2$, and $N_S = 3$, resulting in 63 coefficients per band. Figure 4.14 shows the measured spectrum of the output of the dual-band ET PA with and without DPD. The dual-band ET PA achieved 40% overall efficiency (including the losses of the envelope amplifier) at 37 dBm output power, showing 10% improvement in efficiency over the constant supply PA. Note that the relatively low overall efficiency of the dual-band ET PA is due to an inefficient envelope amplifier employed in the measurements. The envelope amplifier's estimated efficiency when amplifying the LFC of the envelope of the dual-band signal is 67% which results in an estimated 59.7% efficiency for the ET PA (excluding losses in the envelope amplifier).

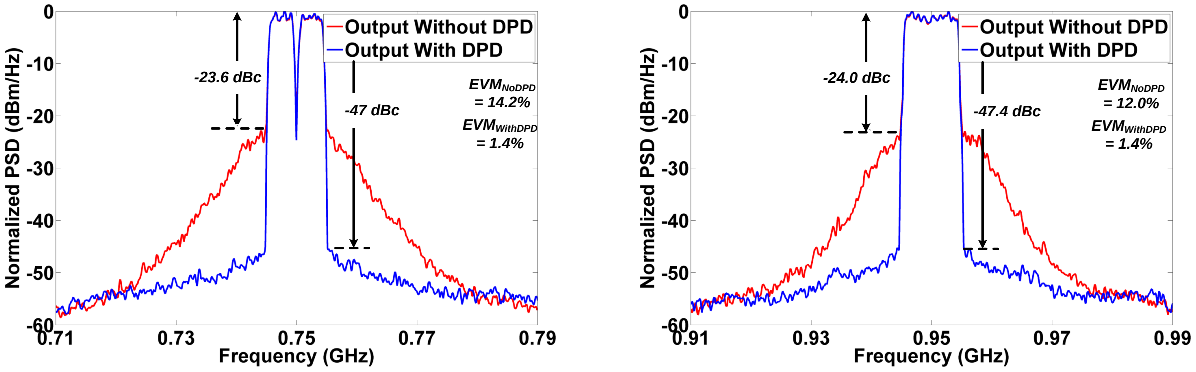

(a) Band 1 – Two-carrier WCDMA

(b) Band 2 – LTE 10 MHz

Figure 4.14: Measured spectrum of the output of Prototype I, (two-carrier WCMDA at 0.75 GHz and LTE 10 MHz at 0.95 GHz) with and without DPD.

The dual-band ET PA was further validated when amplifying dual-band signals with uneven power for the two bands. In practice, carrier aggregated signals may require the PA to operate in different output power scenarios too. In order to test the capability of the proposed dual-band ET approach for carrier aggregated signals, the 45 W GaN ET PA was also linearzied when amplifying a downlink LTE 5 MHz and single-carrier WCDMA signals at 0.78 GHz and 0.88 GHz, respectively, for two scenarios for the output power;

- Case I – Output power at band I and II are equal,
- Case II – Output power at band II is $11\,dB$ lower than band I.

In both cases, the ET PA was successfully linearized using the proposed dual-band DPD model with supply dependency with 63 coefficients per band. An ACPR and EVM of better than $-47\,dB$ and 1.6% were achieved for both bands in all cases. Figure 4.15 and 4.16 show the measured spectrum of both bands for Cases I and II respectively. The dual-band ET PA achieved 45% and 41% overall drain efficiency (including the losses in the envelope amplifier) at $39\,dBm$ and $38\,dBm$ average output power for Cases I and II respectively. Note that based on the estimated efficiency of the envelope amplifier, the PA average efficiency in ET mode was approximated to 65%. The complete measured spectrum of the dual-band ET PA in Case II before and after linearization is depicted in Figure 4.17.

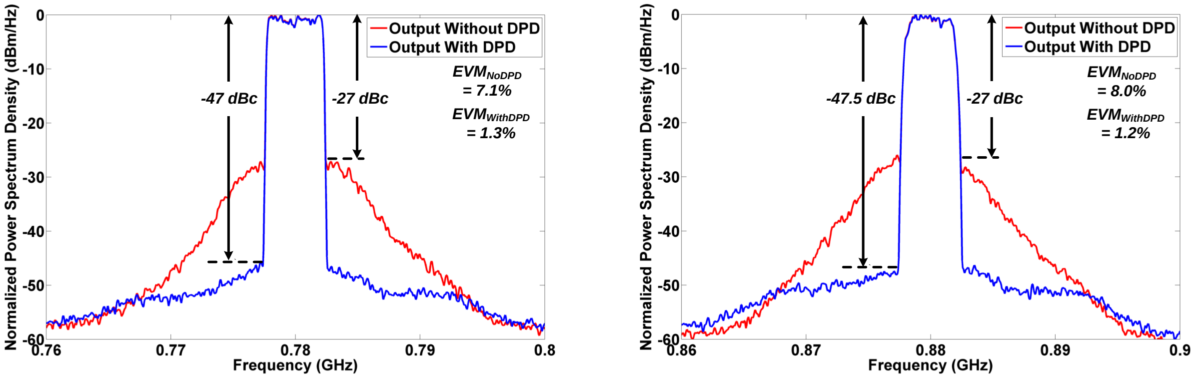

(a) Band 1 – LTE $5\,MHz$

(b) Band 2 – WCDMA

Figure 4.15: Measured spectrum of the output of Prototype I, (LTE $5\,MHz$ at $0.78\,GHz$ and single-carrier WCMDA at $0.88\,GHz$) with and without DPD for Case I.

4.5.2 Prototype II Measurement Results

In order to show the proposed concurrent dual-band ET operation is not frequency dependent, a $45\,W$ broadband class-B/J GaN PA operating from $1.9\,GHz$ to $2.9\,GHz$ was also measured and linearized in dual-band ET mode of operation. The dual-band ET PA was successfully linearized when driven with a dual-band downlink two-carrier WCDMA and LTE $10\,MHz$ signals at different carrier spacings. Figure 4.18 and 4.19 shows the measured spectrum of the dual-band ET

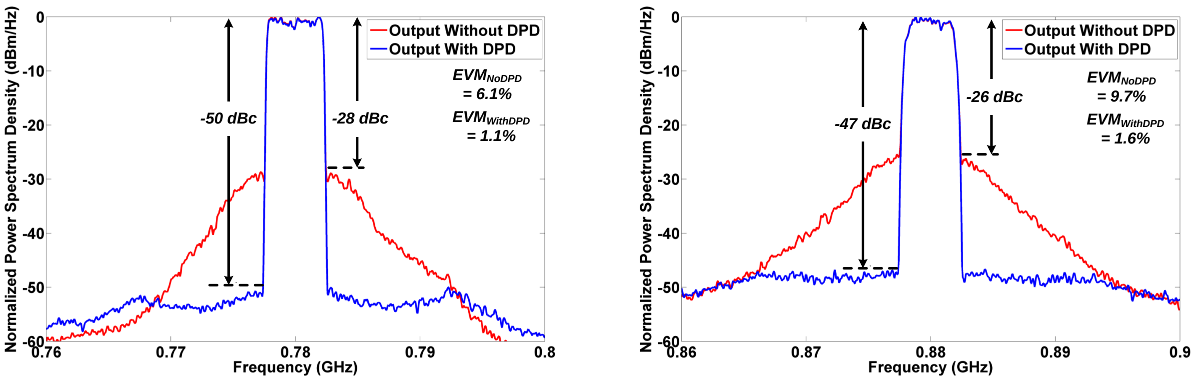

(a) Band 1 − LTE 5 MHz

(b) Band 2 − WCDMA

Figure 4.16: Measured spectrum of the output of Prototype I, (LTE 5 MHz at 0.78 GHz and single-carrier WCMDA at 0.88 GHz) with and without DPD for Case II.

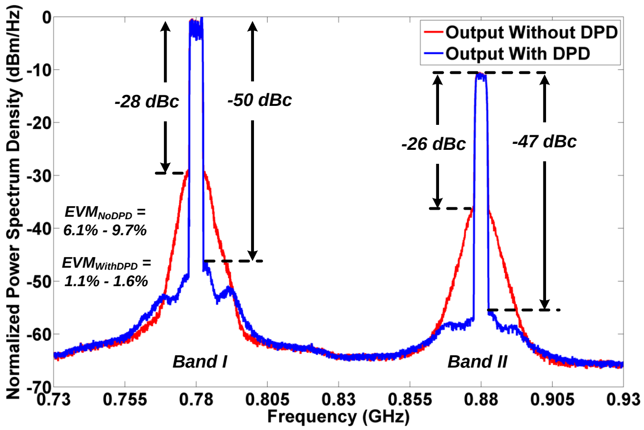

Figure 4.17: Measured spectrum of the output of the Prototype III before and after linearization when the power at band II is 11 dB lower than band I.

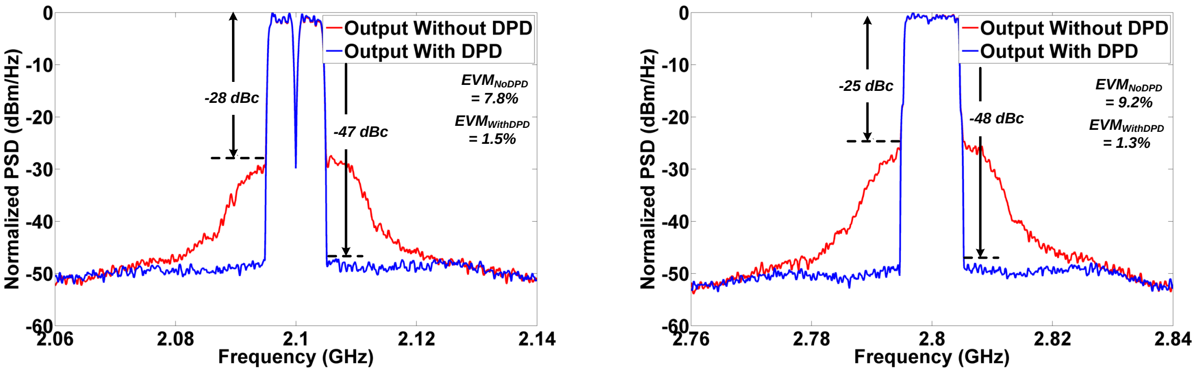

(a) Band 1 – Two-carrier WCDMA

(b) Band 2 – LTE 10 MHz

Figure 4.18: Measured spectrum of the output of Prototype II, (two-carrier WCMDA at 2.1 GHz and LTE 10 MHz band at 2.8 GHz) with and without DPD.

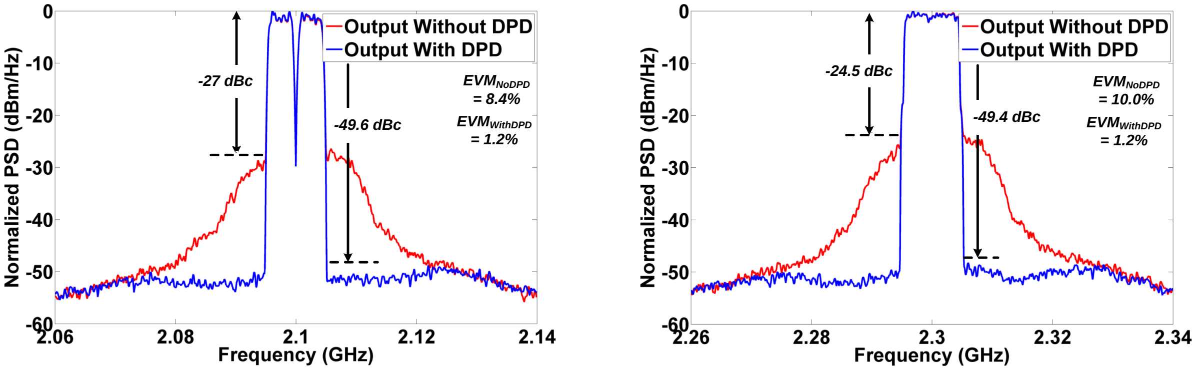

(a) Band 1 – Two-carrier WCDMA

(b) Band 2 – LTE 10 MHz

Figure 4.19: Measured spectrum of the output of Prototype II, (two-carrier WCMDA at 2.1 GHz and LTE 10 MHz band at 2.3 GHz) with and without DPD.

PA output with and without DPD when the carriers are $2.1\,GHz/2.8\,GHz$ and $2.1\,GHz/2.3\,GHz$, respectively. The dual-band ET PA achieved 38.7% and 39% overall efficiencies (including the losses of the envelope amplifier) at $37.1\,dBm$ and $37.2\,dBm$ output powers, respectively, showing approximately 11% improvement over the constant supply PA. The estimated efficiency of the dual-band ET PA excluding the losses of the envelope amplifier is 58%. Table 4.2 summarizes the measurement results of all the two prototypes.

4.6 Conclusion

In this chapter a feasible approach to concurrent dual-band transmission using an ET PA was presented without posing excessive bandwidth/linearity requirements on the envelope amplifier. Based on the analysis of the envelope of the combined dual-band signals, a simplification was proposed to realize a concurrent dual-band ET PA using the LFC of the envelope of the dual-band signal. The effect of this simplification on the efficiency and linearity of the dual-band ET PA was studied and shown to result in only minor efficiency contraction. The additional sources of distortion attributed to the simplification were successfully compensated for using the proposed dual-band DPD model with supply dependency. The proposed approach enables the amplification of inter-band and intra-band non-contiguous carrier aggregated signals using ET PAs. It is important to note that as a result of large decoupling capacitances, the proposed dual-band ET approach is practically limited to dual-band signals with more than $100\,MHz$ carrier spacing. The effectiveness of this simplification for dual-band ET operation was validated with measurement results for two PA prototypes operating at various frequencies. In all cases, the dual-band ET PA was successfully linearized to meet the linearity requirements for base station applications.

Table 4.2: Summary of the dual-band ET PA measurement results for all the prototypes.

		Band 1 – WCDMA				**Band 2 – LTE**				**Concurrent dual-band**	
Operation Mode		**ACPR (dBc)**	**EVM (%)**	**PAPR (dB)**	**NMSE (dB)**	**ACPR (dBc)**	**EVM (%)**	**PAPR (dB)**	**NMSE (dB)**	**Power (dBm)**	**Avg. PA Eff.**
Prototype I [1]	No DPD	−26.0	14.2%	7.2	−37.7	−27.0	12.0%	9.6	−38.1	37.1	59.9%[2]
	With DPD	−47.5	1.4%	7.7	–	−47.7	1.4%	8.6	–	37.0	59.7%
Prototype I – Case I	No DPD	−30.3	8.0%	8.5	−40.0	−29.1	7.7%	9.0	−40.1	39.0	64.7%
	With DPD	−47.7	1.3%	7.5	–	−47.0	1.2%	7.4	–	38.9	64.3%
Prototype I – Case II	No DPD	−31.9	6.1%	7.6	−39.9	−27.5	9.7%	7.7	−38.0	38.0	58.6%
	With DPD	−51.2	1.1%	7.5	–	−47.1	1.6%	7.4	–	38.1	58.7%
Prototype II [3]	No DPD	−29.0	8.4%	8.8	−39.0	−27.4	10.0%	9.3	−37.6	37.2	58.2%[4]
	With DPD	−49.7	1.2%	7.7	–	−49.6	1.2%	8.6	–	36.9	57.5%
Prototype II [5]	No DPD	−28.3	9.2%	9.1	−38.5	−29.5	7.8%	8.4	−38.0	37.1	58%
	With DPD	−48.0	1.3%	7.7	–	−47.5	1.5%	8.6	–	37.0	57.5%

[1] The two signals are separated by $200\,MHz$ at $0.75\,GHz$ and $0.95\,GHz$ with $10\,MHz$ modulation bandwidth.

[2] Efficiency is estimated knowing the envelope amplifier's efficiency is approximately 67%.

[3] The two signals are separated by $200\,MHz$ at $2.1\,GHz$ and $2.3\,GHz$ with $10\,MHz$ modulation bandwidth.

[4] Efficiency is estimated knowing the envelope amplifier's efficiency is approximately 67%.

[5] The two signals are separated by $700\,MHz$ at $2.1\,GHz$ and $2.8\,GHz$ with $10\,MHz$ modulation bandwidth.

Chapter 5

Concurrent Tri-Band ET PA

5.1 Introduction

In this chapter, the concurrent dual-band ET operation presented in Chapter 4 will be generalized to tri- and multi-band signals. Few recent publications, such as [112, 113], have investigated concurrent tri-band operation of constant supply PAs. However, concurrent tri-band operation of ET PAs has not been demonstrated in the literature. This chapter proposes the principle of concurrent multi-band operation of ET PAs utilizing the low-frequency envelope of a multi-band signal to modulate the drain supply of the ET PA. Linearity and efficiency analyses of the proposed concurrent multi-band ET PA will be presented in this chapter. The effectiveness of the proposed solution is verified using simulation and measurement results from a concurrent tri-band ET PA which is linearized using a proposed tri-band DPD technique that takes the effect of drain modulation into account.

5.2 Concurrent Tri-Band ET Operation

5.2.1 Basic Principle

Similar to concurrent dual-band ET operation, concurrent multi-band operation of ET PAs requires better understanding of the envelope of a multi-band signal. We start by formulating the envelope of a tri-band signal and later generalize the result to multi-band signals with more than three carriers. Assume the tri-band signal is composed of three modulated signals expressed as:

$$\begin{aligned}
v_1(t) &= I_1(t)\cos(\omega_{c1}t) + Q_1(t)\sin(\omega_{c1}t) = Re\left(\tilde{v}_1(t)e^{j(\omega_{c1}t)}\right), \\
v_2(t) &= I_2(t)\cos(\omega_{c2}t+\theta_1) + Q_2(t)\sin(\omega_{c2}t+\theta_1) = Re\left(\tilde{v}_2(t)e^{j(\omega_{c2}t+\theta_1)}\right), \\
v_3(t) &= I_3(t)\cos(\omega_{c3}t+\theta_2) + Q_3(t)\sin(\omega_{c3}t+\theta_2) = Re\left(\tilde{v}_3(t)e^{j(\omega_{c3}t+\theta_2)}\right),
\end{aligned} \tag{5.1}$$

where ω_{c1}, ω_{c2}, and ω_{c3} denote the three carrier frequencies, θ_1 and θ_2 represent the phase shift between the carrier frequencies, and $\tilde{v}_1(t)$, $\tilde{v}_2(t)$, and $\tilde{v}_3(t)$ are the complex envelopes of the three signals and defined as:

$$\begin{aligned}
\tilde{v}_1(t) &= I_1(t) + jQ_1(t) = a_1(t)e^{j\phi_1(t)}, \\
\tilde{v}_2(t) &= I_2(t) + jQ_2(t) = a_2(t)e^{j\phi_2(t)}, \\
\tilde{v}_3(t) &= I_3(t) + jQ_3(t) = a_3(t)e^{j\phi_3(t)},
\end{aligned} \tag{5.2}$$

where $a_i(t)$ and $\phi_i(t)$ are the envelope and phase of the signal at band i. The tri-band signal is expressed as,

$$\begin{aligned}
v_{TB}(t) &= v_1(t) + v_2(t) + v_3(t) \\
&= Re\left(\tilde{v}_1(t)e^{j(\omega_{c1}t)} + \tilde{v}_2(t)e^{j(\omega_{c2}t+\theta_1)} + \tilde{v}_3(t)e^{j(\omega_{c3}t+\theta_2)}\right) \\
&= Re\left(\left(\tilde{v}_1(t) + \tilde{v}_2(t)e^{j(\Delta\omega_1 t+\theta_1)} + \tilde{v}_3(t)e^{j(\Delta\omega_{c2}t+\theta_2)}\right)e^{j(\omega_{c1}t)}\right),
\end{aligned} \tag{5.3}$$

where,

$$\begin{aligned}
\Delta\omega_1 &= \omega_{c1} - \omega_{c2}, \\
\Delta\omega_2 &= \omega_{c1} - \omega_{c3}.
\end{aligned} \tag{5.4}$$

The envelope of the tri-band signal can be calculated from (5.3) as,

$$a_{TB}(t) = \left|\tilde{v}_1(t) + \tilde{v}_2(t)e^{j(\Delta\omega_1 t+\theta_1)} + \tilde{v}_3(t)e^{j(\Delta\omega_{c2}t+\theta_2)}\right|, \tag{5.5}$$

Replacing (5.2) in (5.5), and after some derivation, the envelope of the tri-band signal is calculated as,

$$\begin{aligned}
a_{TB}^2(t) = \big(&I_1(t) + I_2(t)\cos(\Delta\omega_1 t+\theta_1) - Q_2(t)\sin(\Delta\omega_1 t+\theta_1) \\
&+ I_3(t)\cos(\Delta\omega_2 t+\theta_2) - Q_3(t)\sin(\Delta\omega_2 t+\theta_2)\big)^2 \\
&+ \big(Q_1(t) + Q_2(t)\cos(\Delta\omega_1 t+\theta_1) + I_2(t)\sin(\Delta\omega_1 t+\theta_1) \\
&+ Q_3(t)\cos(\Delta\omega_2 t+\theta_2) + I_3(t)\sin(\Delta\omega_2 t+\theta_2)\big)^2.
\end{aligned} \tag{5.6}$$

As is evident from (5.6), the envelope of the tri-band signal contains components at baseband, $\Delta\omega_1$, $\Delta\omega_2$, $\Delta\omega_1 - \Delta\omega_2$, and harmonics of $\Delta\omega_{1/2}$. The complete envelope of the tri-band signal, given in (5.6), cannot be employed to modulate the drain supply of the ET PA. Similar to the concurrent dual-band ET operation, we can calculate the LFC of the tri-band signal (i.e., the envelope of the envelope of the tri-band signal). Using (5.6), and after some simplifications, it can be shown that the LFC of the envelope of the tri-band signal, $a_{LF}(t)$ is calculated as,

$$\begin{aligned} a_{LF}(t) &= \sqrt{I_1^2(t)+Q_1^2(t)} + \sqrt{I_2^2(t)+Q_2^2(t)} + \sqrt{I_3^2(t)+Q_3^2(t)} \\ &= a_1(t)+a_2(t)+a_3(t). \end{aligned} \tag{5.7}$$

The bandwidth of $a_{LF}(t)$ is equal to the largest bandwidth of the individual envelope signals:

$$BW\left(a_{LF}(t)\right) = max\{BW\left(a_1(t)\right), BW\left(a_2(t)\right), BW\left(a_3(t)\right)\}, \tag{5.8}$$

The LFC of the envelope of the tri-band signal, a_{LF}, can be used to modulate the drain supply voltage of the tri-band PA. This will result in a similar bandwidth requirement for the envelope amplifier as that of a single-band ET PA, independent of the carrier spacings, $\Delta\omega_1$ and $\Delta\omega_2$.

Alternatively, the LFC of the envelope of the tri-band signal can be calculated as follows. The tri-band signal can be considered to be a dual-band signal as:

$$v_{TB}(t) = v_1(t) + (v_2(t)+v_3(t)) = v_1(t) + \hat{v}_2(t), \tag{5.9}$$

where,

$$\hat{v}_2(t) = v_2(t) + v_3(t). \tag{5.10}$$

From the analysis presented in Chapter 4, the LFC of the envelope of (5.9) is calculated as:

$$a_{LF}(t) = a_1(t) + \hat{a}_2(t) = a_1(t) + a_{DB,23}(t), \tag{5.11}$$

where $a_{DB,23}(t)$ is the complete envelope of the dual-band signal, $\hat{v}_2(t)$. Using the LFC of $a_{DB,23}$, (5.11) can be rewritten as,

$$a_{LF}(t) = a_1(t) + a_{LF,23}(t) = a_1(t)+a_2(t)+a_3(t). \tag{5.12}$$

Similarly, one can generalize this analysis to calculate the LFC of the envelope of a multi-band signal with N signals as,

$$a_{LF}(t) = a_1(t)+a_2(t)+...+a_N(t), \tag{5.13}$$

where $a_i(t)$ is the envelope of the signal in band i.

In order to validate the derivation, Figure 5.1 shows the envelope of the tri-band WCDMA/LTE $5\,MHz$/WCDMA signal, given in (5.6), and its LFC, a_{LF}, given in (5.7), when the carrier frequencies are at $2.1\,GHz$, $2.2\,GHz$ and $2.4\,GHz$, respectively. The individual single-band signals have a PAPR of $9.1\,dB$, $7.6\,dB$, and $7.4\,dB$, respectively, and the combined tri-band signal has a PAPR of $8.6\,dB$. As is evident from Figure 5.1, the bandwidth of $a_{LF}(t)$ is limited to the modulation bandwidth of the three signals, $5\,MHz$, whereas the bandwidth of $a_{TB}(t)$ is a function of the spacing of the three signals.

5.2.2 Efficiency and Linearity Analysis

Similar to the concurrent dual-band ET PA, employing the LFC of the envelope of the tri-band signal to modulate the drain supply voltage of a tri-band ET PA impacts the efficiency and linearity. The effect on the efficiency and linearity of the tri-band ET PA is very similar to the efficiency and linearity analysss presented in Sections 4.2.2 and 4.2.3 for concurrent dual-band ET PAs.

We can study the effect of tri-band ET operation on the efficiency of the ET PA by comparing the following two cases:

- Case I – tri-band ET PA where the drain supply voltage is modulated using a_{TB}, and
- Case II – tri-band ET PA where the drain supply voltage is modulated using a_{LF}.

The efficiency of the tri-band ET PA for the two cases is calculated as:

$$\eta_{TB}(P_{out}) = \frac{1}{a_{TB}(t)} \cdot \frac{k a_{TB}^2(t)}{V_{DD,max} I_{DD}(P_{out})}, \tag{5.14}$$

$$\eta_{LF}(P_{out}) = \frac{1}{a_{LF}(t)} \cdot \frac{k a_{TB}^2(t)}{V_{DD,max} I_{DD}(P_{out})} = \eta_{TB}(P_{out}) \cdot \frac{a_{TB}(t)}{a_{LF}(t)}, \tag{5.15}$$

where η_{TB} and η_{LF} are the efficiency of the ET PA for Case I and II, respectively. The average efficiency of the tri-band ET PA for Case I and II is calculated assuming the PA is driven with a

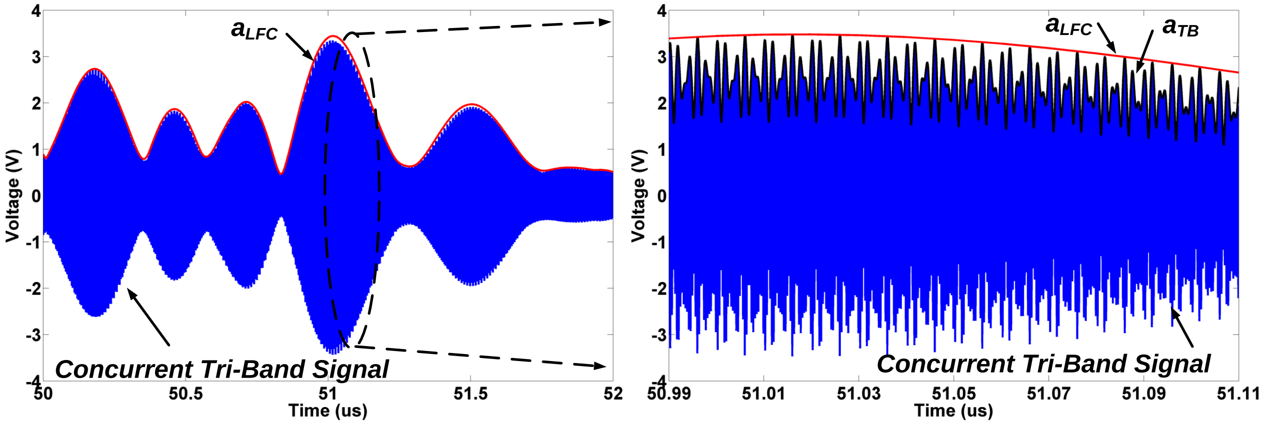

(a) Time domain envelope of the tri-band signal.

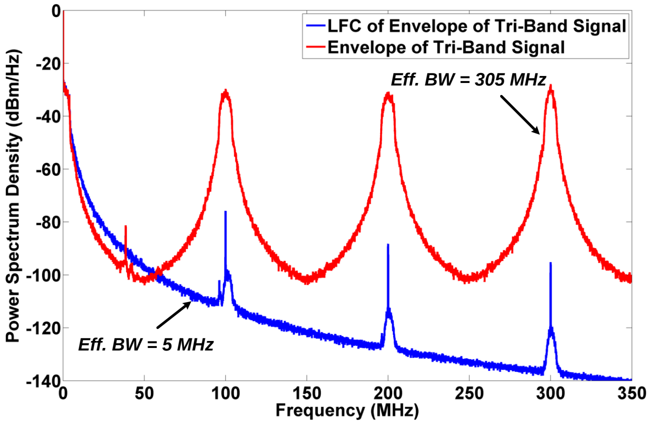

(b) Frequency domain envelope of the tri-band signal.

Figure 5.1: (a) Time domain and (b) frequency domain envelope of the tri-band signal and its low frequency component for a concurrent tri-band signal.

modulated signal as:

$$\eta_{avg,TB} = \frac{\displaystyle\int_0^1 ka_{TB}^2.PDF_{TB}(a_{TB})da_{TB}}{\displaystyle\int_0^1 \frac{ka_{TB}^2}{\eta_{TB}(ka_{TB}^2)}.PDF_{TB}(a_{TB})da_{TB}}, \tag{5.16}$$

$$\eta_{avg,LF} = \frac{\displaystyle\int_0^1 ka_{TB}^2.PDF_{TB}(a_{TB})da_{TB}}{\displaystyle\int_0^1\int_0^1 \frac{ka_{LF}a_{TB}}{\eta_{TB}(ka_{TB}^2)}.PDF_{LF}(a_{TB},a_{LF})da_{LF}da_{TB}}, \tag{5.17}$$

where $\eta_{avg,TB}$ and $\eta_{avg,LF}$ represent the average efficiency of the concurrent tri-band ET PA using $a_{TB}(t)$ and $a_{LF}(t)$, respectively. PDF_{TB} and PDF_{LF} represent the PDF of the complete envelope of the tri-band signal and its LFC, respectively. The efficiency contraction factor, γ_{CF}, can be defined as:

$$\gamma_{CF} = \frac{\eta_{avg,LF}}{\eta_{avg,TB}} = \frac{\displaystyle\int_0^1\int_0^1 a_{LF}\frac{ka_{TB}}{\eta_{TB}(ka_{TB}^2)}.PDF_{LF}(a_{TB},a_{LF})da_{LF}da_{TB}}{\displaystyle\int_0^1 \frac{ka_{TB}^2}{\eta_{TB}(ka_{TB}^2)}.PDF_{TB}(a_{TB})da_{TB}}. \tag{5.18}$$

The efficiency contraction factor strongly depends on the individual signal characteristics (e.g., PDF and PAPR), and efficiency profile of the PA, and is independent of the carrier spacings. Assuming a PA is biased in class-AB with a conduction angle of 200^o (where GaN PAs are typically biased in practice), an efficiency contraction factor of 88% is achieved for the tri-band WCDMA/LTE $5\,MHz$/WCMDA signal shown in Figure 5.1. This will typically result in efficiency loss of $5-6\%$ for the tri-band ET PA when $a_{LF}(t)$ is used to modulate instead of $a_{TB}(t)$. It should be noted that as the number of carriers increases, it is expected that γ_{CF} will degrade, given the multi-band signal has the same PAPR. This will limit the application of the proposed simplification to multi-band signals with more than three carriers due to significant reduction of the efficiency enhancement. This analysis will be further validated using simulation results for a tri-band $45\,W$ GaN ET PA in the next section.

Similar to the dual-band ET PA, the nonlinearity of the tri-band ET PA using $a_{LF}(t)$ will be intensified as the behavior of the PA changes with the drain supply voltage. As $a_{LF}(t)$ does not follow the instantaneous envelope of the tri-band signal, $a_{TB}(t)$, the PA may operate with different supply voltages while driven with the same input power at different times. As the behavior of the PA changes with the drain supply voltage, this will lead to stronger memory effects in tri-band ET PAs. The intensity of the memory effects is a strong function of the

Table 5.1: Simulation results of a 45 W GaN tri-band ET PA (excluding the losses of the envelope amplifier).

Technique	Avg. Efficiency	Avg. Power (dBm)	Gain (dB)	Env. BW (MHz)
Constant Supply PA	27.5%	38.9	14.3	–
LFC-Env ET PA	51.0%	38.9	10.6	5
TB-Env ET PA	57.0%	38.6	10.2	> 305

transistor technology and the nonlinearity profile of the transistor parasitics. Similar to the dual-band ET PA, it can be shown that in the case of GaN transistors, modulating the drain supply voltage with $a_{LF}(t)$ will results in more spread in AM/AM, while it will not affect the AM/PM spread.

5.2.3 Validation in Simulation

The efficiency analysis was validated by simulating a broadband class-B/J 45 W GaN PA [101] driven with a tri-band signal using Agilent's ADS RF and Ptolemy co-simulation. The 45 W GaN PA was operated from $1.9\,GHz - 2.9\,GHz$ with peak output power and efficiency of 45 dBm and 67%, respectively. The tri-band signal was composed of a WCDMA/LTE 5 MHz/WCDMA signals with center frequencies of 2.1 GHz, 2.2 GHz, and 2.4 GHz, respectively, for the following three cases:

- Case I – Constant supply 45 W GaN tri-band PA (no drain modulation),
- Case II – 45 W GaN tri-band ET PA using $a_{LF}(t)$,
- Case III– 45 W GaN tri-band ET PA using $a_{TDB}(t)$.

An ideal envelope amplifier without bandwidth limitation was used in the co-simulation and the PAs were not linearized. Note that the envelope amplifier required more than 305 MHz bandwidth for Case III. Table 5.1 summarizes the simulation results for the three cases. As is evident from the simulation results, the efficiency of the tri-band ET PA dropped by 6% as the result of using $a_{LF}(t)$ to modulate the drain supply voltage of the PA rather than $a_{TB}(t)$, corresponding to $\gamma_{CF} = 89.5\%$, which agrees with the calculated efficiency contraction factor.

5.3 Tri-Band ET PA Linearization

As discussed in Section 5.2.2, modulating the drain supply voltage in the tri-band ET PA using $a_{LF}(t)$ will result in added distortion, however, the PA cannot be linearized using tri-band DPD techniques available in the literature. In this section, the DPD model proposed for dual-band ET PAs will be generalized to linearize tri-band ET PAs. First, a brief review of the existing tri-band DPD models in the literature will be discussed; next, the proposed tri-band DPD model apropriate for use in tri-band ET PAs will be presented.

5.3.1 Linearization of Tri-Band PAs in Literature

While dual-band DPD models have been paid a lot of attention in recent publications for linearization of carrier aggregated signals, few works have investigated tri-band DPD models. In order to linearize tri-band PAs without excessive sampling frequency requirements, tri-band PAs are modeled and linearized as three-input, three-output nonlinear systems. The behavior of the tri-band PA is modeled as:

$$\tilde{y}_i(n) = \tilde{f}_i(\tilde{x}_1(n), \tilde{x}_2(n), \tilde{x}_3(n)), \tag{5.19}$$

where $\tilde{x}_i(n)$ and $\tilde{y}_i(n)$ are the BBE inputs and outputs of the tri-band PA for band i, respectively, and $\tilde{f}_i(.)$ is the describing function of the PA behavior around band i. Similar to dual-band DPD models, BBE inputs/outputs are sampled at up to five times the largest bandwidth of all the signals, independent of the three carrier frequencies. Different tri-band DPD models use different describing functions to model the behavior of the tri-band PA. For example, in [112], authors have generalized the 2D-DPD model for a tri-band PA (3D-DPD). The 3D-DPD model expresses the output in each band as a function of the inputs as:

$$\tilde{y}_i(n) = \sum_{m=0}^{M-1} \sum_{k=0}^{N-1} \sum_{l=0}^{k+l} \sum_{j=0}^{l} a_{klm}^{(i)} \tilde{x}_i(n-m) |\tilde{x}_1(n-m)|^{(k-l-j)} |\tilde{x}_2(n-m)|^l \tilde{x}_3(n-m)|^j, \tag{5.20}$$

where $a_{mklj}^{(i)}$ are the model coefficients for band i, and N and M denote the nonlinearity order and memory depth, respectively. The 3D-DPD model shows good linearization capacity, however, the model requires a large of number of coefficients as the nonlinearity order and/or memory depth increases. Furthermore, the 3D-DPD is not capable of linearizing tri-band ET PAs. Another example of a tri-band DPD model is presented in [107], where the authors have extended their work on 2D-CR-GMP to three-input, three-output systems. The tri-band CR-GMP (3D-CR-GMP) model achieves similar linearization performance to 3D-DPD with a smaller number of coefficients. The model, however, has only been tested for constant supply and Doherty PAs and is not capable of linearizing tri-band ET PAs. The 3D-CR-GMP has the general form of:

$$\begin{aligned}
\tilde{y}_i(n) = &\sum_{\substack{k=1\\ odd}}^{2N_i-1} \sum_{\substack{r=0\\ even}}^{k} \sum_{\substack{t=0\\ even}}^{r} \phi \tilde{x}_i(n)|\tilde{x}_1(n)|^{k-r-1}|\tilde{x}_2(n)|^{r-t}|\tilde{x}_3(n)|^{t} \\
&+ \sum_{\substack{k=2\\ even}}^{N_i} \sum_{\substack{q=2\\ even}}^{\hat{N}-1} \sum_{\substack{r=0\\ even}}^{q} \sum_{\substack{s=0\\ even}}^{k-1} \sum_{\substack{t=0\\ even}}^{r} \sum_{\substack{u=0\\ even}}^{s} \sum_{j=1}^{M(m_1)} \Big(\alpha \tilde{x}_i(n)|\tilde{x}_1(n)|^{k-s-2}|\tilde{x}_2(n)|^{s-u}|\tilde{x}_3(n)|^{u}|\tilde{x}_1(n-j)|^{q-r} \\
&\times |\tilde{x}_2(n-j)|^{r-t}|\tilde{x}_3(n-j)|^{t}\Big) \\
&+ \sum_{\substack{k=1\\ odd}}^{N_i} \sum_{\substack{q=1\\ odd}}^{\hat{N}-1} \sum_{\substack{r=0\\ even}}^{q} \sum_{\substack{s=0\\ even}}^{k-1} \sum_{\substack{t=0\\ even}}^{r} \sum_{\substack{u=0\\ even}}^{s} \sum_{j=1}^{M(m_2)} \Big(\beta \tilde{x}_i(n-j)|\tilde{x}_1(n)|^{k-s-1}|\tilde{x}_2(n)|^{s-u}|\tilde{x}_3(n)|^{u}|\tilde{x}_1(n-j)|^{q-r-1} \\
&\times |\tilde{x}_2(n-j)|^{r-t}|\tilde{x}_3(n-j)|^{t}\Big),
\end{aligned} \tag{5.21}$$

where ϕ, α, and β are the model coefficients, and,

$$\begin{aligned}
\hat{N} &= \max(N_1, N_2, N_3), \\
m_1 &= \frac{1}{2}\Big(1 + (k-s-2) + (s-u) + u + (q-r) + (r-t) + t) + 1\Big), \\
m_2 &= \frac{1}{2}\Big(1 + (k-s-1) + (s-u) + u + (q-r-1) + (r-t) + t) + 1\Big).
\end{aligned} \tag{5.22}$$

In this thesis a tri-band DPD model based on 3D-CR-GMP, suitable for the linearization of tri-band ET PAs will be presented.

5.3.2 Proposed Tri-band DPD for ET PAs

Similar to the dual-band DPD for dual-band ET PAs, the tri-band DPD model is augmented to capture the dependency on the drain supply modulation. The tri-band DPD model for tri-band ET PAs can be written as:

$$\tilde{y}_i(n) = \tilde{f}_i(\tilde{x}_1(n), \tilde{x}_2(n), \tilde{x}_3(n)) \times f_{Ei}(V_{DD}(n)), \tag{5.23}$$

where $\tilde{x}_i(n)$ denotes the BBE input signal for band i, and $V_{DD}(n)$ is the voltage used to modulate the drain supply. $\tilde{f}_i(.)$ is the tri-band PA describing function without supply modulation for band i, and $f_{Ei}(.)$ describes the dependency of the dual-band PA on the supply voltage for band

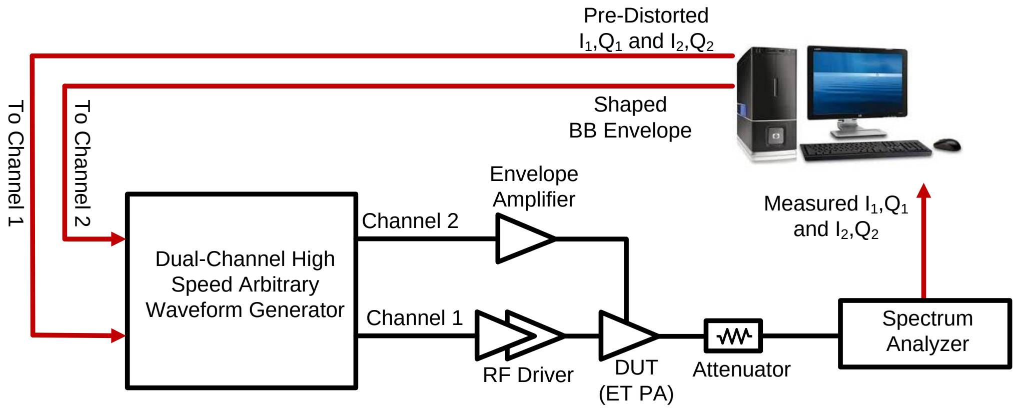

Figure 5.2: Measurement setup for the dual-band ET PA.

i. We can use different describing functions for the constant supply tri-band PA; in this thesis, $f_i(.)$ is expressed as given in (5.21). Furthermore, the supply dependency is approximated using a polynomial function. Since the drain supply voltage is controlled using a shaped version of $a_{LF}(t)$, we can rewrite (5.24) as:

$$\tilde{y}_i(n) = f_i(\tilde{x}_1,\tilde{x}_2,\tilde{x}_3) \times \sum_{l=0}^{N_S-1} \left(c_l^{(i)} \left(|\tilde{x}_1(n)| + |\tilde{x}_2(n)| + |\tilde{x}_3(n)|\right)^l \right), \tag{5.24}$$

where N_S is the nonlinearity order for the supply effect and c_l^i are the model coefficients for band i. The model coefficients are identified using an LSE estimator.

5.4 Tri-Band ET PA Measurement Results

The proposed tri-band ET PA was evaluated using the measurement setup shown in Figure 5.2. The setup consisted of a dual-channel high speed ($8\,GS/s$) arbitrary waveform generator (AWG), a vector signal analyzer, and an RF driver. The high speed AWG generates both the tri-band RF signal and the envelope signal. The DPD model coefficients were identified and applied using a PC running MATLAB®.

In order to validate the effectiveness of the proposed tri-band ET PA operation, a tri-band ET PA prototype was measured. The prototype consisted of a $45\,W$ broadband class B/J GaN PA (presented in [101]) and a linear-assisted switched mode envelope amplifier (the same as

Prototype II in Section 4.5). The PA was operated from $1.9-2.9\,GHz$ with measured peak output power and efficiency of $45\,dBm$ and 67%, respectively, when operated from a constant $28\,V$ drain supply voltage.

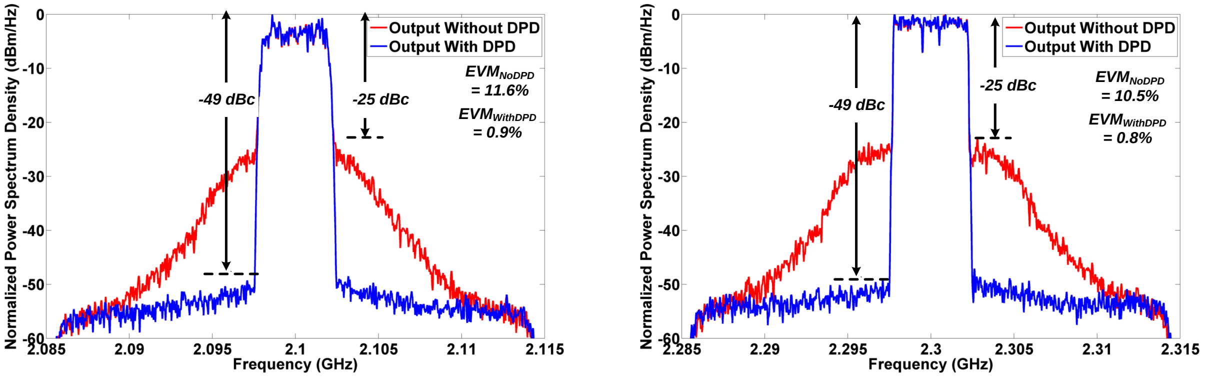

(a) Band 1 – WCDMA

(b) Band 2 – LTE $5\,MHz$

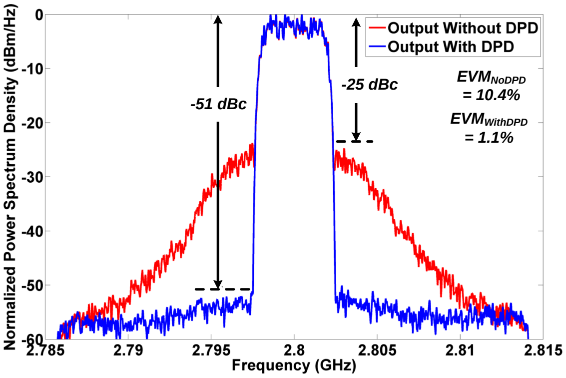

(c) Band 3 – WCDMA

Figure 5.3: Measured spectrum of the tri-band ET PA (WCMDA band at $2.1\,GHz$, LTE $5\,MHz$ band at $2.3\,GHz$ and WCMDA band at $2.8\,GHz$) with and without DPD.

The tri-band $45\,W$ GaN PA was measured in both constant supply and ET modes of operation. The tri-band ET PA was successfully linearized when driven with a tri-band WCDMA/LTE $5\,MHz$/WCDMA signal using the proposed 3D-DR-GMP with supply dependency, with $N=5$, $M=2$, and $N_S=3$, for a total of 63 coefficients per band. Figure 5.3 shows the measured spectrum of the tri-band ET PA output before and after linearization when the carriers were at $2.1\,GHz$, $2.3\,GHz$, and $2.8\,GHz$, respectively. The tri-band ET PA achieved 38% overall effi-

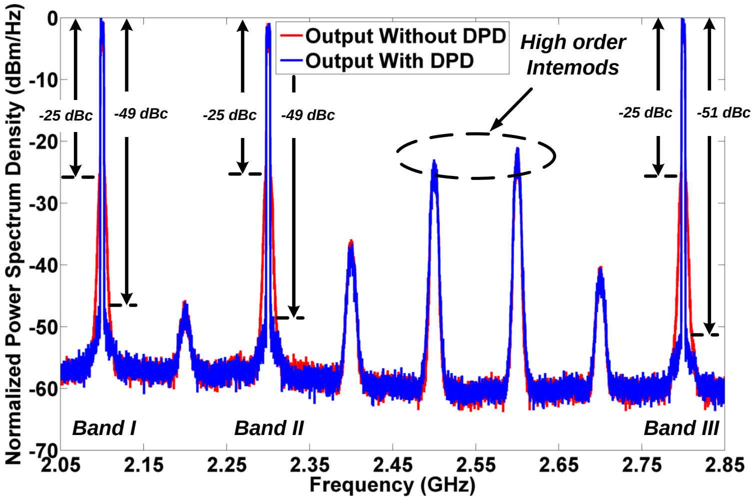

Figure 5.4: Measured spectrum of the output of the tri-band ET PA before and after linearization.

ciency (estimated 54% efficiency for the PA excluding the losses in the envelope amplifier) at 37.1 *dBm* average output power, showing 10% efficiency improvement over the constant supply PA. Table 5.2 summarizes the measurement results of the tri-band ET PA. Figure 5.4 shows the measured spectrum of the tri-band ET PA before and after linearization over a wide frequency range. In the case of tri-band signals, the number of out-of-band intermodulation distortions increases, which will result in more stringent requirements for the filter after the PA. Note that this issue exists in both constant supply and supply modulated PAs.

Table 5.2: Summary of the tri-band ET PA measurement results.

	Band 1		**Band 2**		**Band 3**		**Concurrent tri-band**	
Parameter	**Without DPD**	**With DPD**	**Without DPD**	**With DPD**	**Without DPD**	**With DPD**	**Without DPD**	**With DPD**
ACPR (dBc)	−28.5	−48.5	−27.7	−49.7	−28.8	−51.0	–	–
EVM (%)	11.61	0.95	10.55	0.83	10.46	1.15	–	–
PAPR (dB)	9.71	8.54	8.54	7.15	8.28	7.07	7.50	8.02
NMSE (dB)	−41.70		−43.18		−43.18		–	–
# of coeff.	63		63		63		189	

5.5 Conclusion

In this chapter, the principle of dual-band ET operation, presented in Chapter 4, was extended to multi-band ET operation. Similar to dual-band ET operation, multi-band ET operation will not pose additional bandwidth/linearity requirements on the envelope amplifier compared to a single-band ET PA. As the number of component carriers increases, the efficiency degradation associated with the elimination of the high frequency components of the multi-band signal envelop may be significant. In this work the number of component carriers was limited three as this is more plausible deployment scenario in the practice. In fact a significant increase in the number of component carriers will also induce further additional complexity at the system level too. The principle was validated using the measurement results of a tri-band $45\,W$ GaN ET PA. The tri-band ET PA showed 10% efficiency enhancement compared to a constant supply voltage tri-band PA. The efficiency of the tri-band ET PA was limited by the relatively limited efficiency of the envelope amplifier of 70%. Furthermore, a new tri-band DPD model with supply dependency, based on 3D-CR-GMP, was presented in this chapter to linearize the tri-band ET PA.

Chapter 6

Conclusion

The ever increasing demand for high data-rate wireless communication links has resulted in communication signals with high PAPR, wide modulation bandwidth and stringent linearity requirements. Future wireless communication standards will require designers to employ carrier aggregation techniques to increase the effective modulation bandwidth of the signal, by deploying multiple frequency compounds to deploy a wider bandwidth. Thus, future PAs (and transmitters) will be required to concurrently amplify multi-band signals with high PAPR, while maintaining good efficiency and linearity. This thesis began by reviewing the existing efficiency enhancement techniques from the literature and evaluating their compatibility with concurrent multi-band operation. The literature review revealed ET technique as an attractive efficiency enhancement technique for both base station and mobile PAs. However, concurrent amplification of multi-band signals using ET technique has not been shown in the literature. The main aim of this thesis was to propose and develop an ET PA capable of concurrent amplification of multi-band signals while achieving good efficiency and linearity, targeting inter-band and intra-band non-contiguous scenarios for carrier aggregated signals. The thesis was focused on implementation of such an amplifier for base station infrastructures; however, this work can be applied to mobile PAs as well.

As the first step, the sources of nonlinearity in single-band and dual-band PAs were investigated from a circuit perspective. Note that when developing a multi-band ET PA, it is important to ensure that the sources of nonlinearity and memory effects in the PA itself are minimized. Using the study of sources of nonlinearity, a design methodology was developed to reduce the memory effects in GaN PAs from the circuit design stage. A 45 W broadband GaN PA was designed to validate the study of sources of nonlinearity and reduce the sources of memory effects. The 45 W GaN PA was linearized to meet the EVM and spectrum mask requirements using simple memoryless polynomial DPD, when driven with different single-band and dual-band signals.

This analysis and design to reduce the sources of memory effects in PAs is essential as we move toward smaller cell sizes for base station infrastructure, such as femto- and pico-cells.

Next, the principle of concurrent dual-band ET operation using the LFC of the envelope of the dual-band signal was presented. In the literature, concurrent dual-band operation of ET PAs has not been shown, mainly due to the bandwidth limitations of the envelope amplifier. In this thesis, concurrent dual-band operation of ET PAs using the LFC of the envelope of the dual-band signal was proposed. To the best of our knowledge, concurrent dual-band operation of ET PAs using the LFC of the envelope of the dual-band signal was shown for the first time through this work using measurement results of several GaN ET PAs with different power levels and center frequencies. The dual-band ET PA was linearized using the proposed dual-band DPD model with supply dependency.

Lastly, the principle of concurrent dual-band ET operation was extended to multi-band signals using the LFC of the envelope of the multi-band signals. The proposed multi-band ET operation was validated using the measurement results from a tri-band ET PA. To the best of our knowledge, this was the first time in literature that tri-band ET operation was proposed and validated. The tri-band ET PA was linearized using the proposed tri-band DPD model with supply dependency.

6.1 Summary of Contributions

The key goal of this thesis was to develop concurrent amplification of multi-band signals using ET PAs for inter-band and intra-band non-contiguous carrier aggregated signals. This goal was achieved through the following key contributions:

(a) A detailed study of sources of memory effects in single- and dual-band PAs was presented. Based on the study, design methodology was devised to reduce the sources of memory effects in PAs from the circuit design stage and improve their linearizability.

(b) The principle of concurrent dual-band and tri-band ET operation using the LFC of the envelope of the dual-band and tri-band signal was proposed. This enabled ET PAs to amplify non-contiguous intra-band and inter-band carrier aggregated signals without posing extra bandwidth requirements on the envelope amplifier.

(c) A new dual-band and tri-band DPD model with supply dependency was proposed to linearize concurrent dual-band ET PAs.

6.2 Future Work

The work presented in thesis can be extended through further research into the mitigation of the limitations of the proposed techniques, also, by investigation of the applicability of these techniques for different technologies and applications.

The focus of this thesis was on multi-band ET PAs for base station transmitters. It would be interesting to research the suitability of the proposed multi-band ET PA for small base station cells (e.g., femto- and pico-cells) and integrated mobile transmitters. These applications have less stringent linearity requirement compared to what was discussed in this thesis, however, complicated DPD models (such as the DPD models proposed in this thesis) cannot be applied due to the power overhead of the linearization.

Another interesting topic for future research would be the extension the modulation bandwidth of the ET PA. This will require improving the bandwidth and slew-rate of the envelope amplifier. Furthermore, as the modulation bandwidth increases, the effects of ground noise, trapping effects and the envelope amplifier and PA interface become more significant.

Lastly, it would be worthwhile to investigate the integration of the complete ET PA into one or two IC processes. This would make the ET PA system suitable for mobile and hand-held devices. Note that the interface between the envelope amplifier and the PA plays a critical role in terms of achieving good efficiency and linearity. Further research into the interface of the envelope amplifier and the PA will be crucial for successful implementation of a fully integrated ET PA system.

6.3 List of Publications

Patents

1. **H. Sarbishaei**, Y. Hu, and S. Boumaiza, ”Dual-Band Signal Transmission,” U.S. Provisional Patent 61/946, 315, February 28, 2014.

Journal Papers

1. **H. Sarbishaei**, Y. Hu, B. Fehri, and S. Boumaiza, ”Concurrent Multi-Band Signal Transmission Using Envelope Tracking Power Amplifiers,” submitted to *IEEE Transactions on Circuits and Systems - Part I*, August 2014. (Based on Chapter 4 and 5)

2. **H. Sarbishaei**, B. Fehri, Y. Hu, and S. Boumaiza, ”Dual-band Volterra series digital predistortion for envelope tracking power amplifiers,” *IEEE Microwave and Wireless Components Letters*, vol. 24, no. 6, pp. 430-432, June 2014. (Based on Chapter 4)

Conference Papers

1. **H. Sarbishaei**, Y. Hu, B. Fehri, and S. Boumaiza, ”Concurrent Dual-Band Envelope Tracking Power Amplifier for Carrier Aggregated Systems,” in *IEEE MTT-S International Microwave Symposium Digest*, Tampa Bay, FL, June 2014. (Based on Chapter 4)

2. M. Naseri Ali Abadi, H. Golestaneh, **H. Sarbishaei**, and S. Boumaiza, ”An Extended Bandwidth Doherty Power Amplifier Using a Novel Output Combiner,” in *IEEE MTT-S International Microwave Symposium Digest*, Tampa Bay, FL, June 2014.

3. A. Khan, **H. Sarbishaei**, and S. Boumaiza, ”High Efficiency Two-Stage GaN Power Amplifier With Improved Linearity,” in *IEEE Tropical Conference on Power Amplifiers for Wireless and Radio Applications (PAWR)*, Newport Beach, CA, January 2014.

4. **H. Sarbishaei**, D. Y. Wu, and S. Boumaiza, ”Linearity of GaN HEMT RF Power Amplifiers A Circuit Perspective,” in *IEEE MTT-S International Microwave Symposium Digest*, Montreal, QC, June 2012. (Based on Chapter 3)

5. **H. Sarbishaei**, and S. Boumaiza, ”Switched-Mode Power Amplifier for Digital RF Transmitters,” presented in *IEEE Topical Symposium on Power Amplifiers for Wireless Communication*, Tempe, AZ, November 2011.

APPENDICES

Appendix A

Effect of Nonlinear Input Capacitance on AM/PM

The effect of nonlinear input capacitance on AM/AM and AM/PM of can be modeled by analyzing the input section of the equivalent model of the power amplifier shown in Figure A.1. The input side can be modeled using a low pass filter $Z_S(\omega_0) - C_{IN}$. We assume input signal is a single tone at ω_0 with the time-domain voltages and currents expressed as,

$$\begin{aligned} v_s(t) &= V_S \cos(\omega_0 t), \\ v_{gs}(t) &= V_0 + V_1 \cos(\omega_0 t + \phi_1) + V_2 \cos(2\omega_0 t + \phi_2) + V_3 \cos(3\omega_0 t + \phi_3) + \ldots, \\ i_{gs}(t) &= I_0 + I_1 \cos(\omega_0 t + \theta_1) + I_2 \cos(2\omega_0 t + \theta_2) + I_3 \cos(3\omega_0 t + \theta_3) + \ldots. \end{aligned} \tag{A.1}$$

Using the input capacitance C-V characteristics (for simplicity, assumed to be a polynomial function), the gate current is calculated as,

$$i_{gs}(t) = C_{gs}\left(v_{gs}(t)\right) \frac{dv_{gs}(t)}{dt} = C_0 \frac{dv_{gs}(t)}{dt} + C_1 v_{gs}(t) \frac{dv_{gs}(t)}{dt} + C_2 v_{gs}^2(t) \frac{dv_{gs}(t)}{dt} + \ldots. \tag{A.2}$$

Similarly, the gate current is defined using the source impedance as,

$$i_{gs}(t) = \left(v_s(t) - v_{gs}(t)\right) \otimes \mathcal{F}^{-1}\left(Y_S(\omega_0)\right). \tag{A.3}$$

For simplicity of analysis we use phasor notation, only taking the first three harmonics into account. Thus, the current and voltages are rewritten using phasor notation as,

$$\begin{aligned} V_s(\omega) &= [0, V_S, 0, 0], \\ V_{gs}(\omega) &= \left[V_0, V_1 e^{j\phi_1}, V_2 e^{j\phi_2}, V_3 e^{j\phi_3}\right], \\ I_{gs}(\omega) &= \left[0, I_1 e^{j\theta_1}, I_2 e^{j\theta_2}, I_3 e^{j\theta_3}\right], \end{aligned} \tag{A.4}$$

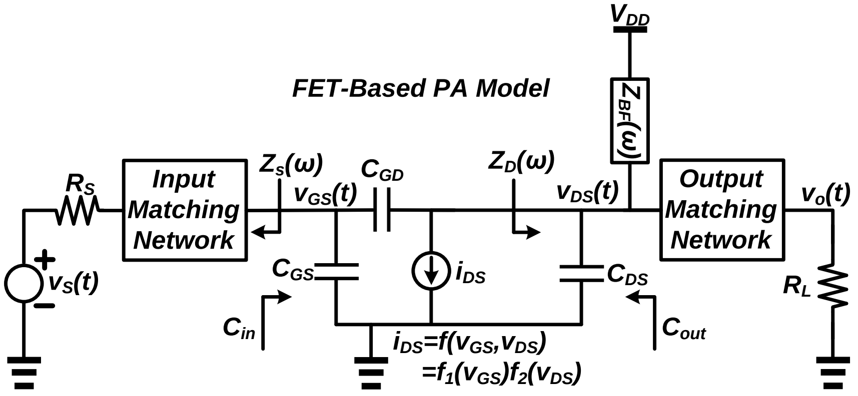

Figure A.1: Generic model for analyzing memory effect in power amplifiers.

where the time-domain signals are calculated using phasor notation as,

$$
\begin{aligned}
v_s(t) &= Re\left[V_S e^{j\omega_0 t}\right], \\
v_{gs}(t) &= Re\left[V_0 + V_1 e^{j\omega_0 t+\phi_1} + V_2 e^{j2\omega_0 t+\phi_2} + V_3 e^{j3\omega_0 t+\phi_3}\right], \\
i_{gs}(t) &= Re\left[I_1 e^{j\omega_0 t+\theta_1} + I_2 e^{j2\omega_0 t+\theta_2} + I_3 e^{j3\omega_0 t+\theta_3}\right].
\end{aligned}
\tag{A.5}
$$

In order to simplify the analytical solution, we assume the source impedance, $Z_S(\omega)$, is short circuited at harmonics, i.e. $V_2 = V_3 = 0$. Using (A.2) and phasor notation, we have,

$$
\begin{aligned}
I_{gs}(\omega) = {} & C_0 j\omega V_{gs}(\omega) + C_1 V_{gs}(\omega) \otimes (j\omega V_{gs}(\omega)) \\
& + C_2 V_{gs}(\omega) \otimes (j\omega V_{gs}(\omega)) \otimes (j\omega V_{gs}(\omega)).
\end{aligned}
\tag{A.6}
$$

Equating phasors for fundamental and harmonics on either side of (A.6), we have,

$$
\begin{aligned}
I_{gs}(\omega_0) &= C_0 j\omega_0 V_1 e^{j\phi_1} + C_1 j\omega_0 V_0 V_1 e^{j\phi_1} + C_2\left(j\omega_0 V_0^2 V_1 e^{j\phi_1} + 0.5 j\omega_0 V_1^3 e^{j\phi_1}\right), \\
I_{gs}(2\omega_0) &= C_0 j2\omega_0 V_2 c^{j\phi_2} + C_1 j\omega_0 V_1^2 e^{j2\phi_1} + C_2 j\omega_0^2 V_0 V_1^2 ec^{j\phi_1}.
\end{aligned}
\tag{A.7}
$$

We can also find the gate current phasors using (A.3) as,

$$\begin{aligned}
I_{gs}(\omega) &= (V_s(\omega) - V_{gs}(\omega))\, Y_s(\omega), \Rightarrow \\
I_{gs}(\omega_0) &= (V_s(\omega_0) - V_{gs}(\omega_0))\, Y_s(\omega_0) = \left(V_S - V_1 e^{j\phi_1}\right) Y_s(\omega_0), \\
I_{gs}(2\omega_0) &= (V_s(2\omega_0) - V_{gs}(2\omega_0))\, Y_s(2\omega_0) = \left(-V_2 e^{j\phi_2}\right) Y_s(2\omega_0), \\
I_{gs}(3\omega_0) &= (V_s(3\omega_0) - V_{gs}(3\omega_0))\, Y_s(3\omega_0) = \left(-V_3 e^{j\phi_3}\right) Y_s(3\omega_0).
\end{aligned} \tag{A.8}$$

Using (A.7) and (A.8), we get,

$$\begin{aligned}
\left(V_S - V_1 e^{j\phi_1}\right) Y_s(\omega_0) = C_0 j\omega_0 V_1 e^{j\phi_1} + C_1 j\omega_0 V_0 V_1 e^{j\phi_1} \\
+ C_2 \left(j\omega_0 V_0^2 V_1 e^{j\phi_1} + 0.5 j\omega_0 V_1^3 e^{j\phi_1}\right).
\end{aligned} \tag{A.9}$$

By solving (A.9), we can find the fundamental phasor of the gate voltage, V_1, as a function of input source, V_S, and the gate's DC bias voltage, V_0. It is evident that (A.9) is a nonlinear function with respect to V_1 which results in a nonlinear gate voltage with respect to input source. Hence, both AM/AM and AM/PM of the power amplifier will be affected due to existence of nonlinear input capacitance. The fundamental phasor of the gate voltage can be derived by rearranging (A.9) as,

$$V_1 e^{j\phi_1} = \frac{V_S Y_s(\omega_0)}{Y_s(\omega_0) + C_0 j\omega_0 + C_1 j\omega_0 V_0 + C_2 j\omega_0 V_0^2 + 0.5 C_2 j\omega_0 V_1^2}, \tag{A.10}$$

Thus, the amplitude and phase of gate voltage are determined as,

$$\begin{aligned}
V_1 &= V_S \sqrt{\frac{G_s^2(\omega_0) + B_s^2(\omega_0)}{G_s^2(\omega_0) + \left(B_s(\omega_0) + \omega_0\left(C_0 + C_1 V_0 + C_2 V_0^2 + 0.5 C_2 V_1^2\right)\right)^2}}, \\
\phi_1 &= \tan^{-1}\left(\frac{B_s(\omega_0)}{G_s(\omega_0)}\right) \\
&\quad - \tan^{-1}\left(\frac{\left(B_s(\omega_0) + \omega_0\left(C_0 + C_1 V_0 + C_2 V_0^2 + 0.5 C_2 V_1^2\right)\right)}{G_s(\omega_0)}\right),
\end{aligned} \tag{A.11}$$

where $Y_s(\omega_0) = G_s(\omega_0) + jB_s(\omega_0)$. Note that both phase and magnitude are nonlinear functions of input source. We can simplify (A.11) further assuming the source impedance is chosen to resonate out the input capacitance for maximum gain, i.e.,

$$B_s(\omega_0) = -\omega_0\left(C_0 + C_1 V_0 + C_2 V_0^2 + 0.5 C_2 V_1^2\right). \tag{A.12}$$

Replacing (A.12) in (A.11), results in,

$$V_1 = V_S \sqrt{\frac{G_s^2(\omega_0) + B_s^2(\omega_0)}{G_s^2(\omega_0) + \left(0.5\omega_0 C_2 V_1^2\right)^2}},$$
$$\phi_1 = \tan^{-1}\left(\frac{B_s(\omega_0)}{G_s(\omega_0)}\right) - \tan^{-1}\left(\frac{0.5\omega_0 C_2 V_1^2}{G_s(\omega_0)}\right). \tag{A.13}$$

It should be noted that it is not possible to resonate out the term $0.5\omega_0 C_2 V_1^2$, as it is input dependent. In the case where $C_2 \ll C_0, C_1$, we can simplify V_1 using $G_s(\omega_0) \gg 0.5\omega_0 C_2 V_1^2$ as,

$$V_1 \simeq V_S \sqrt{\frac{G_s^2(\omega_0) + B_s^2(\omega_0)}{G_s^2(\omega_0)}}. \tag{A.14}$$

Note that due to nature of $\tan^{-1}()$ function we can not use the same approximation for the phase calculation. Replacing (A.14) in (A.13), we get,

$$\begin{aligned}\phi_1 &= \tan^{-1}\left(\frac{B_s(\omega_0)}{G_s(\omega_0)}\right) - \tan^{-1}\left(\frac{0.5\omega_0 C_2 V_1^2}{G_s(\omega_0)}\right)\\ &\simeq \tan^{-1}\left(\frac{B_s(\omega_0)}{G_s(\omega_0)}\right) - \tan^{-1}\left(\frac{0.5\omega_0 C_2 V_s^2 (G_s^2(\omega_0) + B_s^2(\omega_0))}{G_s(\omega_0)}\right),\end{aligned} \tag{A.15}$$

which gives approximately, the input dependency of the output phase, i.e. AM/PM.

References

[1] W. H. Doherty, “A new high efficiency power amplifier for modulated waves,” *Proceedings of the Institute of Radio Engineers*, vol. 24, pp. 1163–1182, Sep. 1936.

[2] F. Wang, A. H. Yang, D. F. K. L. E. Larson, and P. M. Asbeck, “Design of wide-bandwidth envelope-tracking power amplifiers for OFDM applications,” *IEEE Transactions on Microwave Theory and Techniques*, vol. 53, no. 4, pp. 1244–1255, Apr. 2005.

[3] L. R. Kahn, “Single-sideband transmission by envelope elimination and restoration,” *Proceedings of the IRE*, vol. 40, no. 7, pp. 803–806, Jul. 1952.

[4] S. C. Cripps, *RF Power Amplifiers for Wireless Communications*, 2nd ed. Artech House, 2006.

[5] D. Y.-T. Wu and S. Boumaiza, “A modified Doherty confguration for broadband amplifcation using symmetrical devices,” *IEEE Transactions on Microwave Theory and Techniques*, vol. 60, no. 10, pp. 3201–3213, Oct. 2012.

[6] H. Golestaneh, F. A. Malekzadeh, and S. Boumaiza, “An extended-bandwidth three-way Doherty power amplifer,” *IEEE Transactions on Microwave Theory and Techniques*, vol. 61, no. 9, pp. 3318 – 3328, Sep. 2013.

[7] D. Gustafsson, J. C. Cahuana, R. Hellberg, and C. Fager, “A 13-GHz digitally controlled dual-RF input power-amplifier design based on a Doherty-Outphasing continuum analysis,” *IEEE Transactions on Microwave Theory and Techniques*, vol. 61, no. 10, pp. 3743 – 3752, Oct. 2013.

[8] D. Kang, J. Choi, D. Kim, and B. Kim, “Design of Doherty power amplifers for handset applications,” *IEEE Transactions on Microwave Theory and Techniques*, vol. 58, no. 8, pp. 2134–2142, Aug. 2010.

[9] D. Kang, D. Kim, Y. Cho, B. Park, J. Kim, and B. Kim, "Design of bandwidth-enhanced Doherty power amplifiers for handset applications," *IEEE Transactions on Microwave Theory and Techniques*, vol. 59, no. 12, pp. 3474–3482, Dec. 2011.

[10] J. H. Qureshi, N. Li, W. C. E. Neo, F. Rijs, I. Blednov, and L. C. N. de Vreede, "A wide-band 20W LMOS Doherty power amplifier," in *IEEE MTT-S International Microwave Symposium Digest*, Anaheim, CA, May 2010, pp. 1504 – 1507.

[11] W. Chen, S. A. Bassam, X. Li, Y. Liu, K. Rawat, M. Helaoui, F. M. Ghannouchi, and Z. Feng, "Design and linearization of concurrent dual-band Doherty power amplifer with frequency-dependent power ranges," *IEEE Transactions on Microwave Theory and Techniques*, vol. 59, no. 10, pp. 2537–2546, Oct. 2011.

[12] W. Chen, S. Zhang, Y. Liu, Y. Liu, and F. M. Ghannouchi, "A concurrent dual-band uneven Doherty power amplifier with frequency-dependent input power division," *IEEE Transactions on Circuits and Systems I: Regular Papers*, vol. 61, no. 2, pp. 552–561, Feb. 2014.

[13] D. Gustafsson, C. M. Andersson, and C. Fager, "A modified Doherty power amplifier with extended bandwidth and reconfigurable efficiency," *IEEE Transactions on Microwave Theory and Techniques*, vol. 61, no. 1, pp. 533 – 542, Jan. 2013.

[14] R. Darraji, F. M. Ghannouchi, and M. Helaoui, "Mitigation of bandwidth limitation in wireless Doherty amplifiers with substantial bandwidth enhancement using digital techniques," *IEEE Transactions on Microwave Theory and Techniques*, vol. 60, no. 9, p. 28752884, Sep. 2012.

[15] D. Wu and S. Boumaiza, "A mixed-technology asymmetrically biased extended and reconfgurable Doherty amplifer with improved power utilization factor," *IEEE Transactions on Microwave Theory and Techniques*, vol. 61, no. 5, pp. 1946–1956, May 2013.

[16] M. N. A. Abadi, H. Golestaneh, H. Sarbishaei, and S. Boumaiza, "An extended bandwidth Doherty power amplifier using a novel output combiner," in *IEEE MTT-S International Microwave Symposium Digest*, Tampa Bay, FL, Jun. 2014.

[17] K. Bathich, A. Z. Markos, and G. Boeck, "Frequency response analysis and bandwidth extension of the doherty amplifer," *IEEE Transactions on Microwave Theory and Techniques*, vol. 59, no. 4, pp. 934–944, Apr. 2011.

[18] R. B. Staszewski, J. L.Wallberg, S. Rezeq, C.-M. Hung, O. E. Eliezer, S. K. Vemulapalli, C. Fernando, K. Maggio, R. Staszewski, N. Barton, M.-C. Lee, P. Cruise, M. Entezari,

K. Muhammad, and D. Leipold, “All-digital PLL and transmitter for mobile phones,” *IEEE Journal of Solid-State Circuits*, vol. 40, no. 12, pp. 2469–2482, Dec. 2005.

[19] R. Staszewski, R. B. Staszewski, T. Jung, T. Murphy, I. Bashir, O. Eliezer, K. Muhammad, and M. Entezari, “Software assisted digital RF processor (DRP) for single-chip GSM radio in 90 nm CMOS,” *IEEE Journal of Solid-State Circuits*, vol. 45, no. 2, pp. 276–288, Feb. 2010.

[20] H. Darabi, H. Jensen, and A. Zolfaghari, “Analysis and design of small-signal polar transmitters for cellular applications,” *IEEE Journal of Solid-State Circuits*, vol. 46, no. 6, pp. 1237–1249, Jun. 2011.

[21] P. Reynaert and M. S. J. Steyaert, “A 1.75-GHz polar modulated CMOS RF power amplifier for GSM-EDGE,” *IEEE Journal of Solid-State Circuits*, vol. 40, no. 12, pp. 2598–2608, Dec. 2005.

[22] J. N. Kitchen, I. Deligoz, S. Kiaei, and B. Bakkaloglu, “Polar SiGe class E and F amplifiers using switch-mode supply modulation,” *IEEE Transactions on Microwave Theory and Techniques*, vol. 55, no. 5, pp. 845–856, May 2007.

[23] W.-Y. Chu, B. Bakkaloglu, and S. Kiaei, “A 10 MHz bandwidth, 2 mV ripple PA regulator for CDMA transmitters,” *IEEE Journal of Solid-State Circuits*, vol. 43, no. 12, pp. 2809–2819, Dec. 2008.

[24] J. S. Walling, S. S. Taylor, and D. J. Allstot, “A class-G supply modulator and class-E PA in 130 nm CMOS,” *IEEE Journal of Solid-State Circuits*, vol. 44, no. 9, pp. 2339–2347, Sep. 2009.

[25] T. Nakatani, J. Rode, D. F. Kimball, L. E. Larson, and P. M. Asbeck, “Digital polar transmitter using a watt-class current-mode class-D CMOS power amplifier,” in *IEEE Radio Frequency Integrated Circuits Symposium (RFIC), 2011*, 2011.

[26] J. Choi, J. Yim, J. Yang, J. Kim, J. Cha, D. Kang, D. Kim, and B. Kim, “A $\Delta\Sigma$-digitized polar RF transmitter,” *IEEE Transactions on Microwave Theory and Techniques*, vol. 55, no. 12, pp. 2679–2690, Dec. 2007.

[27] J.-H. Chen, H.-S. Yang, and Y.-J. E. Chen, “A technique for implementing wide dynamic-range polar transmitters,” *IEEE Transactions on Microwave Theory and Techniques*, vol. 58, no. 9, pp. 2368–2374, Sep. 2010.

[28] H.-S. Yang, J.-H. Chen, and Y.-J. E. Chen, “A polar transmitter using interleaving pulse modulation for multimode handsets,” *IEEE Transactions on Microwave Theory and Techniques*, vol. 59, no. 8, pp. 2083–2090, Aug. 2011.

[29] T. Sowlati, D. Rozenblit, R. Pullela, M. Damgaard, E. McCarthy, D. Koh, D. Ripley, F. Balteanu, and I. Gheorghe, “Quad-band GSM/GPRS/EDGE polar loop transmitter,” *IEEE Journal of Solid-State Circuits*, vol. 39, no. 12, pp. 2179–2189, Dec. 2004.

[30] A. Kavousian, D. K. Su, M. Hekmat, A. Shirvani, and B. A. Wooley, “A digitally modulated polar CMOS power amplifier with a 20-MHz channel bandwidth,” *IEEE Journal of Solid-State Circuits*, vol. 43, no. 10, pp. 2251–2257, Oct. 2008.

[31] C. D. Presti, F. Carrara, A. Scuderi, P. M. Asbeck, and G. Palmisano, “A 25 dBm digitally modulated CMOS power amplifier for WCDMA/EDGE/OFDM with adaptive digital predistortion and efficient power control,” *IEEE Journal of Solid-State Circuits*, vol. 44, no. 7, pp. 1883–1896, Jul. 2009.

[32] K. Oishi, E. Yoshida, Y. Sakai, H. Takauchi, Y. Kawano, N. Shirai, H. Kano, M. Kudo, T. Murakami, T. Tamura, S. Kawai, S. Yamaura, K. Suto, H. Yamazaki, and T. Mori, “A 1.95GHz fully integrated envelope elimination and restoration CMOS power amplifier with envelope/phase generator and timing aligner for WCDMA and LTE,” in *IEEE International Solid-State Circuits Conference, 2014*, 2014, pp. 60–62.

[33] D. F. Kimball, J. Jeong, C. Hsia, P. Draxler, S. Lanfranco, W. Nagy, K. Linthicum, L. E. Larson, and P. M. Asbeck, “High-efficiency envelope-tracking W-CDMA base-station amplifier using GaN HFETs,” *IEEE Transactions on Microwave Theory and Techniques*, vol. 54, no. 11, pp. 3848–3856, November 2006.

[34] A. Zhu, P. J. Draxler, C. Hsia, T. J. Brazil, D. F. Kimball, and P. M. Asbeck, “Digital predistortion for envelope-tracking power amplifiers using decomposed piecewise Volterra series,” *IEEE Transactions on Microwave Theory and Techniques*, vol. 56, no. 10, pp. 2237–2347, Oct. 2008.

[35] J. Jeong, D. F. Kimball, M. Kwak, C. Hsia, P. Draxler, and P. M. Asbeck, “Wideband envelope tracking power amplifiers with reduced bandwidth power supply waveforms and adaptive digital predistortion techniques,” *IEEE Transactions on Microwave Theory and Techniques*, vol. 57, no. 12, pp. 3307–3314, Dec. 2009.

[36] J. Jeong, D. F. Kimball, M. Kwak, P. Draxler, C. Hsia, C. Steinbeiser, T. Landon, O. Krutko, L. E. Larson, and P. M. Asbeck, “High-efficiency WCDMA envelope tracking

base-station amplifier implemented with GaAs HVHBTs," *IEEE Journal of Solid-State Circuits*, vol. 44, no. 10, pp. 2629–2639, Oct. 2009.

[37] J. H. Kim, G. D. Jo, J. H. Oh, Y. H. Kim, K. C. Lee, J. H. Jung, and C. S. Park, "High-efficiency envelope-tracking transmitter with optimized class-F^{-1} amplifier and 2-bit envelope amplifier for 3G LTE base station," *IEEE Transactions on Microwave Theory and Techniques*, vol. 59, no. 6, pp. 1610–1621, June 2011.

[38] F. Wang, D. F. Kimball, J. D. Popp, A. H. Yang, D. Y. Lie, P. M. Asbeck, and L. E. Larson, "An improved power-added efficiency 19-dBm hybrid envelope elimination and restoration power amplifier for 802.11g WLAN applications," *IEEE Transactions on Microwave Theory and Techniques*, vol. 54, no. 12, pp. 4086–4099, Dec. 2006.

[39] F. Wang, D. F. Kimball, D. Y. Lie, P. M. Asbeck, and L. E. Larson, "A monolithic high-efficiency 2.4-GHz 20-dBm SiGe BiCMOS envelope-tracking OFDM power amplifier," *IEEE Journal of Solid-State Circuits*, vol. 42, no. 6, pp. 1271–1281, Jun. 2007.

[40] I. Kim, Y. Y. Woo, J. Kim, J. Moon, J. Kim, and B. Kim, "High-efficiency hybrid EER transmitter using optimized power amplifier," *IEEE Transactions on Microwave Theory and Techniques*, vol. 56, no. 11, pp. 2582–2993, Nov. 2008.

[41] A. Shameli, A. Safarian, A. Rofougaran, M. Rofougaran, and F. D. Flaviis, "A two-point modulation technique for CMOS power amplifier in polar transmitter architecture," *IEEE Transactions on Microwave Theory and Techniques*, vol. 56, no. 1, pp. 31–38, Jan. 2008.

[42] P. A. Warr, K. A. Morris, G. T. Watkins, T. R. Horseman, K. Takasuka, Y. Ueda, Y. Kobayashi, and S. Miya, "A 60% PAE WCDMA handset transmitter amplifier," *IEEE Transactions on Microwave Theory and Techniques*, vol. 57, no. 10, pp. 2368–2377, Oct. 2009.

[43] R. Shrestha, R. van der Zee, A. de Graauw, and B. Nauta, "A wideband supply modulator for 20 MHz RF bandwidth polar PAs in 65 nm CMOS," *IEEE Journal of Solid-State Circuits*, vol. 44, no. 4, pp. 1272–1280, Apr. 2009.

[44] J. Lopez, Y. Li, J. D. Popp, D. Y. C. Lie, C.-C. Chuang, K. Chen, S. Wu, T.-Y. Yang, and G.-K. Ma, "Design of highly efficient wideband RF polar transmitters using the envelope-tracking technique," *IEEE Journal of Solid-State Circuits*, vol. 44, no. 9, pp. 2276–2294, Sep. 2009.

[45] J. Choi, D. Kim, D. Kang, and B. Kim, "A polar transmitter with CMOS programmable hysteretic-controlled hybrid switching supply modulator for multistandard applications,"

IEEE Transactions on Microwave Theory and Techniques, vol. 57, no. 7, pp. 1675–1686, Jul. 2009.

[46] D. Kang, D. Kim, J. Choi, J. Kim, Y. Cho, and B. Kim, "A multimode/multiband power amplifier with a boosted supply modulator," *IEEE Transactions on Microwave Theory and Techniques*, vol. 58, no. 10, pp. 2598–2608, Oct. 2010.

[47] Y. Li, J. Lopez, D. Y. C. Lie, K. Chen, S. Wu, T.-Y. Yang, and G.-K. Ma, "Circuits and system design of RF polar transmitters using envelope-tracking and SiGe power ampliers for mobile WiMAX," *IEEE Transactions on Circuits and Systems I: Fundamental Theory and Applications*, vol. 58, no. 5, pp. 893–901, May 2011.

[48] M. Hassan, M. Kwak, V. W. Leung, C. Hsia, J. J. Yan, D. F. Kimball, L. E. Larson, and P. M. Asbeck, "High efficiency envelope tracking power amplifier with very low quiescent power for 20 MHz LTE," in *IEEE Radio Frequency Integrated Circuits Symposium (RFIC), 2011*, 2011.

[49] D. Kim, D. Kang, J. Choi, J. Kim, Y. Cho, and B. Kim, "Optimization for envelope shaped operation of envelope tracking power amplifier," *IEEE Transactions on Microwave Theory and Techniques*, vol. 59, no. 7, pp. 1787–1795, Jul. 2011.

[50] J. Choi, D. Kang, D. Kim, and B. Kim, "Optimized envelope tracking operation of Doherty power amplifier for high efficiency over an extended dynamic range," *IEEE Transactions on Microwave Theory and Techniques*, vol. 57, no. 6, pp. 1508–1515, Jun. 2009.

[51] J. Moon, J. Son, J. Kim, I. Kim, S. Jeel, Y. Y. Woo, and B. Kim, "Doherty amplifier with envelope tracking for high efficiency," in *IEEE MTT-S International Microwave Symposium Digest*, Anaheim, CA, May 2010, pp. 1086–1089.

[52] C.-T. Chen, C.-J. Li, T.-S. Horng, J.-K. Jau, and J.-Y. Li, "Design and linearization of class-E power amplifier for nonconstant envelope modulation," *IEEE Transactions on Microwave Theory and Techniques*, vol. 57, no. 4, pp. 957–964, Apr. 2009.

[53] J. Li and W. Chen, "A new envelope tracking technique for concurrent dual-band PAs," in *2012 2nd International Conference on Consumer Electronics, Communications and Networks (CECNet)*, Yichang, 2012.

[54] A. Cidronali, F. Zucchelli, S. Maddio, N. Giovannelli, and G. Manes, "Bi-dimensional shaping function in concurrent dual band GaAs envelope tracking power amplifier," in *IEEE Topical Conference on Power Amplifiers for Wireless and Radio Applications (PAWR)*, Santa Clara, CA, Jan. 2012, pp. 29–32.

[55] P. L. Gilabert, G. Montoro, D. Lopez, and J. A. Garca, "3D digital predistortion for dual-band envelope tracking power amplifiers," in *IEEE Asia-Pacific Microwave Conference Proceedings 2013*, 2013, pp. 734–736.

[56] M. Hassan, L. E. Larson, V. W. Leung, D. F. Kimball, and P. M. Asbeck, "A wideband CMOS/GaAs HBT envelope tracking power amplifer for 4G LTE mobile terminal applications," *IEEE Transactions on Microwave Theory and Techniques*, vol. 60, no. 5, pp. 1321–1330, May 2012.

[57] D. Kang, B. Park, D. Kim, J. Kim, Y. Cho, and B. Kim, "Envelope-tracking CMOS power ampli?er module for LTE applications," *IEEE Transactions on Microwave Theory and Techniques*, vol. 61, no. 10, pp. 3763–3773, Oct. 2013.

[58] Y. Cho, D. Kang, J. Kim, D. Kim, B. Park, and B. Kim, "A dual power-mode multi-band power ampli?er with envelope tracking for handset applications," *IEEE Transactions on Microwave Theory and Techniques*, vol. 61, no. 4, pp. 1608–1619, Apr. 2013.

[59] J. Kim, D. Kim, Y. Cho, D. Kang, B. Park, and B. Kim, "Envelope-tracking two-stage power amplifer with dual-mode supply modulator for LTE applications," *IEEE Transactions on Microwave Theory and Techniques*, vol. 61, no. 1, pp. 543–552, Jan. 2013.

[60] M. Hassan, P. M. Asbeck, and L. E. Larson, "A CMOS dual-switching power-supply modulator with 8% efficiency improvement for 20MHz LTE envelope tracking RF power amplifiers," in *IEEE International Solid-State Circuits Conference, 2013*, 2013, pp. 366–368.

[61] R. Wu, Y.-T. Liu, J. Lopez, C. Schecht, Y. Li, and D. Y. C. Lie, "High-ef?ciency silicon-based envelope-tracking power ampli?er design with envelope shaping for broadband wireless applications," *IEEE Journal of Solid-State Circuits*, vol. 48, no. 9, pp. 2030–2040, Sep. 2013.

[62] M. Kwak, D. F. Kimball, C. D. Presti, A. Scuderi, C. Santagati, J. J. Yan, P. M. Asbeck, and L. E. Larson, "Design of a wideband high-voltage high-efficiency BiCMOS envelope amplifier for micro-base-station RF power ampli?ers," *IEEE Transactions on Microwave Theory and Techniques*, vol. 60, no. 6, pp. 1850–1861, Jun. 2012.

[63] J. H. Kim, H. S. Son, W. Y. Kim, and C. S. Park, "Envelope amplifer with multiple-linear regulator for envelope tracking power amplifer," *IEEE Transactions on Microwave Theory and Techniques*, vol. 61, no. 11, pp. 3951–3960, Nov. 2013.

[64] J. Kim, J. Son, S. Jee, S. Kim, and B. Kim, “Optimization of envelope tracking power ampli?er for base-station applications,” *IEEE Transactions on Microwave Theory and Techniques*, vol. 61, no. 4, pp. 1620–1627, Apr. 2013.

[65] P. Eloranta, P. Seppinen, S. Kallioinen, T. Saarela, and A. Prssinen, “A multimode transmitter in 0.13 μm CMOS using direct-digital RF modulator,” *IEEE Journal of Solid-State Circuits*, vol. 42, no. 12, pp. 2774–2784, Dec. 2007.

[66] A. Jerng and C. G. Sodini, “A wideband $\Delta\Sigma$ digital-RF modulator for high data rate transmitters,” *IEEE Journal of Solid-State Circuits*, vol. 42, no. 8, pp. 1710–1722, Aug. 2007.

[67] H. Chireix, “High power outphasing modulation,” *Proceedings of the Institute of Radio Engineers*, vol. 23, no. 11, pp. 1370–1392, Nov. 1935.

[68] D. C. Cox, “Linear amplification with nonlinear components,” *IEEE Transactions on Communications*, vol. 22, no. 12, pp. 1942–1945, Dec. 1974.

[69] M. E. Heidari, M. Lee, and A. A. Abidi, “All-digital outphasing modulator for a software-defined transmitter,” *IEEE Journal of Solid-State Circuits*, vol. 44, no. 4, pp. 1260–1271, Apr. 2009.

[70] Y. Zhou and J. Yuan, “A 10-Bit wide-band CMOS direct digital RF amplitude modulator,” *IEEE Journal of Solid-State Circuits*, vol. 38, no. 7, pp. 1182–1188, Jul. 2003.

[71] S. Luschas, R. Schreier, and H.-S. Lee, “Radio frequency digital-to-analog converter,” *IEEE Journal of Solid-State Circuits*, vol. 39, no. 9, pp. 1462–1467, Sep. 2004.

[72] C. Jones, B. Tenbroek, P. Fowers, C. Beghein, J. Strange, F. Beffa, and D. Nalbantis, “Direct-conversion WCDMA transmitter with 163dBc/Hz noise at 190MHz offset,” in *IEEE International Solid-State Circuits Conference*, Feb. 2007, pp. 336–607.

[73] M. Nielsen and T. Larsen, “A transmitter architecture based on Delta Sigma modulation and switch-mode power amplification,” *IEEE Transactions on Circuits and Systems - II: Express Briefs*, vol. 54, no. 8, pp. 735–739, Aug. 2007.

[74] S. M. Taleie, T. Copani, B. Bakkaloglu, and S. Kiaei, “A linear $\Sigma - \Delta$ digital IF to RF DAC transmitter with embedded mixer,” *IEEE Transactions on Microwave Theory and Techniques*, vol. 56, no. 5, pp. 1059–1068, May 2008.

[75] A. Pozsgay, T. Zounes, R. Hossain, M. Boulemnakher, V. Knopik, and S. Grange, “A fully digital 65nm CMOS transmitter for the 2.4-to-2.7GHz WiFi/WiMAX bands using

5.4GHz ΔΣ RF DACs," in *IEEE International Solid-State Circuits Conference*, Feb. 2008, pp. 360–619.

[76] A. Mirzaei and H. Darab, "A low-power WCDMA transmitter with an integrated notch filter," *IEEE Journal of Solid-State Circuits*, vol. 43, no. 12, pp. 2868–2881, Dec. 2008.

[77] X. He and J. van Sinderen, "A low-power, low-EVM, SAW-less WCDMA transmitter using direct quadrature voltage modulation," *IEEE Journal of Solid-State Circuits*, vol. 44, no. 12, pp. 3448–3458, Dec. 2009.

[78] S. Lee, J. Lee, H. Park, K.-Y. Lee, and S. Nam, "Self-calibrated two-point DeltaSigma modulation technique for RF transmitters," *IEEE Transactions on Microwave Theory and Techniques*, vol. 58, no. 7, pp. 1748–1756, Jul. 2010.

[79] M. Park, M. H. Perrott, and R. B. Staszewski, "A time-domain resolution improvement of an RF - DAC," *IEEE Transactions on Circuits and Systems - II: Express Briefs*, vol. 57, no. 7, pp. 517–521, Jul. 2010.

[80] S. Kousai and A. Hajimiri, "An octave-range, watt-level, fully-integrated CMOS switching power mixer array for linearization and back-off-efficiency improvement," *IEEE Journal of Solid-State Circuits*, vol. 44, no. 12, pp. 3376–3392, Dec. 2009.

[81] T. Johnson and S. P. Stapleton, "RF class-D amplification with bandpass Sigma-Delta modulator drive signals," *IEEE Transactions on Circuits and Systems - I: Regular Papers*, vol. 53, no. 12, pp. 2507–2520, Dec. 2006.

[82] T. Johnson, R. Sobot, and S. Stapleton, "Manchester encoded bandpass sigmadelta modulation for RF class D amplifiers," *IET Circuits Devices Systems*, vol. 1, no. 1, pp. 21–26, Feb. 2007.

[83] T. Johnson and S. P. Stapleton, "Comparison of bandpass ΔΣ modulator coding efficiency with a periodic signal model," *IEEE Transactions on Circuits and Systems - I: Regular Papers*, vol. 55, no. 11, pp. 3763–3775, Dec. 2008.

[84] P. Wagh, P. Midya, P. Rakers, J. Caldwell, and T. Schooler, "An all-digital universal RF transmitter," in *Proceedings of IEEE Custom Integrated Circuits Conference*, Oct. 2004, pp. 549–552.

[85] T.-P. Hung, J. Rode, L. E. Larson, and P. M. Asbeck, "Design of H-bridge class-D power amplifiers for digital pulse modulation transmitters," *IEEE Transactions on Microwave Theory and Techniques*, vol. 55, no. 12, pp. 2845–2855, Dec. 2007, h-Bridge Voltage Mode Class D in CMOS with BPDSM input signal.

[86] J. T. Stauth and S. R. Sanders, “A 2.4GHz, 20dBm class-D PA with single-bit digital polar modulation in 90nm CMOS,” in *Proceedings of IEEE Custom Integrated Circuits Conference*, Sep. 2008, pp. 737–740.

[87] J. S. Walling, H. Lakdawala, Y. Palaskas, A. Ravi, O. Degani, K. Soumyanath, and D. J. Allstot, “A class-E PA with pulse-width and pulse-position modulation in 65nm CMOS,” *IEEE Journal of Solid-State Circuits*, vol. 44, no. 6, pp. 1668–1678, Jun. 2009.

[88] W.-Y. Kim, J. Rode, A. Scuderi, H.-S. Son, C. S. Park, and Peter.M.Asbeck, “An efficient voltage-mode class-D power amplifier for digital transmitters with Delta-Sigma modulation,” in *IEEE MTT-S International Microwave Symposium Digest*, 2011.

[89] S. Moloudi, K. Takinami, M. Youssef, M. Mikhemar, and A. Abidi, “An outphasing power amplifier for a software-defined radio transmitter,” in *IEEE International Solid-State Circuits Conference*, Feb. 2008, pp. 568–636.

[90] P. A. Godoy, S. Chung, T. W. Barton, D. J. Perreault, and J. L. Dawson, “A highly efficient 1.95-GHz, 18-W asymmetric multilevel outphasing transmitter for wideband applications,” in *IEEE MTT-S International Microwave Symposium Digest*, Jun. 2011.

[91] S. Chung, P. A. Godoy, T. W. Barton, D. J. Perreault, and J. L. Dawson, “Asymmetric multilevel outphasing transmitter using class-E PAs with discrete pulse width modulation,” in *IEEE MTT-S International Microwave Symposium Digest*, May 2010, pp. 264–267.

[92] X. He, M. Collados, N. Pavlovic, and J. van Sinderen, “A 1.2V, 17dBm digital polar CMOS PA with transformer-based power interpolating,” in *European Solid-State Circuits Conference*, Sep. 2008, pp. 486–489.

[93] A. Frapp, A. Flament, B. Stefanelli, A. Kaiser, and A. Cathelin, “An all-digital RF signal generator using high-speed $\Delta\Sigma$ modulators,” *IEEE Journal of Solid-State Circuits*, vol. 44, no. 10, pp. 2722–2732, Oct. 2009.

[94] D. Chowdhury, LuYe, E. Alon, and A. M. Niknejad, “An efficient mixed-signal 2.4-GHz polar power amplifier in 65-nm CMOS technology,” *IEEE Journal of Solid-State Circuits*, vol. 46, no. 8, pp. 1796–1809, Aug. 2011.

[95] P. A. Godoy, S. Chung, T. W. Barton, D. J. Perreault, and J. L. Dawson, “A 2.4-GHz, 27-dBm asymmetric multilevel outphasing power ampli?er in 65-nm CMOS,” *IEEE Journal of Solid-State Circuits*, vol. 47, no. 10, pp. 2372–2384, Oct. 2012.

[96] H. Sarbishaei, D. Wu, and S. Boumaiza, "Linearity of GaN HEMT RF power amplifiers - a circuit perspective," in *IEEE MTT-S International Microwave Symposium Digest*, Montreal, QC, May 2012.

[97] A. S. Sedra, *Microelectronic Circuits*, sixth edition ed. Oxford University Press, 2009.

[98] J. C. Pedro and N. B. Carvalho, *Intermodulation Distortion in Microwave and Wireless Circuits*. Artech House, 2003.

[99] I. Angelov, H. Zirath, and N. Rorsman, "A new empirical nonlinear model for hemt and mesfet devices," *IEEE Transactions on Microwave Theory and Techniques*, vol. 40, no. 12, pp. 2258–2266, Dec. 1992.

[100] P. Wright, J. Lees, J. Benedikt, P. J. Tasker, and S. C. Cripps, "A methodology for realizing high efficiency class-J in a linear and broadband PA," *IEEE Transactions on Microwave Theory and Techniques*, vol. 57, no. 12, pp. 3196–3204, Dec. 2009.

[101] D. Y.-T. Wu, F. Mkadem, and S. Boumaiza, "Design of a broadband and highly efficient 45W GaN power amplifier via simplified real frequency technique," in *IEEE MTT-S International Microwave Symposium Digest*, Anaheim, CA, May 2010, pp. 1090–1093.

[102] P. Aaen, J. Pla, and J. Wood, *Modeling and Characterization of RF and Microwave Power FETs*. Cambridge University Press, 2007.

[103] A. Zhu, J. C. Pedro, and T. J. Brazil, "Dynamic deviation reduction-based Volterra behavioral modeling of RF power amplifiers," *IEEE Trans. on Microw. Theory and Tech.*, vol. 54, no. 12, pp. 4323–4332, Dec. 2006.

[104] S. A.Bassam, W. Chen, M. Helaoui, F. M. Ghannouchi, and Z. Feng, "Linearization of concurrent dual-band power amplifier based on 2D-DPD technique," *IEEE Trans. on Microw. Theory and Tech.*, vol. 21, no. 12, pp. 685–687, Dec. 2011.

[105] Y. Liu, W. Che, J. Zhou, B. Zhou, and F. M. Ghannouchi, "Digital predistortion for concurrent dual-band transmitters using 2-D modified memory polynomials," *IEEE Transactions on Microwave Theory and Techniques*, vol. 61, no. 1, pp. 281–290, Jan. 2013.

[106] B. Fehri and S. Boumaiza, "Baseband equivalent Volterra series for digital predistortion of dual-band power amplifiers," *IEEE Transactions on Microwave Theory and Techniques*, vol. 62, no. 3, pp. 700–714, Mar. 2014.

[107] F. Mkadem and S. Boumaiza, “Multi-band complexity-reduced generalized-memory-polynomial power amplifier digital predistortion,” *IEEE Trans. on Microw. Theory and Tech.*, submitted 2014.

[108] ——, “Physically inspired neural network model for RF power amplifier behavioral modeling and digital predistortion,” *IEEE Trans. on Microw. Theory and Tech.*, vol. 59, no. 4, pp. 913–923, Apr. 2011.

[109] Y. Hu and S. Boumaiza, “Optimization of the switching stage supply voltage in parallel voltage controlled envelope amplifier,” in *IEEE Topical Symposium on Power Amplifiers for Wireless Communications*, San Diego, CA, Sep. 2012.

[110] J. K. K. Son, S. Jee, S. Kim, and B. Kim, “Optimization of envelope tracking power amplifier for base-station applications,” *IEEE Transactions on Microwave Theory and Techniques*, vol. 61, no. 4, pp. 1620–1626, Apr. 2013.

[111] J. F. Miranda, M. Olavsbraten, K. M. Gjertsen, and W. Caharija, “First and second order polynomial functions for bandwidth reduction of dynamic biasing signals,” in *IEEE International Conference onWireless Information Technology and Systems (ICWITS)*, 2010.

[112] M. Younes, A. Kwan, M. Rawat, and F. M. Ghannouchi, “Three-dimensional digital predistorter for concurrent tri-band power amplifier linearization,” in *IEEE MTT-S International Microwave Symposium Digest*, Seatle, WA, Jun. 2013.

[113] ——, “Linearization of concurrent tri-band transmitters using 3-D phase-aligned pruned volterra model,” *IEEE Trans. on Microw. Theory and Tech.*, vol. 61, no. 12, pp. 4569–4578, Dec. 2013.